

# **Actin-based motility**

Dissertation der Fakultät für Physik  
der Ludwig-Maximilians-Universität  
München

vorgelegt von  
Frau Azam Gholami  
aus Iran

München, den 30. Mai 2007

Erstgutachter: Prof. Dr. Erwin Frey

Zweitgutachter: Dr. habil. Martin Falcke

Tag der mündlichen prüfung: 2. July 2007

---

# Actin-Based Motility

Azam Gholami

---



# Zusammenfassung

Räumlich kontrollierte Polymerisation von Aktin ist der Ursprung selbstständiger zellularen Bewegung und ist die Ursache für die Bildung von zellularen Vorsprüngen, wie Lamellipodia. Die Krankheitserreger *Listeria monocytogenes* und *Shigella flexneri* bewegen sich in befallenen Zellen, indem sie auf einem Aktinschweif reiten, der aus hochgradig querverbundenen polymerisierten Aktinfilamenten besteht, die einen Kreislauf von Anhaftung und Ablösung an der Oberfläche der Bakterien durchlaufen.

Der Schwerpunkt dieser Arbeit liegt auf der Formulierung eines einfachen theoretischen Modells der auf Aktin basierenden Zellbewegung. Der physikalische Mechanismus unseres Modells verwendet sowohl belastungsabhängige Ablösungs- und Anhaftungsraten sowie Polymerisationsgeschwindigkeiten, als auch Rückstellkräfte der gebundenen Filamente und treibende Kräfte der abgelösten Filamente oder der möglichen Querverbindungen und Verknüpfungen des Aktinnetzwerkes. Wir konnten zeigen, dass das Zusammenspiel von Bindung und Ablösung von Filamenten auf der einen Seite und Polymerisation und Querverbindung von Aktin auf der anderen Seite zu spontanen Oszillationen der Hindernisgeschwindigkeit führt. Unsere Ergebnisse sind in Bezug auf die Geschwindigkeitsamplituden und Perioden in guter Übereinstimmung mit denen in *Listeria* Experimenten. In diesem Modell sind weder Elastizität noch eine mögliche Krümmung des Hindernisses berücksichtigt. Dies wird Gegenstand zukünftiger Modellierung Aktin induzierter Bewegung sein.

Als eine wichtige Vorarbeit für unser Modell haben wir analytische Berechnungen und ausführliche Monte Carlo Simulationen durchgeführt, um die treibende Kraft der abgelösten Filamente zu untersuchen. Die Analyse beginnt mit der Berechnung der entropischen Kraft, die durch ein fixiertes Polymer auf eine massive Wand ausgeübt wird. Diese rein entropische Kraft hängt von der Kontourlänge, der Persistenzlänge und der Orientierung des Polymers, als auch gegebenenfalls vom Abstand des Auflagepunkts des Polymers zur Wand ab. Der Gültigkeitsbereich unserer analytischen Lösung wurde mit zahlreichen Monte Carlo Simulationen für steife, semiflexible und flexible Polymere untersucht. Das Hindernis wurde in dieser Analyse

stets als starre Wand behandelt. Im realen Experiment sind aber die Hindernisse, wie z.B. Membranen, keine starren Objekte, sondern unterliegen thermischen Fluktuationen. Deswegen sind weitere analytische Berechnungen und Monte Carlo Simulation nötig, um die Beweglichkeit der Hindernisse mit zu berücksichtigen.

Um die auf Aktin basierende Zellbewegung zu untersuchen, werden in *in vivo* Experimenten üblicherweise ActA beschichtete Perlen verwendet. Um den Einfluss der Krümmung des Hindernisses auf die entropische Kraft zu untersuchen, haben wir die treibende Gesamtkraft eines homogenen Aktinnetzwerkes auf eine starre Kugel berechnet. Diese Analyse hat eindeutig ergeben, dass sowohl die Eigenschaften des Hindernisses (wie z.B. der Kugelradius) als auch die des Netzwerkes (wie z.B. dessen Orientierung) einen direkten Einfluss auf die Stärke und Richtung der Gesamtkraft haben. Die Berechnungen wurde dabei für ein statisches System durchgeführt: Eine konstante Anzahl von Filamenten mit identischer Kontourlänge drücken gegen eine Kugel in festem Abstand. Bindung und Ablösung der Filamente an und von der Kugel, Polymerisation und der Aufbau von Querverbindungen sind dynamische Prozesse, die in zukünftigen Modellierungen mit einbezogen werden sollen.

Im Zellcytoskelett, das ein aus Biopolymeren bestehendes Fasernetzwerk darstellt, werden thermische Fluktuationen durch die Anwesenheit anderer Filamente stark unterdrückt. Diese Beschränkung erhöht die freie Energie der einzelnen fluktuierenden Polymere, was zu einer gemittelten abstossenden Kraft entropischen Ursprungs führt. Das vierte Kapitel dieser Arbeit widmet sich entropischer Kräfte zwischen zwei parallelen und senkrechten Polymeren. Die analytischen Ergebnisse, die wiederum mit Monte Carlo Simulationen untermauert wurden, zeigen eindeutig die Existenz einer räumlichen "Helfrich Abstossung" zweier parallelen Polymeren bei kleinen Abständen.

# Contents

<b>Zusammenfassung</b>	<b>v</b>
<b>1 Introduction</b>	<b>1</b>
1.1 Actin-based motility . . . . .	1
1.2 The wormlike chain model . . . . .	14
1.3 Non-linear force-extension relation . . . . .	16
1.4 Objective of this thesis . . . . .	20
<b>2 Entropic forces exerted by a grafted polymer on a wall</b>	<b>23</b>
2.1 Introduction . . . . .	23
2.2 Entropic forces and probability densities . . . . .	27
2.3 Polymer orthogonal to a wall . . . . .	31
2.4 Grafted polymer at an oblique angle to the wall . . . . .	44
2.5 Protrusion velocity and intercalation probability . . . . .	62
2.6 Summary . . . . .	67
<b>3 Entropic forces exerted by an actin network on a sphere</b>	<b>71</b>
3.1 Introduction . . . . .	71
3.2 An inhomogeneous actin network and a rigid obstacle . . . . .	72
3.3 A homogeneous actin network and a sphere . . . . .	74
3.4 A homogeneous actin network and a cylinder . . . . .	78
3.5 Summary . . . . .	80
<b>4 Steric repulsions between two polymers</b>	<b>83</b>
4.1 Introduction . . . . .	83
4.2 Steric repulsion between two parallel polymers . . . . .	85
4.3 Steric repulsion between two perpendicular polymers . . . . .	96
4.4 Summary . . . . .	105

<b>5</b>	<b>Velocity oscillations in actin-based motility</b>	<b>107</b>
5.1	Introduction . . . . .	107
5.2	Definition of the model . . . . .	108
5.3	Monodisperse distribution and set of ODEs . . . . .	111
5.4	Summary . . . . .	116
<b>6</b>	<b>Summary</b>	<b>117</b>
	<b>Appendix</b>	<b>119</b>
<b>A</b>	<b>Monte Carlo method</b>	<b>121</b>
<b>B</b>	<b>Euler buckling instability</b>	<b>123</b>
<b>C</b>	<b>Laplace and Jacobi transformations</b>	<b>125</b>
C.1	Inverse Laplace transform . . . . .	125
C.2	Saddle point approximation . . . . .	129
C.3	Jacobi transformation of the restricted partition sum . . . . .	130
C.4	Graft-angle-dependent force . . . . .	131
<b>D</b>	<b>Force-extension relation of attached filaments</b>	<b>135</b>
	<b>Bibliography</b>	<b>141</b>
	<b>Acknowledgements</b>	<b>147</b>
	<b>Lebenslauf</b>	<b>149</b>

# List of Figures

1.1	Cytoskeleton of a cultured epithelial cell. . . . .	1
1.2	Actin based motility of cell and <i>Listeria</i> . . . . .	3
1.3	The actin polymerization machinery . . . . .	4
1.4	Localization of Arp2/3 complex in lamellipodia . . . . .	7
1.5	Speed and position of <i>Listeria</i> as a function of time . . . . .	8
1.6	ActA coated bead propulsion . . . . .	9
1.7	Actin treadmilling . . . . .	10
1.8	Tethered ratchet model of propulsion . . . . .	12
1.9	Curvature-induced elastic stress development . . . . .	14
1.10	Worm-like chain model . . . . .	15
1.11	Setup: force-extension . . . . .	17
1.12	Nonlinear force-extension . . . . .	19
1.13	Pulling force acts on the free end of a filament . . . . .	20
2.1	Setup: a polymer pushing against a rigid wall . . . . .	24
2.2	Probability density in 3d . . . . .	35
2.3	Confinement free energy in 3d . . . . .	38
2.4	Entropic force exerted on the wall in 3d . . . . .	39
2.5	Probability density in 2d . . . . .	41
2.6	Confinement free energy in 2d . . . . .	43
2.7	Entropic force exerted on the wall in 2d . . . . .	44
2.8	Setup map in $x - z$ plane . . . . .	45
2.9	Density plot of $P(x, z)$ in 3d and 2d (Analytical) . . . . .	49
2.10	Density plot of $P(x, z)$ in 3d and 2d (MC) . . . . .	49
2.11	Probability isosurface in 3d . . . . .	50
2.12	Density plots of $P(x, z)$ in 3d (MC) . . . . .	51
2.13	Density plots of $P(x, z)$ in 2d (MC) . . . . .	52
2.14	Color density plots of $P(x, y)$ (MC) . . . . .	53
2.15	Comparison of MC data to analytical results for $P(x = 0, y)$ . . . . .	54
2.16	Geometry of the problem in the reduced coordinates . . . . .	55
2.17	Scaling function of the entropic force in 2d and 3d (I) . . . . .	57

2.18	Scaling function of the entropic force in $2d$ and $3d$ (II)	58
2.19	Entropic force as a function of $\zeta$	61
2.20	Entropic force as a function of $\vartheta$	62
2.21	Polymer's contour effect on entropic force	63
2.22	Entropic force as a function of $\vartheta$ in $2d$	64
2.23	Comparison to factorization approximation	65
2.24	Setup: polymerization against an external load	65
2.25	Protrusion velocity $v$ versus inclination angle	66
2.26	Protrusion velocity as a function of external load	67
3.1	Actin network and a hard sphere	72
3.2	An inhomogeneous actin network and a obstacle	73
3.3	Geometry of sphere and actin network	74
3.4	Actin network and a sphere	75
3.5	Force for a flat and spherical graft surface	76
3.6	Force per single filament as a function of angle	77
3.7	A stiff polymer network in the presence of a cylinder	78
3.8	A smooth hard wall with finite length and a filament	79
3.9	Tangential force exerted by a polymer on a wall	80
4.1	A membrane fluctuating near a rigid wall	84
4.2	A rigid polymer orients perpendicular to a membrane	84
4.3	Microfilaments in cell cytoskeleton	85
4.4	A stack of fluctuating polymers	86
4.5	Effective repulsion between polymers and membranes.	89
4.6	A polymer fluctuating near a rigid line	90
4.7	A polymer close to a wall in presence of external pressure	92
4.8	Average distance as a function of pressure (MC)	93
4.9	The results of Monte Carlo simulations on membranes	94
4.10	Effective steric potential of a filament (MC)	95
4.11	Coefficients of effective potential between polymer and wall	97
4.12	A polymer fluctuating near a rigid polymer	98
4.13	A polymer fluctuating above a point barrier	98
4.14	Effective repulsive force between two perpendicular polymers	100
4.15	Effective steric potential of two perpendicular polymers (MC)	102
4.16	A polymer fluctuating above a point barrier	102
5.1	Set up in actin-based motility	109
5.2	Monodisperse length distribution of filaments	112
5.3	Phase diagram	113
5.4	Example of spontaneous oscillations	114

5.5	Speed-displacement curves of the obstacle . . . . .	115
B.1	Setup: Euler buckling instability . . . . .	123
B.2	$f$ as a function of $y$ for a beam . . . . .	124
B.3	Entropic forces together with mechanical limits . . . . .	124
D.1	Force-extension curves (exact+approximation) . . . . .	136
D.2	Setup: A filament is attached to the wall via a linker . . . . .	136
D.3	Force-extension curves in the presence of a linker . . . . .	138
D.4	Example of typical oscillations in pulling and pushing forces	139



# 1 Introduction

## 1.1 Actin-based motility

### The cytoskeleton of cells

The mechanical stability and integrity of biological cells is provided by the cytoskeleton, a semi-dilute meshwork of biopolymers. Recent research has underscored its role as a dynamic, multifunctional muscle, whose passive and active mechanical performance is highly heterogeneous in space and time and intimately linked to many biological functions, such that it may serve as a sensitive indicator for the health or developmental state of the cell. The cytoskeleton is a network of protein fibers in the cytoplasm

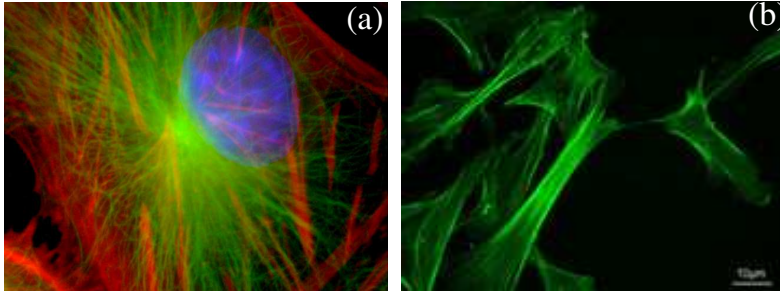


**Figure 1.1** (a) Cytoskeleton of a cultured epithelial cell. Microtubules are shown in green, actin in red and DNA in blue. (b) Actin cytoskeleton of mouse embryo fibroblasts, stained with phalloidin. The figures are from the website <http://cmgm.stanford.edu/theriot/>.

that serve functions such as establishing cell shape, providing mechanical strength, generating locomotion in cells such as white blood cells and the amoeba, providing force for chromosome separation in mitosis and meiosis and involving in intracellular transport of organelles. The cytoskeleton is made up of three kinds of protein filaments: actin filaments, intermediate

filaments and microtubules (Fig. 1.1).

Actin filaments, made of monomers of the protein actin, polymerize to form long, thin fibers. These are about 8 nm in diameter and, being the thinnest of the cytoskeletal filaments, are also called microfilaments. Some functions of actin filaments are

- form a band just beneath the plasma membrane that provides mechanical strength to the cell and links transmembrane proteins (e.g., cell surface receptors) to cytoplasmic proteins. It also anchors the centrosomes at opposite poles of the cell during mitosis and pinches dividing animal cells apart during cytokinesis,
- generate cytoplasmic streaming in some cells,
- generate locomotion in cells such as amoeba,
- interact with myosin (“thick”) filaments in skeletal muscle fibers to provide the force of muscular contraction.

Intermediate filaments are fibers with an average diameter of 10 nm and thus are “intermediate” in thickness between actin filaments (8 nm) and microtubules (25 nm). Microtubules are straight, hollow cylinders whose wall is made up of a ring of approximately 13 protofilaments. They are variable in length but can grow 1000 times as long as their width and are built by the assembly of dimers of alpha and beta-tubulin. Microtubules are found in both animal and plant cells. Microtubules grow at each end by the polymerization of tubulin dimers which is powered by the hydrolysis of GTP <sup>1</sup>, and shrink at each end by the release of tubulin dimers (depolymerization). However, both processes always occur more rapidly at one end, called the plus end. The other, less active, end is the minus end. Microtubules participate in a wide variety of cell activities. Most involve motion. The motion is generated by protein “motors” that use the energy of ATP <sup>2</sup> to move along the microtubule. There are two major groups of microtubule motors: kinesins, which most of them move toward the plus end of the microtubules, and dyneins which move toward the minus end.

## Cell motility

Many biological movements like cell motility, are based on the dynamics of the actin network in cells. Cell crawling begins with protrusion, the

---

<sup>1</sup>GTP=Guanosine 5'-triphosphate.

<sup>2</sup>ATP=Adenosine triphosphate.

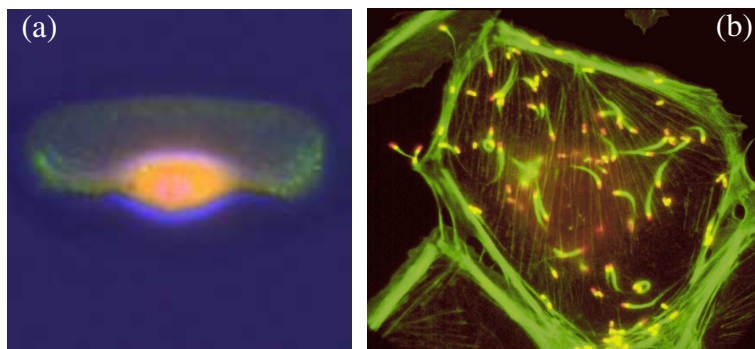


**Figure 1.2** (a) A keratocyte cell crawling on a substrate by extending a leading edge. Actin filaments are stained in green. (b) *Listeria monocytogenes* (red dots) moves inside the infected host cell by riding on an actin tail (green). The figures are from the website <http://cmgm.stanford.edu/theriot/>.

process of actin-based extension of the cell's leading edge (Fig. 1.2a). It is an important phenomenon that drives cellular and developmental processes as diverse as morphogenesis and metastasis. Cell migration is directional, ATP-consuming, and is associated with actin polymerization. It is a complex process, coupling protrusion of the cell's leading edge, contraction of the cytoskeleton, and dynamic graded adhesion. The phenomenon of lamellipodial protrusion- motile appendages of rapidly migrating simple shaped cells- is one aspect of cell movement, where our understanding is most advanced. To produce the forces required for the motion, actin is often associated with myosin, as in muscles or in the cell contractile ring (Bray, 2001). However, the presence of motor proteins like myosin is not necessary to produce a motile force; this issue has been discussed for amoeboid motion (Mitchison and Cramer, 1996) and has been demonstrated several times in the case of the bacterium *Listeria monocytogenes* (Fig. 1.2b), for which motor proteins associated with its actin tail have been sought but not found (Southwick and Purich, 1998; Loisel *et al.*, 1999). It is therefore widely accepted that the process of actin polymerization itself is sufficient to induce cell movement.

A crucial factor for protrusion is actin polarity. The two ends of an actin filament are structurally and functionally different, one termed barbed (with fast dynamics, favored for polymerization) and the opposite, termed pointed. The principal reactions constituting the cycle of turnover of the lamellipodial actin network are dendritic nucleation, elongation, capping

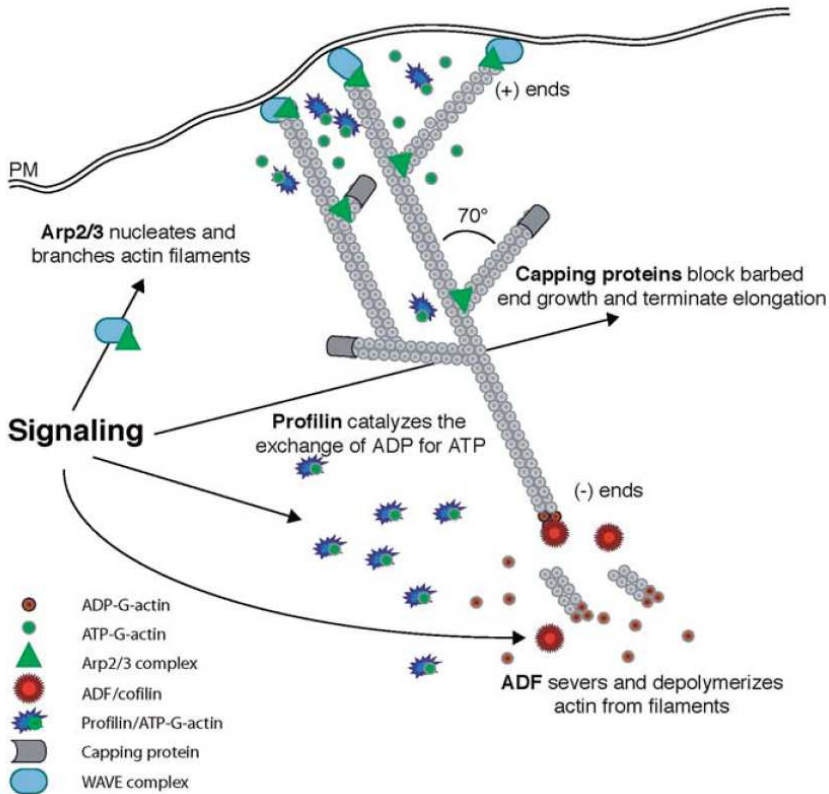


**Figure 1.3** The actin polymerization machinery triggers dendritic nucleation for protrusion at the leading edge. The activated Arp2/3 complex nucleates and branches actin filaments at the leading edge, pushing the membrane forward. Capping proteins control the half-life of filaments, and by blocking a large fraction of barbed ends, promote site-directed elongation of uncapped filaments. ADF/cofilin promotes dissociation of ADP-actin from filament pointed ends and severs preexisting filaments, generating new barbed ends. Profilin catalyzes the exchange of ADP for ATP on monomeric actin molecules, which become available for new polymerization at barbed ends. This figure is from the paper by Disanza *et al.* (2005).

and disassembly of actin filaments. First, proteins of the WASP<sup>3</sup>/WAVE<sup>4</sup> families activate Arp2/3<sup>5</sup> protein complexes (see Fig. 1.3). These complexes nucleate new actin filaments at the sides or tips of existing filaments (Welch *et al.*, 1997; Svitkina and Borisy, 1999; Borisy and Svitkina, 2000; Pollard *et al.*, 2000). The new nucleated filaments elongate at their barbed ends, exerting pushing force on the membrane at the leading edge until they are capped by capping proteins which block further addition of actin monomers. Capping is believed to increase the actin monomer pool by restricting the number of growing filament ends, and thus makes the elongation of the remaining uncapped filaments more efficient (Carlier and Pantaloni, 1997; Pantaloni *et al.*, 2001; Mogilner and Edelstein-Keshet, 2002). Actin monomers for the elongation of the uncapped barbed ends are produced in the process of disassembly at the opposite, pointed ends. This process is accelerated in cells by proteins of the ADF/cofilin family which increase the number of depolymerizing minus ends in the actin network, filling up the subunit pool for filament elongation. During steady cell locomotion, elongation/disassembly and branching/capping reactions are expected to be balanced, so that the total concentration of polymerized actin as well as the average number of actin filaments does not change.

How does the whole shape of the leading edge evolves in time and what is the control mechanism? The description of actin organization and dynamics at microscopic level is not sufficient to understand the organization and dynamics of the leading edge at a macroscopic scale. The actin dynamics is believed to be related to the geometry of the rigid surface on which the actin network is growing (Bernheim-Groswasser *et al.*, 2002). Model systems with well-defined leading edge dynamics, like fish epidermal keratocytes, are very useful to investigate the relationship between actin dynamics and cell shape. Fish keratocytes are one of the most rapidly moving eukaryotic cell types. They crawl on surfaces with a steady fan-like shape lamellipodium at a speed around 15  $\mu\text{m}$  per minute (Lee *et al.*, 1993a). The lamellipodium of the keratocyte is only a few tenths of a micrometer thick but stretches for several tens of micrometers from side to side and for about ten micrometers from front to back (see Fig.1.4). The rate of actin polymerization equals the rate of protrusion at the leading edge since, during cell movement, the actin network in the large part of the keratocyte lamellipodium is stationary with respect to the substratum (Theriot and Mitchison, 1991; Mitchison and Cramer, 1996). In the moving coordinate system of the cell, actin filaments move back from the leading edge, and

---

<sup>3</sup>WASP=Wiskott-Aldrich syndrome protein.

<sup>4</sup>WAVE=WASP family Verprolin-homologous protein.

<sup>5</sup>Arp2/3=Actin-related proteins Arp2 and Arp3.

the barbed ends of the filaments are oriented at some angle with respect to the membrane (Small, 1994). By moving from the front to the back of the lamellipodium, due to slow depolymerization of actin, the density of the actin network decreases (Svitkina *et al.*, 1997; Edelstein-Keshet and Ermentrout, 2000). The side and the back area of the lamellipodium are the only parts in which actin filaments move with respect to the substratum and to each other (Lee *et al.*, 1993a,b; Svitkina *et al.*, 1997; Anderson and Cross, 2000). Thus, the processes of actin polymerization and the subsequent contraction of the network are spatially separated, and the shape of the front part of the lamellipodium may be considered to be the result of the polymerization-driven protrusion. Three mechanisms - protrusion, adhesion, and contraction - are acting together to produce cell movement. First, growth of the actin plus ends leads to the extension of the cell's leading edge. Then, graded adhesion of the cytoskeleton to the substrate is developed: the adhesion to the surface at the front is stronger, than at the cell's back. Finally, the actin network contracts, pulling the back of the cell forward. In keratocytes, all these steps take place at the same time so that the cell moves steadily without changing its shape.

## ***Listeria* propulsion**

*Listeria monocytogenes* is a Gram-positive bacterium, named for Joseph Lister. It is a cylinder-like object with radius of around  $0.5 \mu\text{m}$  and length of  $1.5 \mu\text{m}$ . *Listeria* hijacks actin monomers from the host cell and assemble them into a comet-like tail which is made up of oriented, cross-linked networks of actin filaments. Barbed (growing) ends of actin filaments are oriented toward the bacterial surface on which actin filaments polymerize with the same rate as that of the bacterial cell propulsion. This suggests that the actin polymerization drives the bacterium forward (Theriot *et al.*, 1992). The actin comet is used as an anchor in the cytoplasm, so that as new polymerized actin is added between the bacterium surface and the older polymerized gel, the organism is propelled forward (Fig. 1.2b). *Listeria* moves through the host cytoplasm rapidly, with velocities of the order of tenth of a micron per second (Cameron *et al.*, 2001). The wild-type of *Listeria* is observed to move with a constant velocity but *Listeria* mutant ActA $_{\Delta 21-97}$  shows oscillatory motion with a period around 100 sec. This *Listeria* mutant is named "hopping *Listeria*". (see Fig. 1.5)

Actin based motility has been shown to be more general than initially thought: movement of the Gram-positive *L. monocytogenes*, the Gram-negative *Shigella flexneri* (Clerc and Sansonetti, 1987), the vaccinia virus (Cudmore *et al.*, 1995) are all based on the formation of an actin tail.

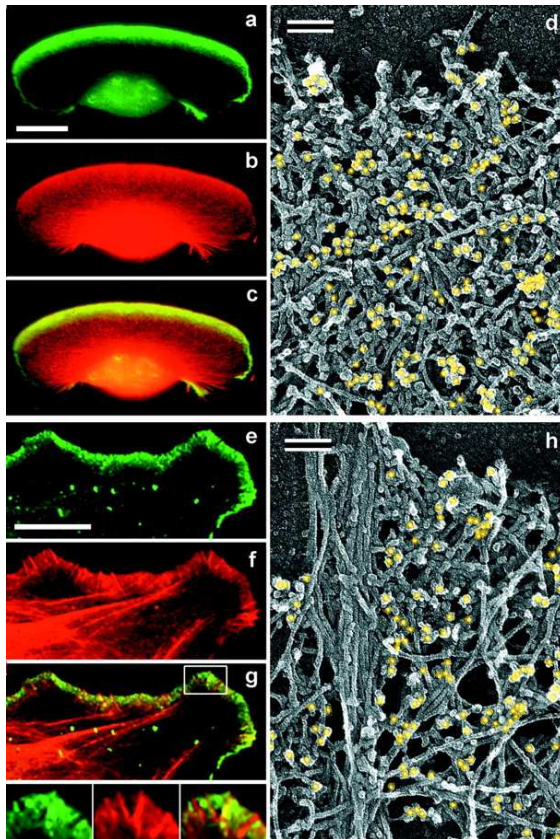


**Figure 1.4** Organization of actin filaments and localization of Arp2/3 complex in lamellipodia. (a-c and e-g) Fluorescence microscopy of *Xenopus* keratocyte (a-c) or fibroblast (e-g). Staining with p21 antibody (green) and TRITC-phalloidin (red) shows Arp2/3 complex highly enriched in lamellipodia. Boxed region in g is enlarged in insets; it shows several filopodia lacking and only one filopodium containing Arp2/3 complex. (d and h) Immuno-EM of lamellipodia of *Xenopus* keratocyte (d) or fibroblast (h) stained with p21 primary antibody and 10-nm gold-conjugated secondary antibody after glutaraldehyde fixation and SDS treatment of detergent-extracted cells. Gold particles are highlighted in yellow. Bars: (a and e) 10  $\mu\text{m}$ ; (d and h) 0.1  $\mu\text{m}$ . This figure is from the paper by Svitkina and Borisy (1999).

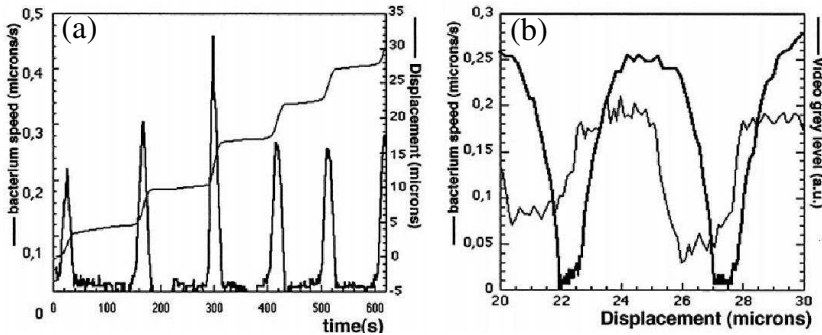


**Figure 1.5** (a) Kinematics record of the mutant *ActA* $_{\Delta 21-97}$  (hopping *Listeria*): Speed and position of bacteria as functions of time. (b) Speed and measurement of the video grey level intensity along the tail of the snapshots at time 108 s as a function of the position. These figures are from the paper by Gerbal *et al.* (2000a).

Transmembrane protein, ActA, is distributed asymmetrically on the surface of *Listeria*. The presence of ActA, has been shown to be required and sufficient to trigger actin polymerization and thus motility (Kocks *et al.*, 1993). Infected medium provides all the other necessary proteins like actin, cross-linkers (such as  $\alpha$ -actinin) and Arp2/3.

Using *Listeria* as a model system for studying the biochemistry of actin-based movement, suffers from the fact that geometrical parameters such as its size and shape are predetermined, and the surface density of the Arp2/3 complex activator (ActA) is unknown. Biophysical studies on movement induced by actin polymerization were greatly facilitated by the development of *in vitro* systems that explore actin-driven motility of non-biological cargos such as protein coated beads (Cameron *et al.*, 1999) and vesicles (Upadhyaya *et al.*, 2003) placed in cell extracts. These *in vitro* systems, when coated with either ActA or WASP proteins, move much the same way as the pathogens. Polystyrene beads coated with purified ActA protein can undergo directional movement in an actin-rich cytoplasmic extract (Fig. 1.6). Thus, the actin polymerization-based motility generated by ActA can be used to move non biological cargos, as has been demonstrated for classical motor molecules such as kinesin and myosin. Initiation of unidirectional movement of a symmetrically coated particle is a function of bead size and surface protein density. Small beads ( $< 0.5 \mu\text{m}$  in diameter) initiate actin-based motility when local asymmetries are built up by random fluctuations

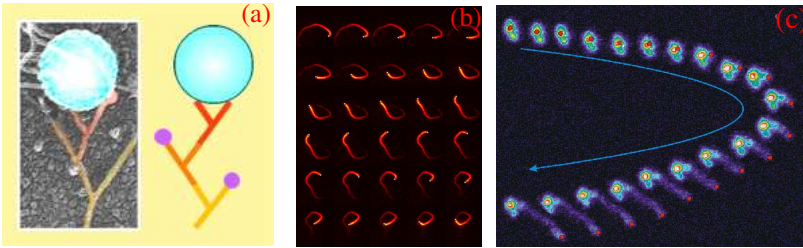


**Figure 1.6** (a) ActA coated bead is riding on an actin tail with dendritic organization. (b) A serial image sequence, captured every thirty seconds of .5-micron bead coated with the ActA protein. (c) Graphical representation of an actual ActA-coated latex sphere undergoing the transition from a bead (red circle) symmetrically coated with actin (pseudocolor) to a bead being propelled by an actin comet tail. These figures are from the papers by Cameron *et al.* (1999) and Van Oudenaarden and Theriot (1999).

of actin filament density or by thermal motion, demonstrating the inherent ability of the dynamic actin cytoskeleton to spontaneously self-organize into a polar structure capable of generating unidirectional force. Larger beads (up to  $2 \mu\text{m}$  in diameter) can initiate movement only if surface asymmetry is introduced by coating the beads on one hemisphere. This explains why the relatively large *L. monocytogenes* requires polar distribution of ActA on its surface to move. These *in vitro* systems have several advantages: the number of essential proteins is small; their structures, concentrations and localizations are known; the reaction rates of the actin dynamics have been measured (Loisel *et al.*, 1999; Pollard and Borisy, 2003); and the force generated by the actin comet is also measured (Marcy *et al.*, 2004; Parekh *et al.*, 2005).

## Mathematical modelling

The challenge in understanding the physical mechanism of force generation by actin assembly has given rise to various theoretical descriptions. The process of protrusion is based on the polymerization of actin into a two-stranded polar helix with barbed and pointed ends having fast and slow dynamics, respectively (Pollard, 1986). The monomers bind ATP, and ATP hydrolysis results in the filament's dynamic asymmetry and treadmilling (net depolymerization from the pointed end balanced by net polymerization onto the barbed end with monomers simply being recycled by diffusion)

(see Fig. 1.7). Protrusion is based on the treadmilling of the polar actin arrays, rather than of the individual filaments. What determines the fast rate of treadmilling of these arrays and how do they self-organize? What is the nature of the protrusive force?

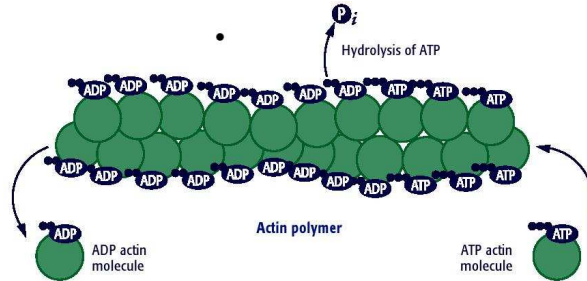


**Figure 1.7** A schematic presentation of actin treadmilling, i.e. simultaneous association and dissociation of actin molecules from an actin filament. The figure is from the website <http://bbri.org/>.

Equilibrium polymerization was first modelled quantitatively by Oosawa and Asakura (1962) and treadmilling predicted mathematically by Wegner (1976). Thermodynamics was used by Hill (1981a) to demonstrate that a polymerizing filament can generate force in the piconewton range. Later on, Peskin *et al.* (1993) formulated a *Brownian ratchet theory* for how a growing polymer could exert an axial force. This theory explained how such force can be generated: even when a resisting force is applied to the object in front of the filaments tip, the object can still diffuse away, creating a gap sufficient for monomers to intercalate and assemble onto the tip, thereby inhibiting the object from diffusing backward. In this model, polymers are assumed to be infinitely stiff, such that the Brownian motion of the load alone creates a gap sufficient for monomers to intercalate between the tip and the load. Consequently, it predicts that the bacterial velocity should depend on its diffusion coefficient, and as a result on its size. However, experiments failed to show such a size dependence: *Listeria* and *Shigella* move at the same speed despite their very different sizes (Goldberd and Theriot, 1995). The actin network at the leading edge of lamellipodia is organized into an orthogonal network (Small *et al.*, 1995). This is unexplained by the *Brownian ratchet model*, which treats only collinear filament growth. To remove these limitations, Mogilner and Oster (1996a) have generalized the *elastic ratchet model* to include the elasticity of the polymer and to relax the collinear structure of growing tips. The principle result of

this model was an expression for the effective polymerization velocity of a growing filament as a function of the load force  $F_{\text{load}}$  it is working against

$$v_p = v_p^{\text{max}} \exp(-\delta F_{\text{load}}/k_B T), \quad (1.1)$$

in which  $\delta = 2.7$  nm is the actin monomer size and  $v_p^{\text{max}}$  is the free polymerization velocity. They used this expression to describe the propulsion of *Listeria* and the protrusion of lamellipodia. But, as we discuss in the next section, experimental data soon revealed its limitations.

## Tethered ratchet model

On the basis of observations that the actin filaments are flexible rather than rigid, an *elastic ratchet model* suggested that a filament's own thermal undulations can create a gap between its tip and the load (Mogilner and Oster, 1996a). Subsequent monomer assembly increases the fibers length so that when the tip contacts the load the polymer is bent; the resulting elastic force pushes on the load. In these models, which are based on the behavior of individual filaments, the actin binding energy drives protrusion. ATP hydrolysis is not utilized directly in the force generation but is necessary for treadmilling.

But this model faces the following shortcomings. First, actin filaments responsible for protrusion are not actually independent, but are rather parts of the dendritic network (Pollard and Borisy, 2003). Second, one-filament models cannot really describe the complex geometry of the actin network leading edge impinging on the curved cell membrane or bacterial surface. Third, experimental data (Cameron *et al.*, 2001; Kuo and McGrath, 2000) indicated that the filaments are attached to the surface they push. Now the question is: How can the ratchet model work if the filaments are attached to the surface? Mogilner and Oster (2003) introduced the *tethered ratchet model* which answers this question by assuming that the filaments attach transiently to the surface of the obstacle via protein complexes. However, they soon dissociate and grow until they lose contact with the surface after capping. The attached fibers are in tension and resist the protrusion, whereas the dissociated fibers are in compression and generate the force of propulsion (see Fig.1.8).

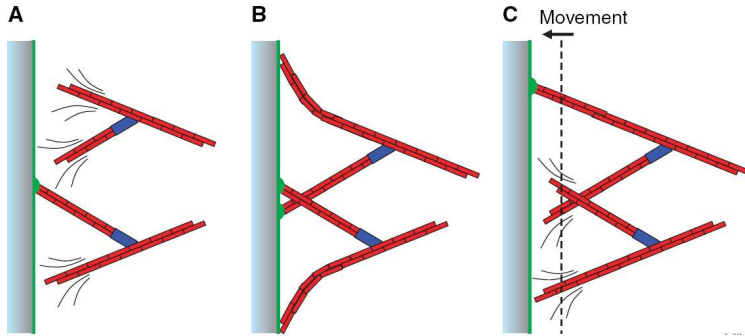


**Figure 1.8** Tethered ratchet model of propulsion. Actin filaments (red) grow by branching as mediated by the Arp2/3 complex (blue). (A) Some filaments are attached to the load surface which is coated with ActA (green). Other unattached filaments are free to polymerize. (B) Thermal fluctuations cause the polymerizing filaments to bend away from the load. (C) Once the elongated filaments attach to the load, they are under compression and their subsequent relaxation provides the propulsive force and can move the object forward. The attached filaments detach and are free to polymerize. This figure is from the paper by Upadhyaya and Oudenaarden (2004).

## Elastic continuum model

Operating on a much larger length scale than the microscopic models, the elastic propulsion theory treats the actin tail as an elastic continuum gel (Gerbal *et al.*, 2000a). Experimental evidence suggests that the actin mesh around the object behaves like an elastic gel (Gerbal *et al.*, 2000b). Based on experimental results showing that *Listeria* are connected to their tail and using the measured value of the Young's modulus ( $Y = 10^3 - 10^4$  Pa) of the actin tail, a macroscopic elastic propulsion model suggested that the curved surface is not merely pushed, but is rather squeezed forward by an elastic stress. This model is formulated at a mesoscopic scale at which the actin tail gel is viewed as a continuous medium and does not consider explicitly the microscopic mechanism of force generation at the surface. The squeezing stress develops when the growth of actin at the surface pushes the actin gel outward, stretching it and generating tangential tension balanced by radial compression at the surface (Fig. 1.9).

This model assumes that there is an effective friction between the gel and surface. Similar to the microscopic models, the elastic propulsion model

predicts a balance between the pushing elastic and pulling friction forces on the surface. It describes the complex system of *Listeria* by a two-gel model to illustrate the main features of the propulsion mechanism. This approach makes a few assumptions about the microscopic mechanism at work in the polymerization/reticulation process; it can, in principle, be used with any microscopic mechanism. The internal forces exerted on the bacteria surface predicted by this model lead to a simple understanding of the oscillatory motion (Fig. 1.5) of the *Listeria* mutant ActA $_{\Delta 21-97}$ : at the microscopic level the mutation of the ActA gene changes the connection kinetics of the links between the gel and the bacterium surface. It corresponds, at a physical or macroscopic level, to a modification of the surface properties, change in the polymerization rate and the effective friction between the gel and the bacterium. This can induce a stick-slip transition, resulting in the oscillatory motion of the mutant. This model succeeds in reproducing the experimental data of its motion. It predicts that the strength of linkage between the mutant and the tail should be stronger during its slow phase and weaker during its rapid displacement.

On the other hand, growth of filaments on a flat surface will not lead to a build-up of stress, as described in Fig. 1.9. The results of Schwartz *et al.* (2004) show that curvature-derived stresses may not be critical for movement. They used flat disks (made by compression of polystyrene beads) coated uniformly with ActA in cell extracts to reconstitute *Listeria*-like motility. They find that the disks move through extracts with comet tails in a manner similar to *Listeria*, beads and vesicles. Furthermore, particles with tails on their curved perimeters are observed to hop, but disks with face tails move steadily, suggesting that curvature of the load is required for hopping. Hopping has been observed previously for spherical beads in purified protein solutions (Bernheim-Groswasser *et al.*, 2005) and was found to be in agreement with a curvature-induced build-up of stress (Gerbai *et al.*, 2000a). The period of velocity oscillations with beads differs by one order of magnitude (8-15 min) from *Listeria*.

In chapter. 5, we present our simple model of actin-based motility for a flat obstacle. The model which is formulated on the single filament level, predicts that for a given set of parameters, changing the attachment rate of filaments drives the system from a stationary to a saltatory movement. Our results agree well with respect to velocity spike amplitude and periods in *Listeria* experiments (see Fig. 5.5a). It also predicts that curvature of the obstacle is not necessary for “hopping”, which is in contradiction with the recent results by Schwartz *et al.* (2004). It seems that more experiments on flat obstacles, for a broad range of parameters, needs to be done.

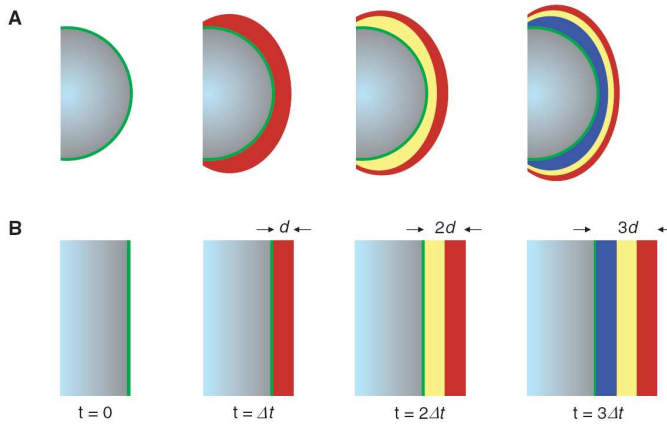


**Figure 1.9** Curvature-induced elastic stress development. (A) A curved object coated with ActA (green) polymerizes actin on its surface. The first layer of actin is depicted in red. As the subsequent layer (yellow) grows on the surface of the object, it displaces the first layer and causes it to stretch. The growth of the next layer (blue) causes the previous layers to be further stretched. This leads to a compressive force on the bead. (B) Actin polymerizing on a flat object coated with ActA on one surface. In a time interval the thickness of the gel increases by  $d$ . Successive layers are not stretched and therefore do not generate a compressive stress. This is in contrast to the curved object where the thickness of older layers decreases as each new layer is added. This figure is from the paper by Upadhyaya and Oudenaarden (2004).

## 1.2 The wormlike chain model

Many important biopolymers, like actin, microtubules, and DNA, are stiff meaning that their persistence length  $\ell_p$  is several orders of magnitude larger than the microscopic scale defined by the backbone diameter or monomer size  $a$ . The theoretical understanding of the mechanical properties of a single stiff macromolecule in isolation is already a nontrivial statistical mechanics problem with quite a number of recent developments 50 years after it was first formulated (Kratky and Porod, 1949). In contrast to flexible polymers, which are usually theoretically represented by highly coarse grained, effective models such as the fractal Gaussian chain, stiff polymers can be modeled more realistically by the so-called wormlike chain model: an inextensible contour with a resistance to bending quanti-

fied by the persistence length  $\ell_p$ , which is the characteristic decay length of tangential correlations under the influence of thermal forces. The filament is represented by an inextensible space curve  $\mathbf{r}(s)$  of total length  $L$  parametrized in terms of the arc length  $s$  (Fig. 1.10a). The statistical

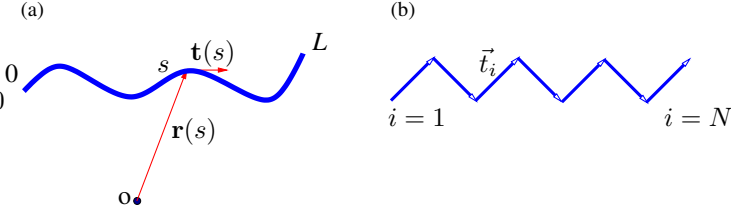


**Figure 1.10** Sketch of the wormlike chain as (a) a differentiable space curve  $\mathbf{r}(s)$  of a contour length  $L$  parametrized by arc length  $s$  and (b) a succession of  $N$  segments  $\vec{t}_i$ , whose direction is tangent to the polymer contour at the  $i$ th segment.

properties of the wormlike chain are determined by a free energy functional which measures the total elastic energy of a particular conformation. The elastic energy of a given configuration  $\mathbf{r}(s)$ , parametrized in terms of the arc length  $s \in [0, L]$ , is given by

$$\mathcal{H} = \frac{\kappa}{2} \int_0^L ds \left( \frac{\partial \mathbf{t}(s)}{\partial s} \right)^2, \quad (1.2)$$

where  $\mathbf{t}(s) = \partial \mathbf{r}(s) / \partial s$  is the tangent vector. The energy functional is quadratic in the local curvature with  $\kappa$  being the bending stiffness of the chain. The inextensibility of the chain is expressed by the local constraint,  $|\mathbf{t}(s)| = 1$ , which leads to non-Gaussian path integrals. Since there would be high energetic costs for a chain to fold back onto itself one may safely neglect self-avoidance effects for sufficiently stiff chains.

Despite the mathematical difficulty of the model some quantities can be calculated exactly. Among these is the tangent-tangent correlation function which decays exponentially,  $\langle \mathbf{t}(s) \cdot \mathbf{t}(s') \rangle = \exp[-(s - s') / \ell_p]$ , with the persistence length  $\ell_p = \kappa / k_B T$ . Another example is the mean-square end-to-end distance

$$\begin{aligned} \mathcal{R}^2 &:= \langle R^2 \rangle = 2\ell_p^2 (e^{-L/\ell_p} - 1 + L/\ell_p) \\ &= \begin{cases} L^2 & \text{for } L/\ell_p \rightarrow 0 \text{ (rigid rod)} \\ 2\ell_p L & \text{for } L/\ell_p \rightarrow \infty \text{ (random coil)}, \end{cases} \end{aligned} \quad (1.3)$$

which reduces to the appropriate limits of a rigid rod and a random coil (with Kuhn length  $2\ell_p$ ) as the ratio of  $L$  to  $\ell_p$  tends to zero or infinity, respectively. The calculation of higher moments quickly gets very troublesome (Hermans and Ullman, 1952).

Rigorous analytical calculations within the wormlike chain model are essentially limited to perturbation calculations for weakly bending rods  $L < \ell_p$ , but this limit captures the most important property of the model.

It is also possible to define a discrete form of the worm like chain model. In this framework, a polymer conformation is represented by a succession of  $N$  segments  $\vec{t}_i$ , whose direction is tangent to the polymer contour at the  $i$ th segment (Fig. 1.10b). Since the polymer is assumed to be inextensible, all segments  $\vec{t}_i$  have a prescribed length  $a = L/N$ . The Hamiltonian in the presence of constant external force  $\vec{f}$  is given by

$$\frac{\mathcal{H}}{k_B T} = -\frac{\lambda a^2}{k_B T} \sum_{i=1}^N \hat{t}_i \cdot \hat{t}_{i+1} - \sum_{i=1}^N \frac{\vec{f} a}{k_B T} \cdot \hat{t}_i, \quad (1.4)$$

where  $\hat{t} = \vec{t}/a$  and  $\lambda a^2/k_B T$  is the (dimensionless) energy associated with each bond.  $\lambda$  is chosen such that to reproduce the energy of a semiflexible polymer of persistence length  $\ell_p$ . The relation in  $d$  dimensions is computed to

$$\exp(-L/\ell_p) = \left[ \frac{I_{d/2}(K)}{I_{d/2-1}(K)} \right]^N \quad (1.5)$$

with  $K = \lambda a^2/k_B T$  and  $I_\nu$  as modified Bessel function of first kind.

Continuum limit can be obtained for  $a \rightarrow 0$ ,  $N \rightarrow \infty$ , with  $Na = L$  and  $\lambda a^3$  held fixed. Since  $K = (\lambda a^3)/(a k_B T)$  and  $\lambda a^3$  is finite, small  $a$  is equivalent to large  $K$ . In the limit of large  $K$ , Eq. 1.5 reduces to

$$\ell_p = \frac{2}{d-1} \frac{KL}{N} = \frac{2}{d-1} \frac{\lambda a^3}{k_B T} \quad (1.6)$$

The Hamiltonian is then equivalent to the following functional

$$\mathcal{H} = \frac{\kappa}{2} \int_0^L ds \left( \frac{\partial \mathbf{t}(s)}{\partial s} \right)^2 - \vec{f} \cdot \int_0^L ds \mathbf{t}(s), \quad (1.7)$$

where  $\kappa = 2/(d-1)\lambda a^3$ .

### 1.3 Non-linear force-extension relation

A useful property of the wormlike chain model, which can be computed exactly is the linear force extension. Consider a semiflexible polymer with

contour length  $L$  and persistence length  $\ell_p$  which is grafted at one end in  $\hat{z}$  direction. The other free fluctuating end is pulled by an external force  $\mathbf{f} = f\hat{z}$  (Fig. 1.11).

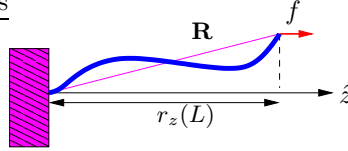


**Figure 1.11** A semiflexible polymer is grafted in one end and the other free fluctuating end is pulled by an external force  $f$  in  $\hat{z}$  direction.  $R$  is the end-to-end distance of the polymer and  $r_z(L)$  is the projection of  $R$  in  $\hat{z}$  direction.

The non-linear force extension relation of the filament in the weakly bending approximation has been calculated in Sec. 2.3.2 and looks like (Ghomi *et al.*, 2006)

$$\langle r_z(L) \rangle_f = L \left( 1 - \frac{L(d-1)}{4\ell_p} \frac{\tanh \sqrt{fL_{\parallel}/k_B T}}{\sqrt{fL_{\parallel}/k_B T}} \right), \quad L_{\parallel} = L^2/\ell_p, \quad (1.8)$$

where  $f$  is the external force exerted on the free fluctuating end of the filament in the graft direction and  $r_z(L)$  is the end-to-end distance of the filament projected in  $\hat{z}$  direction.  $d$  is the dimension of the embedding space.

In the limit of small external forces, this reduces to

$$\langle r_z(L) \rangle_f = L \left[ 1 - \frac{d-1}{4} \frac{L}{\ell_p} + \frac{d-1}{12} \left( \frac{L}{\ell_p} \right)^2 fL \right], \quad (1.9)$$

which identifies  $\mathbf{R}_{\parallel}$  (the  $z$  projection of the equilibrium end-to-end distance of the filament  $\mathbf{R}$  in the absence of external forces) as  $L[1 - (d-1)L/4\ell_p]$  and the effective linear spring constant  $k_{\parallel} = 12\kappa^2/(d-1)k_B T L^4$ . For strong stretching forces, the extension saturates asymptotically as

$$\langle r_z(L) \rangle_f = L \left[ 1 - \frac{L(d-1)}{4\ell_p \sqrt{fL_{\parallel}}} \right], \quad (1.10)$$

which agrees with results by Marko and Siggia (1995).

In the limit of large compressive forces, the weakly bending rod approximation breaks down. The non-linear response of the polymer to compressive forces (as well as extension forces) can be obtained from the probability

distribution of the tip position (Frey *et al.*, 1998). The probability distribution of a grafted semiflexible polymer in the  $z$  direction has the scaling form (see Sec. 2.3.3)

$$P_{\parallel}(z, L, \ell_p) = L_{\parallel}^{-1} \tilde{P}_{\parallel}(\tilde{\rho}), \quad (1.11)$$

where we have introduced the scaling variable

$$\tilde{\rho} = \frac{L - z}{L_{\parallel}} \quad (1.12)$$

measuring the compression of the filament in units of  $L_{\parallel}$ . In three dimensions, one finds (see Sec. 2.3.3)

$$P_{\parallel}(\tilde{\rho}) = \begin{cases} \pi \exp(-\frac{1}{4}\pi^2 \tilde{\rho}) & \tilde{\rho} \geq 0.3 \\ \frac{1}{\sqrt{\pi \tilde{\rho}^3}} \exp(-\frac{1}{4\tilde{\rho}}) & \tilde{\rho} < 0.3 \end{cases}. \quad (1.13)$$

Now we calculate the moment generating function by a Laplace transform

$$\begin{aligned} P_{\parallel}(f) &:= \langle e^{-f(L-r_z(L))/k_B T} \rangle_0 = \int_0^L dz e^{-f(L-z)/k_B T} P_{\parallel}(z) \\ &= \int_0^{L/L_{\parallel}} d\tilde{\rho} e^{-fL_{\parallel}\tilde{\rho}/k_B T} P_{\parallel}(\tilde{\rho}). \end{aligned} \quad (1.14)$$

Then, the force-extension relation is given by

$$\langle r_z(L, f) \rangle = L + k_B T \frac{\partial \ln \mathcal{P}_{\parallel}(f)}{\partial f}. \quad (1.15)$$

The results of numerically evaluating Eq. (1.15) using Eqs. 1.13, 2.20 are presented in Fig. 1.12a for different values of  $\epsilon = L/\ell_p$ .

Also shown in Figs. 1.12b,c,d are the results from the Monte Carlo (MC) simulations at different intervals of  $fL/k_B T$ . We used MC data for the probability distribution of the tip in  $z$  direction,  $P_{\parallel}(z)$ , to calculate numerically the integral in Eq. 1.14 for different values of  $\epsilon = L/\ell_p$ . The MC simulations have been performed according to the standard Metropolis algorithm for a chain with  $N = 50$  identical segments (see Appendix A). We found a good agreement between analytical results and MC data for intermediate (semiflexible polymers) and even large values of  $\epsilon$  (flexible polymers). For stiff filaments ( $\epsilon \ll 0.1$ ), the deviations for compressing forces are significant due to the weak statistics of MC data at small values of  $z$ . The probability to find the tip of the stiff polymer at small values of  $z$

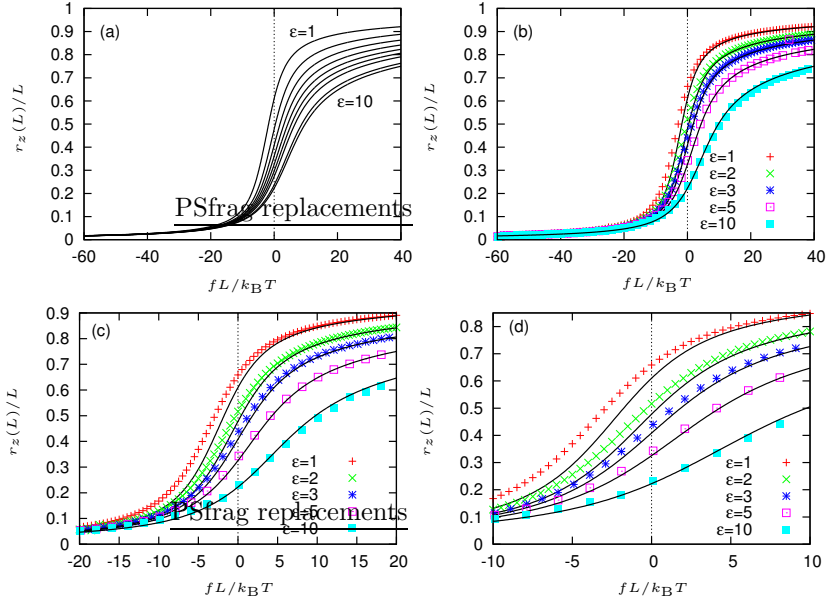


**Figure 1.12** (a)  $\langle r_z(L) \rangle / L$  as a function of the dimensionless force  $fL/k_B T$ . The curves are for different values of  $\epsilon = L/\ell_p = 10, \dots, 1$  with steps of size 1 (Frey *et al.*, 1998). (b), (c), (d) Results of MC simulations are plotted in different intervals of  $fL/k_B T$ . Deviations from analytical results due to the lack of simulation time is pronounced for semiflexible ( $\epsilon \sim 1$ ) and stiff filaments ( $\epsilon \ll 1$  which are not presented here).

is very small, since these configurations are strongly suppressed. Although this probability is negligible, but it is not exactly zero. At small values of  $z$ ,  $P_{\parallel}(z)$  is small but  $e^{-f(L-z)}$  ( $f$  negative) can be large, so their multiplication is not necessary small. Indeed, our MC data vanishes at small values of  $z$  which for compressing forces, has important contribution to the integral in Eq. 1.14. One may need to run MC simulations for longer times in order to get a better statistics of  $P_{\parallel}(z)$  at small values of  $z$ .

Finally, we also note the result for the linear response of a semiflexible polymer which is grafted at one end (in  $\hat{z}$  direction) and the other end is pulled out by a small force  $f\hat{n}$  with  $\vartheta$  to be the angle between  $\hat{z}$  and  $\hat{n}$  (Fig. 1.13).

The force coefficient is markedly angle dependent and in two dimensions

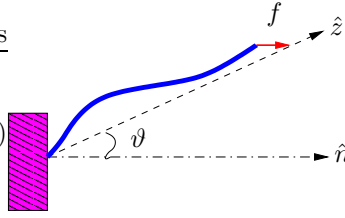


**Figure 1.13** A pulling force  $f\hat{n}$  acts on the free fluctuating end of a semiflexible polymer which is grafted in  $\hat{z}$  direction.

is given by (Kroy, 1998; Kroy and Frey, 1996)

$$\begin{aligned}
 k_{\parallel}^{-1}(\vartheta) &= \frac{4\ell_p^2}{k_B T} \left[ \frac{1}{2} \frac{L}{\ell_p} + e^{-L/2\ell_p} - 1 \right. \\
 &+ \cos 2\vartheta \left( \frac{1}{4} + \frac{1}{12} e^{-2L/\ell_p} - \frac{1}{3} e^{-L/2\ell_p} \right) \\
 &\left. - \cos^2 \vartheta (e^{-L/2\ell_p} - 1)^2 \right]. \quad (1.16)
 \end{aligned}$$

In three dimensions,  $k_{\parallel}^{-1}(\vartheta)$  changes to (Kroy, 1998)

$$\begin{aligned}
 k_{\parallel}^{-1}(\vartheta) &= \frac{\ell_p^2}{k_B T} \left[ \frac{2}{3} \frac{L}{\ell_p} - \frac{5}{9} + \frac{1}{18} e^{-3L/\ell_p} + \sin^2 \vartheta e^{-L/\ell_p} \right. \\
 &\left. + \frac{1}{6} \cos 2\vartheta (e^{-3L/\ell_p} + 2) - \cos^2 \vartheta (e^{-L/\ell_p} - 1)^2 \right]. \quad (1.17)
 \end{aligned}$$

## 1.4 Objective of this thesis

In this thesis, we aim to build up a simple model of actin-based motility on the single filament level. We assume that filaments can attach to the surface of the obstacle with a constant rate and detach with a force dependent rate. While the free fluctuating length of detached filaments grow by a force dependent polymerization velocity (Eq. 1.1), it decreases by crosslinking of both attached and detached filaments in the stiff part of the actin gel. A detached filament which is grafted at distance  $\zeta$  with respect to the obstacle and has free fluctuating length  $l_d$ , performs thermal fluctuations in the presence of the obstacle. Since the number of possible configurations of the filament is decreased or its free energy has been increased, it exerts a force

on the obstacle which is pure entropic in origin. Hence, the following question arises: how does the magnitude of this force depend on  $l_d$ ,  $\zeta$ ,  $\ell_p$  and  $\vartheta$ ? Here,  $\ell_p$  is the persistence length and  $\vartheta$  is the filament orientation. To address this question, first, we analytically solve this problem in the weakly bending approximation which is a valid approximation for stiff filaments ( $l_d \ll \ell_p$ ). In the next step, we perform extensive Monte Carlo simulations to check the validity range of our analytical calculations. We found that there is a nice agreement between our analytical results and MC simulations for stiff filaments and the results start to deviate as the persistence length of filament becomes comparable to its contour length (semiflexible polymers). Our MC simulations also reproduces the already known results for flexible polymers like the gaussian distribution of end-to-end distance (see Chapter. 2).

On the other hand, attached filaments which are attached to the obstacle via some linker proteins, most the time pull back the obstacle. Obviously, this pulling force will depend on the contour length of attached filament, its persistence length, its orientation and eventually on the spring constant of the linker protein. We include the presence of the linker protein in the non-linear force extension relation (Sec. 1.3) in order to calculate the pulling force of attached filaments (see Appendix D).

We use the results of our calculations for pushing and pulling forces as a main ingredients to build up our simple theoretical description of actin-based motility. We show that attachment and detachment of actin filaments to the obstacle, polymerization at the filament's free ends and cross-linking of the actin network lead to spontaneous oscillations of the obstacle velocity (Chapter 5).

We also use the analytical results obtained for pushing force of detached filaments to calculate numerically the total entropic force exerted by a homogeneous actin network on a sphere. These calculations may serve as a prerequisite for modelling actin-based motility in *in vitro* experiments using curved obstacles like beads and vesicles (Chapter 3).

At the end, part of this thesis is also dedicated to our numerical results obtained for steric interactions between two biopolymers fluctuating parallel or perpendicular to each other with different boundary conditions. This is the situation that one often encounters in cell cytoskeleton. We also compare the results obtained from Monte Carlo simulations to our analytical calculations (Chapter 4).



## 2 Entropic forces exerted by a grafted polymer on a wall

This chapter has been published as: A. Gholami, J. Wilhelm, and E. Frey: *Entropic forces generated by grafted semiflexible polymers*, Phys. Rev. E. **74**, 41803 (2006). More Monte Carlo results in 3d are added.

### Abstract

The entropic force exerted by the Brownian fluctuations of a grafted semiflexible polymer upon a rigid smooth wall are calculated both analytically and by Monte Carlo simulations. Such forces are thought to play an important role for several cellular phenomena, in particular, the physics of actin-polymerization-driven cell motility and movement of bacteria like *Listeria*. In the stiff limit, where the persistence length of the polymer is larger than its contour length, we find that the entropic force shows scaling behavior. We identify the characteristic length scales and the explicit form of the scaling functions. In certain asymptotic regimes, we give simple analytical expressions which describe the full results to a very high numerical accuracy. Depending on the constraints imposed on the transverse fluctuations of the filament, there are characteristic differences in the functional form of the entropic forces. In a two-dimensional geometry, the entropic force exhibits a marked peak.

### 2.1 Introduction

In a cellular environment, soft objects like membranes and polymers are subject to Brownian motion. As a result there are interactions between them which are entropic in origin, i.e. a consequence of constraints imposed on the Brownian fluctuations. For example, two parallel membranes repel each other entropically with a potential that falls off like a power law in the distance between them (Helfrich, 1978). Similarly, thermally fluctuating biopolymers like F-actin and microtubules may exert entropic forces

on membranes or some other obstacles; for an illustration see Fig. 5.1. Though due to the same thermal fluctuations, such forces have to be dis-

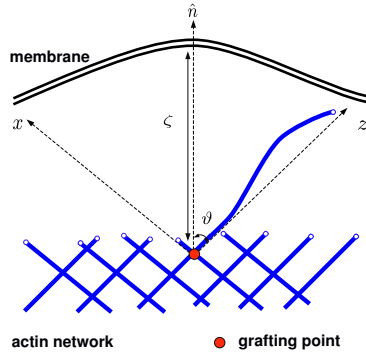


**Figure 2.1** A membrane constrains the Brownian fluctuations of a semiflexible polymer grafted parallel to the z-axis resulting in an entropic force on the membrane. The membrane, for simplicity, has been considered as a rigid smooth wall.

tinguished from forces obtained by pulling on a biopolymer (Fixman and Kovac, 1973; Kovac and Crabb, 1982; Marko and Siggia, 1995; Benetatos and Frey, 2004). It turns out that the force-distance curves of these two cases have no resemblance at all in a regime where thermal fluctuations play a role, which is generically the case for all cytoskeletal filaments. Both types of forces are thought to play a prominent role in cell motility and movement of pathogens like *Listeria monocytogenes*, that propel itself through the cytoplasm of infected cells by constructing behind it a polymerized tail of cross-linked actin filaments (Marcy *et al.*, 2004). Similarly, in a crawling cell, the force generated from the polymerization of a collection of actin fibers is responsible for the protrusion of cell membrane, which are known as lamellipodia, filopodia, or microspikes according to their shapes (Bray, 2001). It seems that polymerizing networks of actin filaments are capable of exerting significant mechanical force, which are used by eukaryotic cells and their prokaryotic pathogens to change shape or move.

In this chapter, we will not enter into the debate on the particular force generating mechanism responsible for all these different types of cell motility. It seems plausible to us that a final model for a particular biological system may be a macroscopic viscoelastic model of the actin gel (Gerbal *et al.*, 2000a,b) combined with elements from a microscopic elastic Brownian ratchet (EBR) model of the growing edge of the network (Mogilner and

Oster, 1996a,b). The first one is a continuum model of *Listeria* propulsion relying on the elastic shear stress developed by growth of the actin meshwork at the cell surface. In the EBR model, which is based on the behavior of individual actin filaments, thermal bending undulations of semiflexible actin fibers create the polymerization gap and the entropic force of the growing filaments pushes the bacterium forward or deforms the cell membrane. It seems that a detailed analysis of the entropic forces which fluctuating stiff polymers exert on rigid walls may serve as an important input for future molecular models of force generation in cellular systems. The length of the thermally fluctuating parts of these polymers are typically  $200 \sim 300$  nm, which is very short compared to their persistence length  $\ell_p \approx 15 \mu\text{m}$  (LeGoff *et al.*, 2002), such that an analysis which considers these filaments as stiff seems appropriate. For microtubules, whose persistence length ranges from  $110 \mu\text{m}$  to  $5\text{mm}$  when  $L$  is varied between  $2.6$  and  $47.5 \mu\text{m}$  (Pampaloni *et al.*, 2006), the analysis should even work better.

We consider the idealized situation illustrated in Fig. 5.1, where one end of a semiflexible polymer is fixed both in position and orientation to some rigid support, e.g. the dense part of an actin gel. We choose coordinates such that the grafted end is at the origin with the tangent fixed parallel to the  $z$ -axis. The membrane or obstacle is considered as a rigid, smooth wall orthogonal to the  $x$ - $z$ -plane at a distance  $\zeta$  from the origin. Let  $\vartheta$  be the angle between the  $z$ -axis and the normal  $\hat{n}$  of the wall. If  $\zeta$  is small enough, the wall will constrain the Brownian fluctuations of the polymer leading to an increase in free energy with respect to the unconstrained polymer. On time scales larger than the equilibration time of the grafted polymer, this results in an average force  $f$  exerted on the wall. In this paper we will calculate how the entropic force  $f$  depends on the geometric parameters  $\zeta$ ,  $\vartheta$ , the contour length  $L$  and the persistence length  $\ell_p$  of the polymer, and the dimensionality of the embedding space.

Polymers confined to two dimensions is a situation frequently encountered in *in vitro* experiments but also of relevance for actin filaments in the confined space of a lamellipodium. We find that in this case the entropic force shows a pronounced maximum as a function of the compression of the polymer,  $L - \zeta$ , for a broad range of stiffness parameters  $\varepsilon = L/\ell_p \leq 4$ . The magnitude of the maximum force exceeds the value of the Euler buckling force  $f_c = \frac{\pi^2}{4} \frac{\ell_p k_B T}{L^2}$  by a factor between 2 and 3. These results are quite distinct from the behavior of a polymer which is free to fluctuate in three dimensions. Then, the entropic force is a monotonic function of the compression and exceeds the buckling force only in the nonlinear regime for strong compressions.

In the branched actin network formed in lamellipodia, the Arp2/3 complex is responsible for the nucleation of new filaments. It is found that the angle relative to the parent filament is  $2\vartheta \approx 70^\circ$  (Small *et al.*, 1995). It has been asked (Mogilner and Oster, 1996a,b) whether this angle corresponds to an optimal angle with respect to the entropic force generated by a fluctuating filament. Indeed, we do find that there is such an optimal angle for a homogeneous network pushing against a flat membrane (see section 2.5), but this angle is much larger, ranging in the interval  $2\vartheta \in [120^\circ, 150^\circ]$ . This angle differs from previous estimates (Mogilner and Oster, 1996a,b) mainly since they were based on an incorrect value for the persistence length of actin. It would, however, be overhasty to conclude that the branching angle is not optimized for maximal force production since the simplified model in section 2.5 leaves out important physics such as the polydispersity in filament length and the thermal fluctuations of the membrane.

We proceed as follows: Section 2.2 serves to introduce and discuss the various types of thermodynamic forces which can be generated by fluctuating semiflexible polymers. We arrive at the conclusion that the entropic forces discussed above are closely related to the probability distribution of the free end of the clamped polymer. In Section 2.3, we start our analysis of entropic forces with a polymer grafted perpendicular to the wall. This chapter contains a definition of the wormlike chain model and the basic idea of our analytical calculations, which starting from the tip distribution calculates the restricted free energy and the entropic force. The analysis is complemented by Monte Carlo (MC) simulations, which both show the range of validity of the analytical results and the crossover from semiflexible to Gaussian chains. Details of the calculations are deferred to the Appendices C.1, C.2 and C.3. Section 2.4 treats the technically more complicated case of a polymer inclined at an angle  $\vartheta$  with respect to the wall. Here, we obtain the entropic forces analytically up to the numerical evaluation of some integrals. For some asymptotic cases explicit analytical formula are obtained. The MC simulations in this chapter are restricted to a parameter range which is close to the stiff limit and mainly serve the purpose to define the range of applicability of the analytical results. In Section 2.5, we take the polymerization kinetics of the filaments into account and show that there is an optimal angle at which the polymerization velocity is maximum.

## 2.2 Entropic forces and probability densities

According to the *wormlike chain model* (Kratky and Porod, 1949; Saito *et al.*, 1967), the elastic energy of a given configuration  $\mathbf{r}(s)$ , parametrized in terms of the arc length  $s \in [0, L]$ , is given by

$$\beta H = \frac{\ell_p}{2} \int_0^L ds \left( \frac{\partial \mathbf{t}(s)}{\partial s} \right)^2. \quad (2.1)$$

Here  $\mathbf{t}(s) = \partial \mathbf{r}(s)/\partial s \equiv \dot{\mathbf{r}}(s)$  is the local tangent to the contour  $\mathbf{r}(s)$ ,  $\ell_p = \kappa/k_B T$  is the persistence length with  $\kappa$  the polymer's bending modulus, and  $\beta = 1/k_B T$ . As the polymer is considered to be inextensible, we have  $|\mathbf{t}(s)| = 1$  for all  $s$ , i.e. the tangent vectors are restricted to the unit sphere.

In a cellular environment, biopolymers are flexed by Brownian motion, i.e. they exhibit thermal fluctuations in their shape. This makes for a rich mechanic response genuinely different from its classical analogue, a rigid beam. Consider a polymer whose position (not its orientation) is fixed at one end and one is pulling on its other end, a typical situation encountered in an experiment using optical or magnetic tweezers. Then there is no unique force-distance relation. It actually matters whether one pulls at constant force  $f$  and measures the resulting average distance  $\langle r \rangle(f)$  or vice versa. Results for the constant force ensemble are thoroughly discussed in Refs. Fixman and Kovac (1973); Kovac and Crabb (1982); Marko and Siggia (1995). In a constant distance ensemble, the probability density distribution of the end-to-end distance  $P(r)$  provides the necessary information (Wilhelm and Frey, 1996). It defines a free energy  $F(r) = -k_B T \ln P(r)$  from which the average force may be derived by differentiation,  $\langle f \rangle(r) = -\partial F(r)/\partial r$  (Frey *et al.*, 1998). Here, we are interested in the force a fluctuating filament exerts on a rigid obstacle which is fixed in its position. The polymer's end facing the obstacle is considered as free to fluctuate and only its proximal end is fixed in position and orientation; see Fig. 5.1. Since there are no direct forces between polymer and obstacle the force exerted on the wall is solely due to the steric constraints imposed on the filament. This suggests to use the term “entropic forces”, frequently used in analogous physical situations (Lubensky, 1997). However, this should not leave the reader with the wrong impression that there are different physical origins for entropic forces and those discussed in the preceding paragraph. It is merely the type of “boundary condition” imposed on the thermal fluctuations which leads to their (drastically) different character.

For getting acquainted with the problem, let us consider the simplest case, a grafted polymer whose one end and tangent is fixed such that it

is oriented perpendicular to a smooth wall (Fig. 5.1 with  $\vartheta = 0$ ). The presence of the wall allows only for those polymer configurations which are entirely in the half-space to the left of the wall. Since we are mostly interested in stiff polymers (which have a low probability for back-turns), this restriction may be approximated as a constraint solely on the position of the polymer tip facing the wall,  $r_z(L) \leq \zeta$ ; later in Section 2.4.3 we will show some simulation data going beyond this approximation.

To derive the average force acting on the wall, we consider a wall potential  $U(\zeta - r_z(L))$  for the free polymer tip, which at the end of the calculation will be reduced to a hard wall potential. For now, picture a steep potential which rises rapidly for  $r_z(L) \rightarrow \zeta$ . Then, the ensemble average for the force the polymer tip exerts perpendicular to the wall reads

$$\langle f_{\parallel} \rangle(\zeta) = \frac{1}{\mathcal{Z}_{\parallel}(\zeta)} \int \mathcal{D}[\mathbf{r}(s)] e^{-\beta(H+U)} \frac{\partial U}{\partial r_z(L)}. \quad (2.2)$$

Here the partition sum

$$\mathcal{Z}_{\parallel}(\zeta) = \int \mathcal{D}[\mathbf{r}(s)] e^{-\beta(H+U)} \quad (2.3)$$

is a path integral over all polymer configurations compatible with the boundary conditions imposed on the distal and free end of the grafted polymer, where the measure is taken such that the partition sum without a constraining wall ( $U = 0$ ) is normalized to 1. This is now a thermodynamic force. In an actual experiment, it is obtained by a time average with an averaging time much larger than the equilibration time for the grafted polymer. This force would also be measured in an experiment where a large number of independent and identical polymers push against the same wall.

Since the wall potential depends only on the difference between the position of the polymer tip and the wall, we may rewrite the entropic force in Eq. (2.2) as

$$\langle f_{\parallel} \rangle(\zeta) = k_B T \frac{\partial}{\partial \zeta} \ln \mathcal{Z}_{\parallel}(\zeta). \quad (2.4)$$

Upon defining a free energy of the confined polymer as

$$\mathcal{F}_{\parallel}(\zeta) = -k_B T \ln \mathcal{Z}_{\parallel}(\zeta), \quad (2.5)$$

the entropic forces again reads as a spatial derivative of a free energy

$$\langle f_{\parallel} \rangle(\zeta) = -\frac{\partial}{\partial \zeta} \mathcal{F}_{\parallel}(\zeta). \quad (2.6)$$

The physical interpretation of this free energy becomes clear as one goes to the hard wall limit. Then the partition function reduces to

$$\begin{aligned}\mathcal{Z}_{\parallel}(\zeta) &= \int \mathcal{D}[\mathbf{r}(s)] \Theta(\zeta - r_z(L)) e^{-\beta H} \\ &=: \langle \Theta(\zeta - r_z(L)) \rangle_0 ,\end{aligned}\quad (2.7)$$

where the subscript 0 indicates that the average is now taken with respect to the bending Hamiltonian only. The  $\Theta$ -function, defined such that  $\Theta(x) = 1$  for  $x > 0$  and zero elsewhere, indicates that only those configurations are counted with the position of the polymer tip to the left of the wall. Hence, as for the fixed distance ensemble in a pulling experiment, the free energy results from a quantity measuring the number of configurations obeying the imposed constraint, where each configuration is weighted by a Boltzmann factor for the bending energy.

It is useful to rewrite the partition function as

$$\mathcal{Z}_{\parallel}(\zeta) = \int_{-L}^L dz \Theta(\zeta - z) \langle \delta(z - r_z(L)) \rangle_0 = \int_{-L}^{\zeta} dz P_{\parallel}(z) , \quad (2.8)$$

where  $P_{\parallel}(z) = \langle \delta(z - r_z(L)) \rangle_0$  is the probability density to find the  $z$ -coordinate of the polymer's free end at  $z$  irrespective of its transverse coordinates. It identifies the restricted partition sum as the cumulative distribution function corresponding to the probability density  $P_{\parallel}(z)$ . One may then write the entropic force in the alternative form

$$\langle f_{\parallel} \rangle(\zeta) = k_{\text{B}} T \frac{P_{\parallel}(\zeta)}{\mathcal{Z}_{\parallel}(\zeta)} . \quad (2.9)$$

Upon multiplying this formula by  $d\zeta$ , it may be interpreted as follows. The work done on the wall upon displacing it by an infinitesimal distance  $d\zeta$  equals the thermal energy scale  $k_{\text{B}}T$  times a conditional probability  $P_{\text{left}}(\zeta)d\zeta = P_{\parallel}(\zeta)d\zeta/\mathcal{Z}_{\parallel}(\zeta)$ , which measures the probability that the position of the polymer tip is within a distance  $d\zeta$  from the wall given that the polymer is in the left half-space.

Since the probability density for the position of the polymer tip  $P(\mathbf{x}, z)$  is actually a function of the position perpendicular and transverse to the wall, Eq. (2.9) immediately suggests that one could define a *local* entropic

pressure. Indeed, upon generalizing the above arguments, one may write

$$\begin{aligned}
 p(\mathbf{x}, \zeta) &= \frac{-1}{\mathcal{Z}_{\parallel}(\zeta)} \int \mathcal{D}[\mathbf{r}] \frac{\partial U}{\partial \zeta} \delta(\mathbf{x} - \mathbf{r}_{\perp}(L)) e^{-\beta(H+U)} \\
 &= \frac{k_{\text{B}}T}{\mathcal{Z}_{\parallel}(\zeta)} \frac{\partial}{\partial \zeta} \langle \Theta(\zeta - r_z(L)) \delta(\mathbf{x} - \mathbf{r}_{\perp}(L)) \rangle_0 \\
 &= k_{\text{B}}T \frac{P(\mathbf{x}, \zeta)}{\mathcal{Z}_{\parallel}(\zeta)} \tag{2.10}
 \end{aligned}$$

for the entropic pressure, i.e. the force per unit area exerted locally at  $\mathbf{x}$  on the wall. Again, the entropic force is given by the thermal energy scale times a conditional probability density, which now measures the probability of finding the polymer tip at a particular site  $\mathbf{x}$  on the wall conditioned on the polymer configuration being to the left of the wall. Pictorially, one may say that the local pressure is given by  $k_{\text{B}}T$  times the number of “collisions” of the polymer with the wall per unit area, a reasoning which is frequently used in scaling analyses.

The total force is obtained by integrating over this local pressure,  $\langle f_{\parallel} \rangle(\zeta) = \int d\mathbf{x} p(\mathbf{x}, \zeta)$ . In addition, one may now also define an entropic torque as has recently been done for a rigid rod facing a planar wall (Roth *et al.*, 2002); we leave this issue for future investigations.

Generalizing the above ideas suggests to introduce an effective local free energy per unit area as

$$\mathcal{F}(\mathbf{x}, \zeta) = -k_{\text{B}}T \int^{\zeta} dz \frac{P(\mathbf{x}, z)}{\mathcal{Z}_{\parallel}(z)}, \tag{2.11}$$

which is useful in applications where the obstacle is actually not rigid but soft with some internal elasticity, e.g. a membrane whose dynamics is much slower than the equilibration time of the polymer. Then the elastic energy describing membrane bending and the above effective free energy may just be added to describe the combined system. Of course, such a description fails if time scales for the dynamics of both soft objects are comparable.

Our main conclusion in this section is that entropic forces generated by a grafted stiff polymer can be reduced to the calculation of the probability distribution of the polymer tip. For a polymer constrained to two dimensions, the distribution function has been found to show quite interesting behavior such as bimodality in the transverse displacement of the free end (Lattanzi *et al.*, 2004). This pronounced feature of the distribution function has recently been rationalized upon exploiting an interesting analogy to a random walker in shear flow (Benetatos *et al.*, 2005).

## 2.3 Polymer orthogonal to a wall

In this section, we are going to calculate the entropic force generated by a grafted polymer whose orientation is on average perpendicular to the wall. It illustrates the basic idea of our analytical calculations for the simplest geometry.

### 2.3.1 Weakly bending limit: mode analysis

In evaluating the distribution function analytically, we restrict ourselves to the limit of a *weakly bending filament*. In other words, we consider the persistence length  $\ell_p$  to be large enough compared to the total contour length  $L$ , such that the statistical weight of configurations with small sharp bends will be negligible. The key small dimensionless quantity will be the *stiffness parameter*

$$\varepsilon = L/\ell_p \quad (2.12)$$

and we will refer to the weakly bending limit also as the *stiff limit*.

For small  $\varepsilon$ , the transverse components  $t_x(s)$  and  $t_y(s)$  of the tangent vector  $\mathbf{t}(s)$  will be small for all  $s$ . The condition  $|\mathbf{t}(s)| = 1$  would suggest a parameterization of  $\mathbf{t}(s)$  in terms of polar coordinates or Euler angles. Such a parameterization, however, becomes quite cumbersome in the present case where the embedding into an external space matters due to the steric constraints imposed by the wall. It is much more convenient to use a Monge-like parameterization

$$\mathbf{t} = \frac{1}{\sqrt{1 + a_x^2 + a_y^2}} \begin{pmatrix} a_x \\ a_y \\ 1 \end{pmatrix}, \quad (2.13)$$

where we dropped all arguments  $s$  for brevity; the generalization to  $d$  spatial dimensions is obvious.

The boundary conditions at the ends of the polymer are

$$\mathbf{t}(0) = (0, 0, 1)^T \quad (\text{clamped end}), \quad (2.14a)$$

$$\dot{\mathbf{t}}(L) = (0, 0, 0)^T \quad (\text{free end}). \quad (2.14b)$$

This translates into  $\mathbf{a}(0) = (a_x(0), a_y(0))^T = (0, 0)^T$  and  $\dot{\mathbf{a}}(L) = (\dot{a}_x(L), \dot{a}_y(L))^T = (0, 0)^T$ . We thus can choose a Fourier representation or in other words a *normal mode decomposition*

$$a_x(s) = \sum_{k=1}^{\infty} a_{x,k} \sin\left(\lambda_k \frac{s}{L}\right) \quad (2.15)$$

with eigenvalues

$$\lambda_k = \frac{\pi}{2}(2k-1), \quad (2.16)$$

and Fourier (normal mode) amplitudes

$$a_{x,k} = \frac{2}{L} \int_0^L ds a_x(s) \sin\left(\lambda_k \frac{s}{L}\right), \quad (2.17)$$

and similar for  $a_y(s)$ . To second order in the Fourier amplitudes, the location of the end-point along the  $z$ -axis reads

$$\begin{aligned} r_z(L) &= \int_0^L ds t_z(s) \approx L - \frac{1}{2} \int_0^L ds [a_x^2(s) + a_y^2(s)] \\ &= L - \frac{L}{4} \sum_{k=1}^{\infty} [a_{x,k}^2 + a_{y,k}^2]. \end{aligned} \quad (2.18)$$

Similarly, we find for the Hamiltonian to second order

$$\beta H \approx \frac{\ell_p}{4L} \sum_{k=1}^{\infty} \lambda_k^2 [a_{x,k}^2 + a_{y,k}^2]. \quad (2.19)$$

### 2.3.2 Moment generating function

To calculate the probability density function  $P_{\parallel}(z)$ , we follow a procedure outlined in Wilhelm and Frey (1996) and consider the moment generating function

$$\begin{aligned} \mathcal{P}_{\parallel}(f) &:= \langle e^{-f(L-r_z(L))} \rangle_0 = \int_{-L}^L dz e^{-f(L-z)} P_{\parallel}(z) \\ &= \int_0^{2L} d\rho e^{-f\rho} P_{\parallel}(L-\rho). \end{aligned} \quad (2.20)$$

Note that thermal averages have to be evaluated using the bare elastic free energy Eq. (2.1). Since for stiff chains configurations with large values for the stored length (“compression”)  $\rho = L - z$  are rather unlikely, we can extend the upper boundary of the integral in the last line of the preceding equation to infinity. This allows us to write the moment generating function as the Laplace transform of the distribution function  $P_{\parallel}(z)$

$$\mathcal{P}_{\parallel}(f) = \int_0^{\infty} d\rho e^{-f\rho} P_{\parallel}(L-\rho). \quad (2.21)$$

For  $f = 0$ , the latter equation reduces to the normalization condition of the probability density function  $P_{\parallel}(z)$  such that  $\mathcal{P}_{\parallel}(0) = 1$ .

Combining Eqs. (2.18, 2.19) and 2.20, the moment generating function can be put into the following path integral form

$$\mathcal{P}_{\parallel}(f) = \int \mathcal{D}[\mathbf{a}(s)] \exp \left\{ -\frac{1}{2} \int_0^L ds [\ell_p \dot{\mathbf{a}}^2 + f \mathbf{a}^2] \right\} \quad (2.22)$$

with the boundary conditions given by Eq. (2.14). This path integral is easily evaluated upon using the Fourier representation of the transverse tangent fields Eq. (2.15), and noting that to harmonic order fluctuations in all transverse directions are statistically independent. We find in  $d$  spatial dimensions

$$\begin{aligned} \mathcal{P}_{\parallel}(f) &= \left( \int \prod_{k=1}^{\infty} \frac{da_k}{\mathcal{N}} \exp \left\{ -\frac{1}{4} \left[ \frac{\lambda_k^2 \ell_p}{L} + fL \right] a_k^2 \right\} \right)^{(d-1)} \\ &= \prod_{k=1}^{\infty} \left( 1 + \frac{fL^2}{\ell_p \lambda_k^2} \right)^{-(d-1)/2}, \end{aligned} \quad (2.23)$$

where the normalization factor  $\mathcal{N}$  of the path integral was chosen such that  $\mathcal{P}_{\parallel}(0) = 1$ . If  $f \in \mathbb{R}_+$  the product may be rewritten as (Hansen, 1975)

$$\mathcal{P}_{\parallel}(f) = \left( \cosh \sqrt{\frac{fL^2}{\ell_p}} \right)^{-\frac{1}{2}(d-1)}. \quad (2.24)$$

Note that the moment generating function, which also depends on the length scales  $L$  and  $\ell_p$ , has the scaling form

$$\mathcal{P}_{\parallel}(f, L, \ell_p) = \tilde{\mathcal{P}}_{\parallel}(fL_{\parallel}), \quad (2.25)$$

where we have defined the characteristic *longitudinal length scale*

$$L_{\parallel} := \frac{L^2}{\ell_p}. \quad (2.26)$$

The formulas in Eq. (2.23) and Eq. (2.24) are the basis for all subsequent calculations in this section, which are basically different forms of performing the inverse Laplace transform.

For future reference and comparison with the entropic forces, we close this subsection with a discussion of the force-extension relation in the fixed

force ensemble. It simply follows as the first moment of the moment generating function

$$\begin{aligned}\langle r_z(L) \rangle_f &= L + \frac{\partial \ln \mathcal{P}_{\parallel}(f)}{\partial f} \\ &= L \left( 1 - \frac{L(d-1)}{4\ell_p} \frac{\tanh \sqrt{fL_{\parallel}}}{\sqrt{fL_{\parallel}}} \right),\end{aligned}\quad (2.27)$$

where  $f$  is the external force in units of the thermal energy  $k_B T$ . In the limit of small external forces, this reduces to

$$\langle r_z(L) \rangle_f = L \left[ 1 - \frac{d-1}{4} \frac{L}{\ell_p} + \frac{d-1}{12} \left( \frac{L}{\ell_p} \right)^2 fL \right], \quad (2.28)$$

which identifies  $L_{\parallel}$  as  $4/(d-1)$  times the equilibrium stored length due to thermal fluctuations. We also recover the effective linear spring coefficient  $k_{\parallel} = 12\kappa^2/(d-1)k_B T L^4$ , which was previously calculated by Kroy and Frey (1996). For strong stretching forces the extension saturates asymptotically as

$$\langle r_z(L) \rangle_f = L \left[ 1 - \frac{L(d-1)}{4\ell_p \sqrt{fL_{\parallel}}} \right]. \quad (2.29)$$

In the limit of large compressional forces, the weakly bending rod approximation breaks down and one has to use different approaches to evaluate the force-extension relation (Frey *et al.*, 1998).

### 2.3.3 Probability density for the position of the polymer tip: analytical and MC results in 3d

We now return to the distribution function and the resulting entropic forces. Upon performing the inverse Laplace transform one gets (for details of the calculations see Appendix C.1.1)

$$P_{\parallel}(z) = \frac{2}{L_{\parallel}} \sum_{k=1}^{\infty} (-1)^{k+1} \lambda_k \exp \left[ -\lambda_k^2 \frac{L-z}{L_{\parallel}} \right]. \quad (2.30)$$

Inspection of Eq. (2.30) immediately tells us that it can be written in scaling form

$$P_{\parallel}(z, L, \ell_p) = L_{\parallel}^{-1} \tilde{P}_{\parallel}(\tilde{\rho}), \quad (2.31)$$

where we have made the dependence of the probability density on  $L$  and  $\ell_p$  explicit and introduced the scaling variable

$$\tilde{\rho} = \frac{L - z}{L_{\parallel}} \quad (2.32)$$

measuring the compression of the filament in units of  $L_{\parallel}$ . This implies that data for the probability density of the polymer tip can be rescaled to fall on a *scaling function*  $\tilde{P}_{\parallel}(\tilde{\rho})$ , shown as the solid curve in Fig. 2.2. Of course, since the analytical calculations are based on the mode analysis in the weakly bending limit, such a universal scaling curve is obtained only for small enough stiffness parameters  $\varepsilon$ .

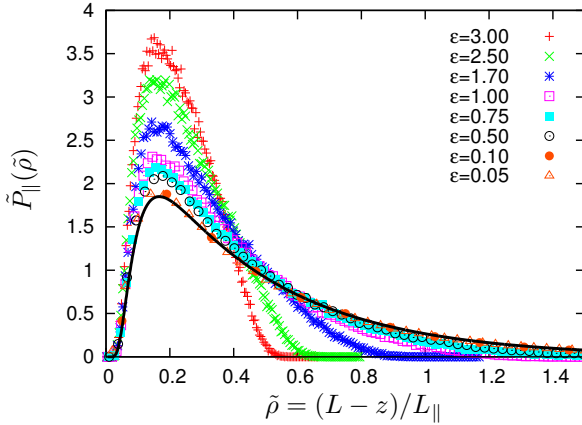


**Figure 2.2** Scaling function  $\tilde{P}_{\parallel}(\tilde{\rho})$  (solid line) in 3d for the probability density to find the free end of a grafted semiflexible polymer in a plane defined by  $r_z(L) = z$  or equivalently with a reduced stored length  $\tilde{\rho}$ . For comparison, MC data are given for a series of stiffness parameters  $\varepsilon = L/\ell_p$  indicated in the graph. Deviations from the scaling curve in the stiff limit become significant for  $\varepsilon \geq 0.5$ .

The probability density is strongly peaked towards full stretching,  $\tilde{\rho} \rightarrow 0$ , and falls off exponentially for large  $\tilde{\rho}$ , such that for  $\tilde{\rho} \geq 0.3$

$$\tilde{P}_{\parallel}^>(\tilde{\rho}) = \pi \exp\left(-\frac{1}{4}\pi^2\tilde{\rho}\right) \quad (2.33)$$

is already an excellent approximation. The series expansion given by Eq. (2.30) converges well for all values of  $z$  well below  $L$ , but its convergence properties become increasingly worse if  $z$  approaches  $L$ . As detailed

in Appendix C.1.2, one may also derive an alternative series representation of the tip distribution function which converges well close to full stretching

$$\tilde{P}_{\parallel}(\tilde{\rho}) = \sum_{l=0}^{\infty} (-1)^l \frac{2l+1}{\sqrt{\pi\tilde{\rho}^3}} \exp\left[-\frac{(l+\frac{1}{2})^2}{\tilde{\rho}}\right]. \quad (2.34)$$

Already the first term of Eq. (2.34)

$$\tilde{P}_{\parallel}^{<}(\tilde{\rho}) = \frac{1}{\sqrt{\pi\tilde{\rho}^3}} \exp\left(-\frac{1}{4\tilde{\rho}}\right) \quad (2.35)$$

gives an excellent fit for  $\tilde{\rho} \leq 0.3$ . In particular, it captures the main feature of the distribution function, namely its maximum is close to full stretching. The same approximate expression may also be obtained by evaluating the inverse Laplace transform using the method of steepest descent; see Appendix C.2. The asymptotic results given in Eq. (2.35) and Eq. (2.33) taken together give a representation of the scaling curve to a very high numerical accuracy. They are the analogues of the results found by Wilhelm and Frey (1996) for a freely fluctuating filament; see also Frey *et al.* (1998).

The MC data shown in Fig. 2.2 have been obtained by using a standard algorithm for a discretized wormlike chain, similar to the one described by Wilhelm and Frey (1996). As expected, the MC results agree very well with the analytical calculations for small values of  $\varepsilon$ . From Fig. 2.2 we can read off that the asymptotic stiff scaling regime remains valid up to stiffness parameters  $\varepsilon \approx 0.1$ ; even for  $\varepsilon = 0.5$  the shape of the scaling function resembles the MC data quite closely. As the polymer becomes more flexible, the shape asymptotically becomes Gaussian; for  $\varepsilon = 3$  a skew is still noticeable. Note that in the parameter range given in Fig. 2.2, the width of the rescaled probability densities stays approximately the same and is hence well characterized by the longitudinal scale  $L_{\parallel}$ .

### 2.3.4 Confinement free energy and entropic forces: 3d

Now we are in a position to calculate the restricted partition sum (cumulative probability distribution)  $\mathcal{Z}_{\parallel}(\zeta) = \int_{-L}^{\zeta} dz P_{\parallel}(z)$  by (formally) integrat-

ing the series expansion of Eq. (2.30) term by term. This gives

$$\begin{aligned}
 \mathcal{Z}_{\parallel}(\zeta) &= 1 - \int_{\zeta}^L dz P_{\parallel}(z) \\
 &= 1 - 2 \sum_{k=1}^{\infty} (-1)^{k+1} \lambda_k^{-1} \left( 1 - e^{-\lambda_k^2(L-\zeta)/L_{\parallel}} \right) \\
 &= 2 \sum_{k=1}^{\infty} (-1)^{k+1} \lambda_k^{-1} e^{-\lambda_k^2(L-\zeta)/L_{\parallel}}, \tag{2.36}
 \end{aligned}$$

where in the first line we used the normalization of  $P_{\parallel}(z)$  and in the last line the identity (Abramowitz and Stegun, 1970)

$$\sum_{k=1}^{\infty} (-1)^{k+1} \frac{1}{2k-1} = \frac{\pi}{4}. \tag{2.37}$$

The series expansion in Eq. (2.36) converges well for all values of  $\zeta$  well below  $L$ . Alternatively, one may start from Eq. (2.34) and derive

$$\mathcal{Z}_{\parallel}(\zeta) = 1 + 2 \sum_{k=1}^{\infty} (-1)^k \operatorname{erfc} \left( \frac{\lambda_k/\pi}{\sqrt{(L-\zeta)/L_{\parallel}}} \right), \tag{2.38}$$

which is well behaved for  $\zeta$  close to  $L$ , and dominated by its first term. A second method to obtain Eq. (2.38) can be found in Appendix C.3.

From both series expansions, it is evident that the restricted partition sum has the scaling property

$$\mathcal{Z}_{\parallel}(\zeta, L, \ell_p) = \tilde{\mathcal{Z}}_{\parallel}(\tilde{\eta}), \tag{2.39}$$

where we have introduced the scaling variable

$$\tilde{\eta} = \frac{L-\zeta}{L_{\parallel}}, \tag{2.40}$$

which measures the minimal stored length (compression)  $\eta = L-\zeta$  of the filament in units of  $L_{\parallel}$ . The confinement free energy,  $\tilde{\mathcal{F}}_{\parallel}(\tilde{\eta}) = -k_B T \ln \tilde{\mathcal{Z}}_{\parallel}(\tilde{\eta})$ , corresponding to this partition function is shown in Fig. 2.3. Again, the universal scaling function describes the MC data well for  $\varepsilon \leq 0.1$ . Note that for all values of  $\tilde{\eta}$  and the stiffness parameter  $\varepsilon$ , the free energy is convex. This will turn out to be an important feature which distinguishes the 3d and 2d case.

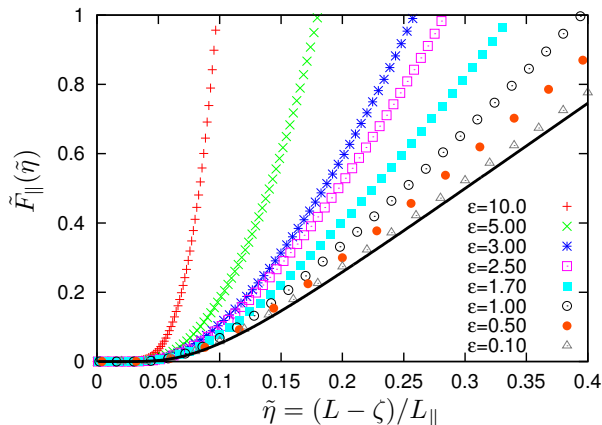


**Figure 2.3** Confinement free energy  $\tilde{\mathcal{F}}_{\parallel}(\tilde{\eta})$  of a grafted polymer constrained by a rigid wall in 3d as a function of the reduced minimal stored length  $\tilde{\eta} = (L - \zeta)/L_{\parallel}$ . The solid line gives the scaling function obtained in the limit of a weakly bending rod. Symbols represent MC data for different values of the stiffness parameter  $\epsilon$  as indicated in the graph.

Upon using Eq. (2.9) for the entropic force we find

$$f_{\parallel}(\zeta) = \frac{k_{\text{B}}T}{L_{\parallel}} \frac{\tilde{P}_{\parallel}(\tilde{\eta})}{\tilde{Z}_{\parallel}(\tilde{\eta})} \quad (2.41)$$

which immediately shows its scaling behavior and identifies  $k_{\text{B}}T/L_{\parallel}$  as the characteristic force scale. It is up to a prefactor identical to the critical force

$$f_c = \frac{\pi^2 \kappa}{4L^2} = \frac{\pi^2}{4} \frac{k_{\text{B}}T}{L_{\parallel}} \quad (2.42)$$

for the buckling instability of a classical Euler-Bernoulli beam (see Appendix. B). It suggest to rewrite the entropic force as

$$f_{\parallel}(\zeta, L, \ell_{\text{p}}) = f_c \tilde{f}_{\parallel}(\tilde{\eta}), \quad (2.43)$$

with the scaling function

$$\tilde{f}_{\parallel}(\tilde{\eta}) := \frac{4}{\pi^2} \frac{\tilde{P}_{\parallel}(\tilde{\eta})}{\tilde{Z}_{\parallel}(\tilde{\eta})}. \quad (2.44)$$

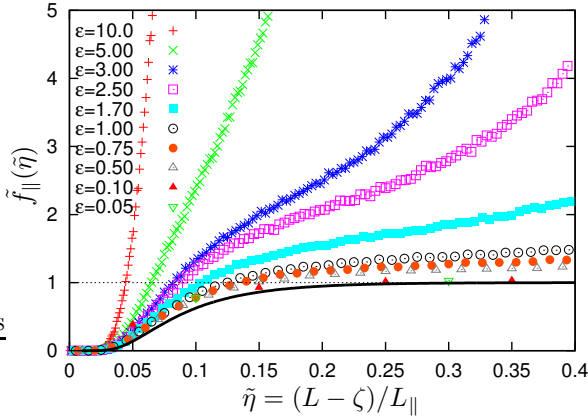


**Figure 2.4** Scaling function  $\tilde{f}_{\parallel}(\tilde{\eta})$  for the entropic force exerted on a wall at a distance  $\zeta$  from the grafted end as a function of the scaling variable  $\tilde{\eta} = (L - \zeta)/L_{\parallel}$ . Symbols represent MC data for different stiffness parameters  $\varepsilon$ , as indicated in the graph. Entropic force is a monotonically increasing function of  $\tilde{\eta}$ .

The analytical result for the scaling function  $\tilde{f}_{\parallel}(\tilde{\eta})$ , shown as the solid curve in Fig. 2.4, has several characteristic features. First of all, it is always monotonically increasing since the free energy is convex. For  $\tilde{\eta} \gtrsim 0.4$ , the scaling function is  $\tilde{f}_{\parallel} \approx 1$  corresponding to  $f_{\parallel} \approx f_c$ , i.e. a vanishing contribution of thermal fluctuations to the force. For smaller  $\tilde{\eta}$ , corresponding to larger distances  $\zeta$  between the wall and the grafted end of the polymer, fluctuations reduce the force exerted on the wall by effectively shortening the polymer. For  $\zeta \rightarrow L$  (resp.  $\tilde{\eta} = 0$ ), the probability of the polymer to contact the wall becomes smaller and smaller until finally for  $\zeta = L$  only one configuration, namely the completely straight one, has  $r_z(L) = L$ . Hence the force must vanish for all  $\zeta \geq L$  (resp.  $\tilde{\eta} \leq 0$ ).

We have learned already in Section 2.3.3 that there are excellent approximations to the scaling function for the probability density of the free polymer end for small values of the reduced stored length, Eq. (2.35). In the same way, the first term of Eq. (2.38) is an excellent approximation to the infinite series for  $\tilde{\eta} \lesssim 0.2$ . Thus, we may write for the scaling function of the entropic force

$$\tilde{f}_{\parallel}^{<}(\tilde{\eta}) = \frac{4 e^{-1/4\tilde{\eta}}}{\pi^{5/2} \tilde{\eta}^{3/2} (1 - 2 \operatorname{erfc}(1/2\sqrt{\tilde{\eta}}))}, \quad (2.45)$$

which already describes most of the nontrivial shape of the scaling function. For  $\tilde{\eta} \gtrsim 0.2$ , it suffices to high accuracy to use the first two terms of Eq. (2.36), which gives

$$\tilde{f}_{\parallel}^>(\tilde{\eta}) = \frac{1 - 3e^{-2\pi^2\tilde{\eta}}}{1 - \frac{1}{3}e^{-2\pi^2\tilde{\eta}}}. \quad (2.46)$$

Upon inspection of Eq. (2.41), one may interpret the functional form of the entropic force as due to two effects. In the numerator, we have the probability density for the position of the free end at the wall. This function shows a pronounced peak as one decreases the distance  $\zeta$  (resp. increases the scaling variable  $\tilde{\eta}$ ). At the same time, the denominator, the cumulative distribution function, decreases by decreasing  $\zeta$ . It is now a matter of how fast these changes occur and what the ensuing shape of the scaling function for the entropic force will be. In the present case of a polymer in 3d, the decrease in the cumulative distribution function seems to be fast enough to compensate the maximum in the probability density of the free polymer end such that the entropic force becomes a monotonically increasing function of  $\tilde{\eta}$ .

From Fig. 2.4, one observes that the universal scaling curve is a lower bound to the MC data for all values of the stiffness parameter  $\varepsilon$ . For fixed  $\varepsilon$ , the entropic force always increases monotonically with increasing compression; for intermediate values  $\varepsilon \approx 2.5$  there is a pronounced change in curvature at  $\tilde{\eta} \approx 0.25$ . For strong compression the results asymptote to the mechanical limit ( $k_{\text{B}}T = 0$ ). This limit is not correctly reproduced within the harmonic approximation which gives

$$f_{\text{mech}}(\zeta) = f_c \Theta(L - \zeta), \quad (2.47)$$

whereas the exact force-extension curve is a monotonous function in  $\zeta$  that is somewhat larger than  $f_c$  for  $\zeta < L$  and tends to  $f_c$  for  $\zeta \rightarrow L$ .

One might finally ask, whether these entropic forces  $f_{\parallel}(\zeta)$  are related to the force extension relation discussed in section 2.3.2,  $\langle r_z(L) \rangle_f - \langle r_z(L) \rangle_0 = k_{\parallel}^{-1}f + \mathcal{O}(f^2)$  with  $k_{\parallel} = 6\kappa^2/k_{\text{B}}TL^4$  (Kroy and Frey, 1996). Rewriting these linear response result in scaling form we find,

$$\frac{f}{f_c} = \frac{24}{\pi^2} \left( \tilde{\eta} - \frac{1}{2} \right). \quad (2.48)$$

Comparing this with Fig. 2.4, we see that the linear response result does not contain any information about the situation under investigation here. To the contrary, the initial rise of the force when  $\zeta$  becomes slightly smaller than  $L$  is highly nonlinear (see Eq. (2.45)).

### 2.3.5 Distribution function and entropic forces: 2d

Since in some important physiological situations like the leading edge of a crawling cell, polymer is essentially confined to fluctuate in 2d, it is important to look at the 2d problem more precisely. Analogous to the previous section, the tip distribution function of a polymer confined to 2d, e.g. by two parallel glass plates, obeys a scaling law in the stiff limit

$$P_{\parallel}(z, L, \ell_p) = L_{\parallel}^{-1} \tilde{P}_{\parallel}(\tilde{\rho}). \quad (2.49)$$

The scaling function may again be represented in terms of series expansions (see Appendix C.1.2). A series which converges well for small values of  $\tilde{\rho}$  reads

$$\tilde{P}_{\parallel}(\tilde{\rho}) = \sum_{l=0}^{\infty} \binom{-\frac{1}{2}}{l} \frac{2l + \frac{1}{2}}{\sqrt{2\pi} \tilde{\rho}^{3/2}} \exp\left[-\frac{(l + \frac{1}{4})^2}{\tilde{\rho}}\right]; \quad (2.50)$$

for an explicit formula for the binomial coefficient in Eq. (2.50) see Eq. (C.17). The scaling function, shown as the solid curve in Fig. 2.5, has an overall shape which is quite similar to 3d with a pronounced maximum close to full stretching. The series approximations may again give useful approximate

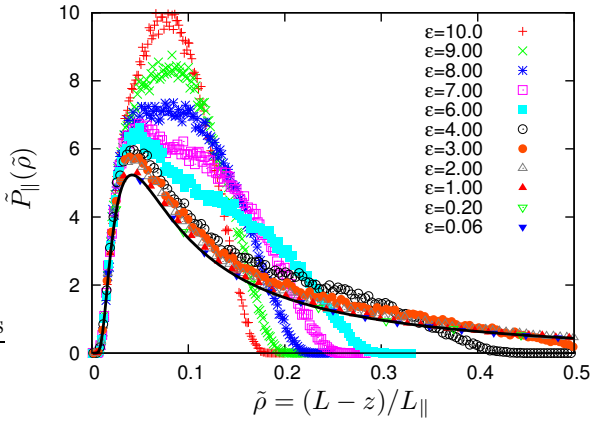


**Figure 2.5** Probability density  $\tilde{P}_{\parallel}(\tilde{\rho})$  of the free end of a grafted semiflexible polymer in 2d as a function of  $\tilde{\rho}$  (solid curve). Symbols represent MC data for different stiffness parameters, as indicated in the graph. MC data deviates from universal curve as  $\epsilon$  increases

expressions for the shape. In the proximity of full stretching, the series

given by Eq. (2.50) converges very fast such that already the first term

$$\tilde{P}_{\parallel}^{<}(\tilde{\rho}) = \frac{1}{\sqrt{8\pi\tilde{\rho}^{3/2}}} \exp\left(-\frac{1}{16\tilde{\rho}}\right) \quad (2.51)$$

is an excellent approximation for the whole series at least for  $\tilde{\rho} \leq 0.3$ . As in 3d, a saddle point approximation also gives Eq. (2.51) (see Appendix C.2). Alternatively, as shown in Appendix C.1.2, one may derive a series expansion which converges well in the strong compression limit; see Eq. (C.11). For  $\tilde{\rho} \gtrsim 0.3$ , it suffices to use the first term of this sum only which reads

$$\begin{aligned} \tilde{P}_{\parallel}^{>}(\tilde{\rho}) &= \frac{\pi e^{-\pi^2\tilde{\rho}/4}}{2\sqrt{2}} \left[ 1 + 1.5 e^{-5\pi^2\tilde{\rho}/16} + 2 e^{-12\pi^2\tilde{\rho}/16} \right. \\ &\quad \left. + 2.5 e^{-21\pi^2\tilde{\rho}/16} + 3 e^{-32\pi^2\tilde{\rho}/16} \right]. \end{aligned} \quad (2.52)$$

Upon increasing the stiffness parameter, the rescaled probability distribution deviates from the scaling function in the semiflexible limit and approaches a Gaussian distribution. In contrast to 3d, there is an intermediate parameter regime in the stiffness parameter where  $\tilde{P}_{\parallel}(\tilde{\rho})$  exhibits a marked shoulder. This feature of the distribution function has recently been identified and explained in terms of an interesting analogy with the physics of a random walker in shear flow (Benetatos *et al.*, 2005).

Upon integrating Eq. (2.50) from  $-L$  to  $\zeta$ , one obtains for the restricted partition sum

$$\mathcal{Z}_{\parallel}(\zeta) = 1 - \sqrt{2} \sum_{k=0}^{\infty} \frac{(-1)^k (2k-1)!!}{2^k k!} \operatorname{erfc}\left(\frac{\lambda_{2k+1}}{2\pi\sqrt{\tilde{\eta}}}\right), \quad (2.53)$$

with the same scaling variable  $\tilde{\eta}$  as in the previous section. Similarly, using Eq. (C.11) gives

$$\mathcal{Z}_{\parallel}(\zeta) \approx \frac{1}{1.49} \sum_{k=0}^{\infty} (-1)^k \sum_{i=4}^8 \lambda_{2k+i/4}^{-1} e^{-\lambda_{2k+i/4}^2 \tilde{\eta}}. \quad (2.54)$$

Hence, as in 3d, one finds for the free energy

$$\mathcal{F}_{\parallel}(\zeta, L, \ell_p) = -k_B T \ln \tilde{\mathcal{Z}}_{\parallel}(\tilde{\eta}) \quad (2.55)$$

and the entropic force

$$f_{\parallel}(\zeta, L, \ell_p) = f_c \tilde{f}_{\parallel}(\tilde{\eta}) \quad (2.56)$$

with the scaling function

$$\tilde{f}_{\parallel}(\tilde{\eta}) = -\frac{4}{\pi^2} \frac{\tilde{Z}'_{\parallel}(\tilde{\eta})}{\tilde{Z}_{\parallel}(\tilde{\eta})} \quad (2.57)$$

where  $f_c = \pi^2 \kappa / 4L^2$ ; see the solid curves in Fig. 2.6 and Fig. 2.7 for a plot of the scaling functions for the free energy and entropic force, respectively.

The key difference between the results in 2d and 3d is that the effective

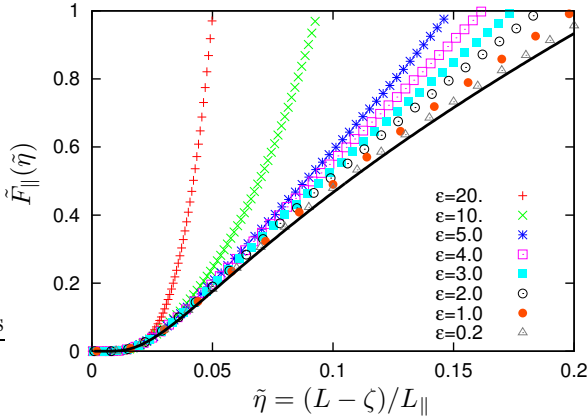


**Figure 2.6** Free energy of a grafted polymer whose tip is constrained by a rigid wall in 2d. The solid line gives the universal scaling function in the stiff limit. MC data are given by the symbols for different values of the stiffness parameter  $\varepsilon$  as indicated in the graph.

free energy exhibits a change in curvature at  $\tilde{\eta} \approx 0.05$  and as a result a pronounced peak in the entropic force. The peak is a pretty robust feature of the distribution function and vanishes only for very large values of  $\varepsilon \approx 5$ .

In order to understand the physical origin of this peak it suffices to consider small values of  $\tilde{\eta}$ . Then, using only the leading term of the series expansion Eq. (2.53), one obtains for the entropic force

$$\tilde{f}_{\parallel}^{<}(\tilde{\eta}) = \frac{\sqrt{2}e^{-1/16\tilde{\eta}}}{\pi^{5/2}\tilde{\eta}^{3/2} (1 - \sqrt{2}\operatorname{erfc}[1/4\sqrt{\tilde{\eta}}])}. \quad (2.58)$$

This has the same functional form as the corresponding expression in 3d, Eq. (2.45), but differs in some numerical factors. These differences can all be traced back to the strength  $\alpha$  of the essential singularity of the tip

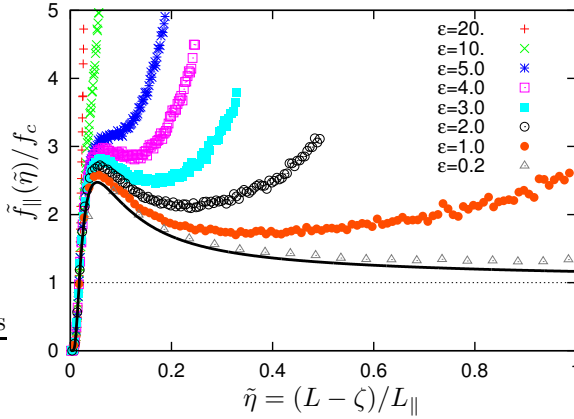


**Figure 2.7** Scaling function for the entropic force which a grafted polymer exerts on a rigid wall in 2d as a function of the reduced stored length  $\tilde{\eta} = (L - \zeta)/L_{\parallel}$ . The solid line gives the universal scaling function in the stiff limit. MC data are given by the symbols for different values of the stiffness parameter  $\epsilon$  as indicated in the graph. There is a pronounced peak in the entropic force for  $\epsilon < 5$ .

distribution function close to full stretching,  $\tilde{P}_{\parallel}(\tilde{\rho}) \propto \exp(-\alpha/\tilde{\rho})$ ; compare Eq. (2.35) with Eq. (2.51). One may interpret this strength as a kind of phase space factor counting how fast the number of polymer configurations decreases as one approaches full stretching. It clearly shows that the maximum of the entropic force in 2d is of purely geometric origin. As an interesting consequence of this maximum, one should note that for most values of the reduced stored length  $\tilde{\eta}$  the entropic force *exceeds* the purely mechanical force given by the Euler buckling force.

## 2.4 Grafted polymer at an oblique angle to the wall

The generic situation one encounters in a cellular system is that the polymer is inclined with respect to a membrane. Then we have to ask how the force derived above changes when the graft of the polymer is not orthogonal to the constraining wall but at some oblique angle  $\pi/2 - \vartheta$ ; see Fig. 2.8. Since the presence of the wall restricts the position of the polymer tip to

$$r_z(L) \cos \vartheta + r_x(L) \sin \vartheta \leq \zeta \quad (2.59)$$

one has to evaluate the restricted partition sum

$$\begin{aligned} \mathcal{Z}(\zeta, \vartheta) &= \langle \Theta[\zeta - r_z(L) \cos \vartheta - r_x(L) \sin \vartheta] \rangle_0 \\ &= \int dx dz P(x, z) \Theta[\zeta - z \cos \vartheta - x \sin \vartheta] \end{aligned} \quad (2.60)$$

to find the entropic force.

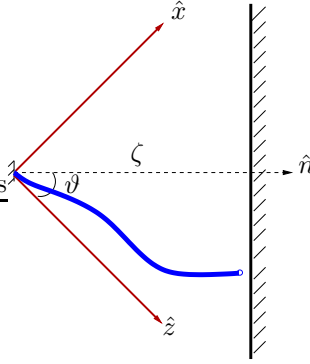


**Figure 2.8** A smooth hard wall at some oblique angle  $\pi/2 - \vartheta$ , constrains the configurations of a stiff polymer grafted parallel to the  $z$ -axis.

### 2.4.1 Probability distribution function of the tip

This calculation requires the knowledge of the joint probability density of the tip

$$P(x, z) := \langle \delta[r_x(L) - x] \delta[r_z(L) - z] \rangle_0. \quad (2.61)$$

In Section 2.3, we have already analyzed the reduced distribution function  $P_{\parallel}(z)$  and found that its width is characterized by the scale  $L_{\parallel} = L^2/\ell_p$ . Similarly, one can find an explicit expression for  $P_{\perp}(x)$  in harmonic approximation, where

$$r_x(L) \approx \sum_{k=1}^{\infty} a_{x,k} \int_0^L ds \sin(\lambda_k s/L) = L \sum_{k=1}^{\infty} \lambda_k^{-1} a_{x,k}, \quad (2.62)$$

and thus

$$\begin{aligned} P_{\perp}(x) &= \int \frac{dq}{2\pi} e^{iqx} \left\langle \exp \left[ -iqL \sum_{k=1}^{\infty} \lambda_k^{-1} a_{x,k} \right] \right\rangle \\ &= \int \frac{dq}{2\pi} e^{iqx} \exp \left[ -\frac{L^3}{\ell_p} q^2 \sum_{k=1}^{\infty} \lambda_k^{-4} \right]. \end{aligned} \quad (2.63)$$

With  $\sum_{k=1}^{\infty} (2k-1)^{-4} = \frac{\pi^4}{96}$  (Abramowitz and Stegun, 1970), this gives a Gaussian distribution

$$P_{\perp}(x) = \frac{1}{\sqrt{2\pi}L_{\perp}} e^{-\frac{1}{2}(x/L_{\perp})^2}, \quad (2.64)$$

where we have defined the characteristic *transverse length scale*

$$L_{\perp} = \sqrt{L^3/3\ell_p}. \quad (2.65)$$

Together with  $L_{\parallel}$ , these are the two length scales characterizing the width of the joint distribution function. This suggests to write the joint distribution function as

$$P(x, z, L, \ell_p) = \frac{1}{L_{\parallel}L_{\perp}} \tilde{P}(\tilde{x}, \tilde{\rho}), \quad (2.66)$$

in terms of dimensionless variables

$$\tilde{x} = x/L_{\perp}, \quad (2.67)$$

$$\tilde{\rho} = (L-z)/L_{\parallel}. \quad (2.68)$$

An explicit form of the joint distribution function can be calculated to harmonic order. For simplicity, we start with a polymer fluctuating only in the  $x$ - $z$ -plane ( $d=2$ ). Then

$$\begin{aligned} P_2(x, z) &= \int \frac{dq_z}{2\pi} \frac{dq_x}{2\pi} e^{-iq_z z - iq_x x} \langle e^{i(q_z r_z(L) + q_x r_x(L))} \rangle_0 \\ &= \int \frac{dq_z}{2\pi} \frac{dq_x}{2\pi} e^{iq_z(L-z) - iq_x x} \prod_k \left\langle e^{-i \left( \frac{Lq_z}{4} a_{x,k}^2 - \frac{Lq_x}{\lambda_k} a_{x,k} \right)} \right\rangle \\ &= \int \frac{dq_z}{2\pi} \frac{dq_x}{2\pi} e^{iq_z(L-z) - iq_x x} \prod_k \sqrt{\frac{\lambda_k^2}{\lambda_k^2 + iq_z L_{\parallel}}} e^{-\frac{3q_x^2 L_{\perp}^2}{\lambda_k^2 (\lambda_k^2 + iq_z L_{\parallel})}} \\ &= \frac{1}{L_{\perp} L_{\parallel}} \int \frac{d\tilde{q}_z}{2\pi} \frac{d\tilde{q}_x}{2\pi} e^{i\tilde{q}_z \tilde{\rho} - i\tilde{q}_x \tilde{x}} \prod_k \sqrt{\frac{1}{1 + i\tilde{q}_z \lambda_k^{-2}}} e^{\sum_k \frac{-3\tilde{q}_x^2}{\lambda_k^2 (\lambda_k^2 + i\tilde{q}_z)}} \\ &= \frac{1}{L_{\perp} L_{\parallel}} \int \frac{d\tilde{q}_z}{2\pi} \frac{d\tilde{q}_x}{2\pi} a_2(i\tilde{q}_z) e^{i\tilde{q}_z \tilde{\rho} - i\tilde{q}_x \tilde{x}} e^{-\frac{3}{2} \tilde{q}_x^2 b(i\tilde{q}_z)}, \end{aligned} \quad (2.69)$$

where for  $z \in \mathbb{R}_+$  we have (Abramowitz and Stegun, 1970)

$$a_2(z) := \prod_k \sqrt{\frac{1}{1 + z\lambda_k^{-2}}} = \sqrt{\frac{1}{\cosh \sqrt{z}}}, \quad (2.70)$$

$$b(z) := 2 \sum_k \frac{1}{\lambda_k^2(\lambda_k^2 + z)} = \frac{\sqrt{z} - \tanh \sqrt{z}}{z^{3/2}}. \quad (2.71)$$

For  $d = 3$ , the additional degrees of freedom associated with excursions in the  $y$ -direction lead to the replacement of  $q_z a_x^2(k)$  by  $q_z [a_x^2(k) + a_y^2(k)]$  which results in an additional factor of  $\sqrt{1 + iq_z \lambda_k^{-2}}$  for each mode  $k$ . Thus, for general  $d$ , we have to replace  $a_2(z)$  with

$$a_d(z) := \prod_k \left[ \frac{1}{1 + z\lambda_k^{-2}} \right]^{(d-1)/2}. \quad (2.72)$$

As  $\Re[b(i\tilde{q}_z)] > 0$  for all  $\tilde{q}_z \in [-\infty, \infty]$ , the Gaussian integration over  $\tilde{q}_x$  in Eq. (2.69) can be performed by completing the square, such that

$$\tilde{P}_d(\tilde{x}, \tilde{\rho}) = \int \frac{d\tilde{q}_z}{2\pi} e^{i\tilde{q}_z \tilde{\rho}} \frac{a_d(i\tilde{q}_z)}{\sqrt{6\pi b(i\tilde{q}_z)}} \exp \left[ -\frac{\tilde{x}^2}{6b(i\tilde{q}_z)} \right]. \quad (2.73)$$

Along similar lines, one may also calculate the full joint distribution function for a grafted polymer in  $d = 3$ ,

$$\begin{aligned} P_3(x, y, z) &= \frac{1}{L_\perp^2 L_\parallel} \int \frac{d\tilde{q}_z}{2\pi} e^{i\tilde{q}_z \tilde{\rho}} \frac{a_3(i\tilde{q}_z)}{6\pi b(i\tilde{q}_z)} \exp \left[ -\frac{\tilde{x}^2 + \tilde{y}^2}{6b(i\tilde{q}_z)} \right] \\ &=: \frac{1}{L_\perp^2 L_\parallel} \tilde{P}_3(\tilde{x}, \tilde{y}, \tilde{\rho}). \end{aligned} \quad (2.74)$$

In addition to the poles of  $a_3(i\tilde{q}_z)$  at  $\tilde{q}_z = i\lambda_k^2$  on the positive imaginary axis of the  $\tilde{q}_z$ -plane, the integrand also has singularities at the zeros  $i\lambda_k^2$  of  $b(z)$ . Thus we continue by evaluating the integrals numerically.

### Numerical evaluation of integrals

The integrand of Eq. (2.73) has no singularities on the real  $\tilde{q}_z$ -axis. Before attempting a numerical integration, we discuss the behavior of the different terms appearing in Eq. (2.73). For  $d = 3$ , we have

$$a_3(z) = \prod_k \frac{1}{1 + z\lambda_k^{-2}} = \frac{1}{\cosh \sqrt{z}}. \quad (2.75)$$

For  $\tilde{q}_z \in \mathbb{R}$ , the real and the imaginary part  $1/\cosh \sqrt{i\tilde{q}_z}$  are respectively even and odd functions rapidly decaying in magnitude for  $\tilde{q}_z \rightarrow \pm\infty$ . The real part of  $1/b(i\tilde{q}_z)$  is strictly positive and increasing with increasing  $|\tilde{q}_z|$ . The imaginary part of  $1/b(i\tilde{q}_z)$  behaves asymptotically as  $\Im [b^{-1}(i\tilde{q}_z)] \sim \tilde{q}_z$  leading to a second strongly oscillating contribution to the integrand of Eq. (2.73) besides  $\exp(iqz)$ . In the interest of numerical stability of the integration, it is advantageous to rewrite the integrand appearing in Eq. (2.73) to

$$\frac{1}{2\pi} e^{iq(\tilde{\rho} - \tilde{x}^2/6)} \frac{a_3(iq)}{\sqrt{2\pi 3b(iq)}} \exp \left[ -\frac{\tilde{x}^2}{6} (1/b(iq) - iq) \right] \quad (2.76)$$

for  $q$  larger than some fixed  $q_0$ .

### Region of vanishing probability

Eq. (2.76) suggests that  $\tilde{\rho} = \tilde{x}^2/6$  is a special situation. The probability density  $P(x, z)$  must vanish for points which are at distances greater than  $L$  from the graft:  $x^2 + z^2 \leq L^2$ . What does this translate to in the harmonic approximation? The largest value  $x^*$  of  $r_x(L)$  that can be obtained for a given value  $z^*$  of  $r_z(L)$  can be found from the variation of  $r_x(L) - \rho(z^* - r_z(L))$  where  $\rho$  is a Lagrange multiplier. Using Eq. (2.18) and Eq. (2.62), this leads to  $a_{x,k} = a/\lambda_k$  where  $a$  is some number. We thus find

$$x^* = La \sum_{k=1}^{\infty} \lambda_k^{-2} = L \frac{a}{2} \quad (2.77)$$

and

$$z^* = L - \frac{L}{4} a^2 \sum_{k=1}^{\infty} \lambda_k^{-2} = L - L \frac{a^2}{8} \quad (2.78)$$

resulting in

$$\frac{L - z^*}{L} = \frac{1}{2} \left( \frac{x^*}{L} \right)^2. \quad (2.79)$$

As  $L_{\perp}^2/LL_{\parallel} = 1/3$ , this is equivalent to

$$\tilde{\rho}^* = \frac{1}{6} (\tilde{x}^*)^2. \quad (2.80)$$

Hence  $\tilde{P}(\tilde{x}, \tilde{\rho})$  has to vanish for  $\tilde{\rho} < \tilde{x}^2/6$ .

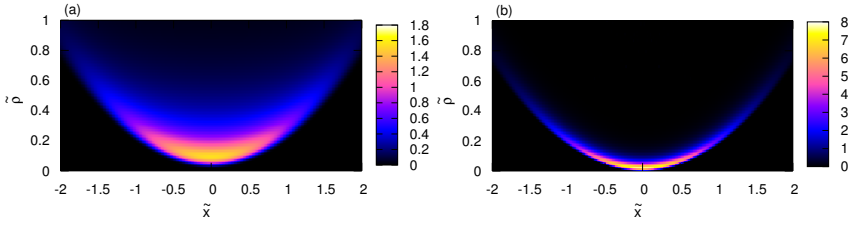


**Figure 2.9** Density plot of the probability density  $\tilde{P}(\tilde{x}, \tilde{\rho})$  in (a)  $d = 3$  and (b)  $d = 2$  calculated numerically from Eq. (2.73). As it is expected, the probability distribution of the tip is much narrower in  $2d$  compare to  $3d$ .

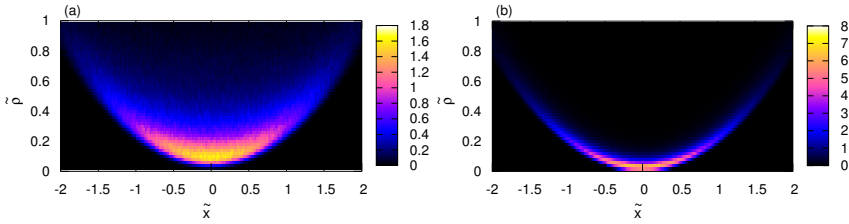


**Figure 2.10** Density plot of the probability density  $\tilde{P}(\tilde{x}, \tilde{\rho})$  in (a)  $d = 3$  and (b)  $d = 2$  obtained from MC simulations for  $\varepsilon = 0.1$ . The MC data agrees very well with corresponding numerical results in Fig. 2.9.

### Results for the general distribution function

It is now straightforward to evaluate the integrals in Eq. (2.73) by some standard numerical method. The corresponding results are shown in Fig. 2.9 as contour plots of  $\tilde{P}(\tilde{x}, \tilde{\rho})$  in  $d = 3$  and  $d = 2$ , respectively. These analytical results compare very well with MC results for polymers with a stiffness parameter  $\varepsilon \leq 0.2$ ; see a plot with  $\varepsilon = 0.1$  in Fig. 2.10. There are deviations between the harmonic approximation and MC data for larger values of  $\varepsilon$  (Lattanzi *et al.*, 2004; Benetatos *et al.*, 2005).

The density distribution essentially vanishes outside the parabola given by  $\tilde{\rho} = \tilde{x}^2/6$ , corresponding to the classical contour of the polymer in harmonic order. The main weight of  $\tilde{P}(\tilde{x}, \tilde{\rho})$  is concentrated close to this line, where the effect is stronger for  $d = 2$ . Profiles parallel to the  $\tilde{\rho}$  direction are of a shape qualitatively similar to  $\tilde{P}_{\parallel}(\tilde{\rho})$  (see Fig. 2.2) at least for small  $\tilde{x}$ . Profiles parallel to the  $\tilde{x}$ -axis are not Gaussian. For small  $\tilde{\rho} \lesssim 0.1$ , they are peaked at  $\tilde{x} = 0$  but unlike a Gaussian, they vanish for  $\tilde{x}^2 > 6\tilde{\rho}$ .

For larger  $\tilde{\rho}$ , they display a double-peaked shape. Both features would be completely missed by a factorization approximation  $\tilde{P}(\tilde{x}, \tilde{\rho}) = \tilde{P}_\perp(\tilde{x})\tilde{P}_\parallel(\tilde{\rho})$ .

The shape of the full joint probability distribution  $P_3(x, y, z)$  is best illustrated by plotting an iso-surface, e.g.  $\tilde{P}_3(\tilde{x}, \tilde{y}, \tilde{\rho}) = 0.1$  as shown in Fig. 2.11. Due to rotational symmetry, a density plot for  $P_3(x, y, z)$  may be obtained by rotating the contour plot of  $P_3(x, z)$  (Fig. 2.9a) around the  $z$ -axis. Again MC and analytical results are identical for small  $\varepsilon$ .

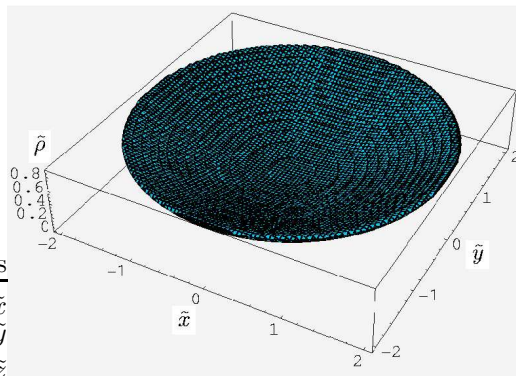


**Figure 2.11** 3d probability isosurface ( $\tilde{P}(\tilde{x}, \tilde{y}, \tilde{z}) \approx 0.1$ ) of a grafted polymer calculated numerically from Eq. (2.74).

Further insight can be gained by the inspection of the joint distribution function  $P(x, z)$ , represented with density plots in Fig. 2.12 and Fig. 2.13 in 3d and 2d, respectively. In the stiff limit,  $P(x, z)$  should be confined to the classical contour obtained by applying the elasticity equations to a rigid rod. This contour can be approximated by a parabola in the proximity of full stretching and is obtained through elliptic functions for any deformation (Landau and Lifshitz, 1959). In Fig. 2.12a the classical contour coincides with the ridge of the probability distribution function. As we relax the stiffness, thermal fluctuations will make the tip of the filament explore the configuration space in the vicinity of the classical contour. Roughly speaking, transverse bending fluctuations enhance fluctuations along the classical contour and shift weight from the center to the upper and lower wings in Figs. 2.12a and 2.12b. In contrast, longitudinal fluctuations widen the distribution function perpendicular to the classical contour. Since for a semiflexible polymer, the corresponding lengths  $L_\perp$  and  $L_\parallel$  scale differently transverse fluctuations are much “softer” than longitudinal ones, upon low-

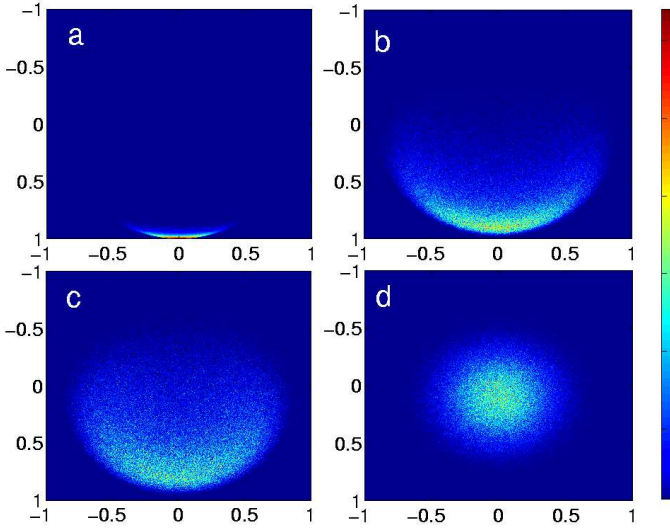


**Figure 2.12** Color density plots of  $P(x, z)$  obtained by Monte Carlo simulations in 3d: regions with high probability are colored in red. (a)  $\epsilon = 0.1$ ; (b)  $\epsilon = 1$ ; (c)  $\epsilon = 5$ ; (d)  $\epsilon = 10$ .

erling the stiffness  $P(x, z)$  gains more weight in the wings rather than in the center. It is precisely this effect that gives rise to the doublepeak distribution, when  $P(x, z)$  is projected in the transverse direction [see Fig. 2.12b]. Eventually, in the flexible limit, where transverse and longitudinal fluctuations become comparable,  $P(x, z)$  is spread so as to cover almost all the available space Fig. 2.12c, before the isotropic Gaussian distribution is recovered Fig. 2.12d.

Density plot of  $P(x, y)$  has been also presented in Fig. 2.14 for different values of  $\epsilon$  in 3d. At the intermediate values of  $\epsilon \sim 1$  (semiflexible polymer), a yellow ring (higher density) forms inside two red rings (lower density), which is the 3d manifestation of the corresponding double peak structure of  $P(y)$  in 2d (see Lattanzi *et al.* (2004)). In order to compare our MC data with analytical results obtained by Semeriyarov and Stepanov (2007),  $P(x = 0, y)$  has been presented in Fig. 2.15 for different values of  $\epsilon$ . Obviously, there is a nice agreement between our Monte Carlo simulations and analytical results. Both MC data and analytical results are normalized such that  $\int_{-L}^L P(x = 0, y) dy = 1$ . The transverse one dimensional

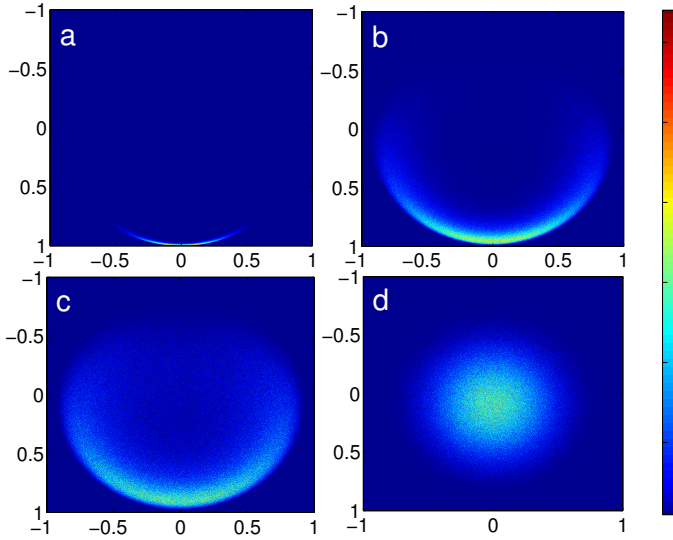


**Figure 2.13** Color density plots of  $P(x, z)$  obtained by Monte Carlo simulations in 2d: regions with high probability are colored in red. (a)  $\epsilon = 0.1$ ; (b)  $\epsilon = 1$ ; (c)  $\epsilon = 5$ ; (d)  $\epsilon = 10$  (Lattanzi *et al.*, 2004).

distribution function  $P(x = 0, y)$ , displays a bimodal shape in the intermediate range of  $\epsilon = 1.3, \dots, 3.5$  which is consistency with the analytical calculations by Semeriyarov and Stepanow (2007).

### 2.4.2 Entropic forces: scaling functions

We are now in a position to evaluate the general expression, Eq. (2.60), for the restricted partition sum. Before going into the details of the calculations, it is instructive to have a look at the geometry of the problem in terms of the dimensionless variables  $\tilde{x}$  and  $\tilde{\rho}$ . Recall that  $\tilde{x}$  and  $\tilde{\rho}$  are measuring the transverse displacement of the tip  $x$  and the stored length  $L - z$  in units of the characteristic transverse and longitudinal length scales,  $L_{\perp}$  and  $L_{\parallel}$ , respectively. As can be inferred from Fig. 2.8, the wall crosses the  $\tilde{x}$ - and  $\tilde{\rho}$ -axis at

$$\eta_{\perp} = \frac{L \cos \vartheta - \zeta}{L_{\perp} \sin \vartheta} \quad \text{and} \quad \eta_{\parallel} = \frac{L \cos \vartheta - \zeta}{L_{\parallel} \cos \vartheta}, \quad (2.81)$$

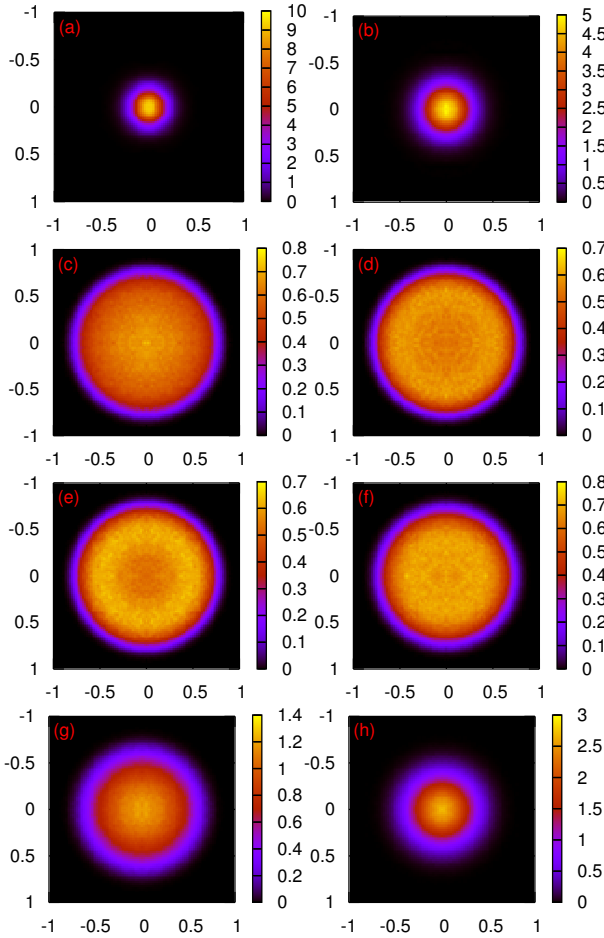


**Figure 2.14** Color density plots of  $P(x, y)$  obtained by MC simulations in  $3d$ : (a)  $\epsilon = 0.05$ , (b)  $\epsilon = 0.1$ , (c)  $\epsilon = 1$ , (d)  $\epsilon = 1.5$ , (e)  $\epsilon = 2$ , (f)  $\epsilon = 3$ , (g)  $\epsilon = 5$  and (h)  $\epsilon = 10$ .

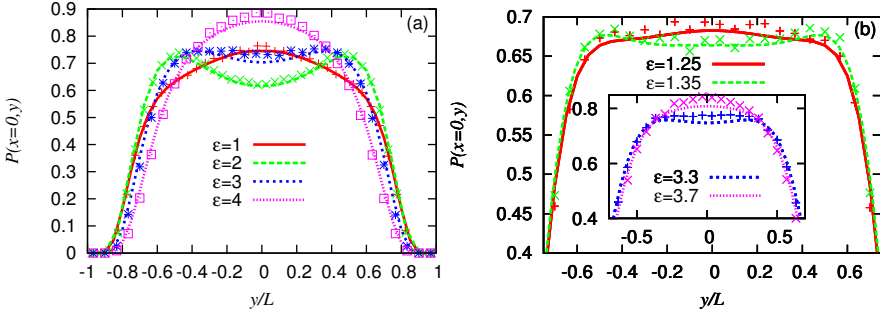


**Figure 2.15** (a) There is a good agreement between our MC simulations (data points) and analytical results (lines) obtained by Semeriyarov and Stepanov (2007). The distribution function displays a biomodal shape and is normalized such that the area under each curve is one. (b) Distribution function has been presented at the onset of bimodality ( $\epsilon = 1.25, 1.35$ ) and in the region of its disappearance ( $\epsilon = 3.3, 3.7$ ).

respectively; see Fig. 2.16. These are the two basic dimensionless variables characterizing the entropic forces exerted on the inclined wall. We also introduce the slope  $\mu = \tan \alpha$  of the constraining wall with respect to the  $\tilde{x}$ -axis

$$\mu = \frac{\eta_{\parallel}}{\eta_{\perp}} = \frac{L_{\perp}}{L_{\parallel}} \tan \vartheta = \frac{1}{\sqrt{3\epsilon}} \tan \vartheta. \quad (2.82)$$

As discussed above, the finite length of the polymer gives a constraint on the reduced stored length  $\tilde{\rho}$  such that it has to be larger than  $\tilde{x}^2/6$ , i.e. above the parabola drawn in Fig. 2.16. Hence, just the points on the constraining wall inside the parabola are accessible to the tip of the polymer. As one moves the wall further away from the grafted end, the number of contact points decreases and finally reduces to zero when the wall becomes tangent to the parabola. In this limit, where

$$\eta_{\parallel}^c = -\frac{3}{2}\mu^2 \quad (2.83)$$

the force exerted on the wall vanishes.

We may now write the restricted partition sum in terms of the reduced stored length  $\eta_{\parallel}$  and the slope of the wall  $\mu$

$$\mathcal{Z}(\zeta, \vartheta) = \tilde{\mathcal{Z}}(\eta_{\parallel}, \mu), \quad (2.84)$$

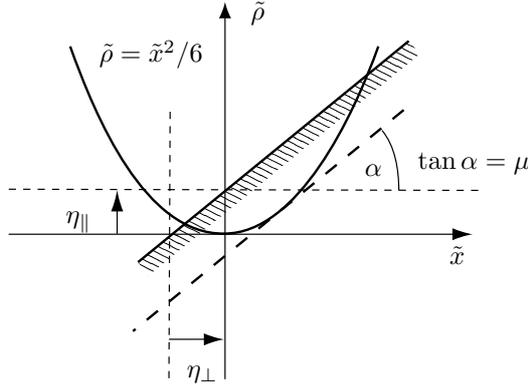


**Figure 2.16** Geometry of the problem in terms of the reduced coordinates  $\tilde{x}$  and  $\tilde{\rho}$ . The position of the wall is characterized by its slope  $\mu = \eta_{\parallel}/\eta_{\perp}$  and  $\eta_{\parallel}$ , the distance from the origin along the  $\tilde{z}$ -axis, i.e. the minimal reduced stored length imposed by the presence of the constraining wall. To harmonic order the finite length of the filament also constrains the reduced stored length  $\tilde{\rho}$  to be larger than  $\tilde{x}^2/6$ .

where

$$\begin{aligned} \tilde{\mathcal{Z}}(\eta_{\parallel}, \mu) &= \frac{1}{2} \operatorname{erfc} \frac{\eta_{\parallel}}{\sqrt{2}\mu} \\ &- \int_0^{\infty} \frac{dq}{\pi q} \Im \left[ e^{iq\eta_{\parallel}} \left( a_3(iq) e^{-\frac{3}{2}(\mu q)^2 b(iq)} - e^{-\frac{1}{2}(\mu q)^2} \right) \right], \end{aligned} \quad (2.85)$$

as shown in Appendix C.4. The force is again found by taking the derivative of  $k_{\text{B}}T \ln \mathcal{Z}$  with respect to  $\zeta$ . It obeys the scaling law

$$f(\zeta, \vartheta, L, \ell_{\text{p}}) = f_c(\vartheta) \tilde{f}(\eta_{\parallel}, \mu), \quad (2.86)$$

with an amplitude

$$f_c(\vartheta) = \frac{\pi^2 \kappa}{4L^2 \cos \vartheta} = \frac{f_c}{\cos \vartheta} \quad (2.87)$$

and a scaling function

$$\tilde{f}(\eta_{\parallel}, \mu) = -\frac{4}{\pi^2} \frac{\tilde{\mathcal{Z}}'(\eta_{\parallel}, \mu)}{\tilde{\mathcal{Z}}(\eta_{\parallel}, \mu)} \quad (2.88)$$

that can be expressed in terms of the restricted partition sum and its derivative

$$\tilde{\mathcal{Z}}'(\eta_{\parallel}, \mu) = - \int_0^{\infty} \frac{dq}{\pi} \Re \left( e^{iq\eta_{\parallel}} a_3(iq) e^{-\frac{3}{2}(\mu q)^2 b(iq)} \right). \quad (2.89)$$

As detailed in Appendix C.4, Eq. (2.85) and Eq. (2.89) are suited best for a numerical evaluation of the entropic force.

In Fig. 2.17, the analytical results for the scaling function  $\tilde{f}(\eta_{\parallel}, \mu)$  of the entropic force are shown as a function of  $\delta\eta_{\parallel} = \eta_{\parallel} - \eta_{\parallel}^c$ , for a series of values of  $\mu$ . Since we have subtracted off the critical value of the reduced stored length  $\eta_{\parallel}^c$ , the forces vanish for  $\delta\eta_{\parallel} \leq 0$ . There is a dramatic difference in the shape of the force-distance curves in 2d and 3d. Whereas the force increases monotonically with increasing  $\delta\eta_{\parallel}$  for 3d, it shows a pronounced maximum in 2d, the physical origin of which is the same as for  $\vartheta = 0$ . The maximum in 2d vanishes upon increasing  $\mu$ , which can either be understood as an increase in the inclination angle or an increase in the persistence length; see Eq. (2.82).

For comparison, MC data are given for a particular value of the stiffness parameter,  $\varepsilon = 0.1$ . In this stiff regime the analytical results compare very well with the MC data, except for large values in the stored length where the harmonic approximation is expected to become invalid.

For small values of  $\mu$ , the reduced stored length  $\eta_{\parallel}$  is no longer a good variable. Instead, we define a new scaling function  $\bar{f}(\eta_{\perp}, \mu)$  such that

$$f(\zeta, \vartheta) = \frac{k_B T}{L_{\perp} \sin \vartheta} \bar{f}(\eta_{\perp}, \mu) \quad (2.90)$$

where

$$\bar{f}(\eta_{\perp}, \mu) = \mu \frac{\pi^2}{4} \tilde{f}(\eta_{\parallel}/\mu, \mu). \quad (2.91)$$

Like in the previous scaling plot, the force should vanish for  $\delta\eta_{\parallel} < 0$ , which in terms of  $\eta_{\perp}$  reads  $\eta_{\perp} < -\frac{3}{2}\mu$ . Again, there is a marked difference between 2d and 3d results; see Fig. 2.18. We also observe that the scaling function  $\bar{f}(\eta_{\perp}, \mu)$  asymptotically approaches a limiting curve for  $\mu \rightarrow \infty$ , which for a fixed value of  $\varepsilon$ , corresponds to  $\vartheta \rightarrow \pi/2$ . It turns out, as we will show now, that this limiting behavior can well be explained within a factorization approximation  $P(x, z) \approx P_{\parallel}(z)P_{\perp}(x)$ . Then,  $\mathcal{Z}(\zeta, \vartheta)$  simplifies to

$$\mathcal{Z}(\zeta, \vartheta) = \int dz P_{\parallel}(z) \mathcal{Z}_{\perp}(\zeta \sin^{-1} \vartheta - z \cot \vartheta). \quad (2.92)$$

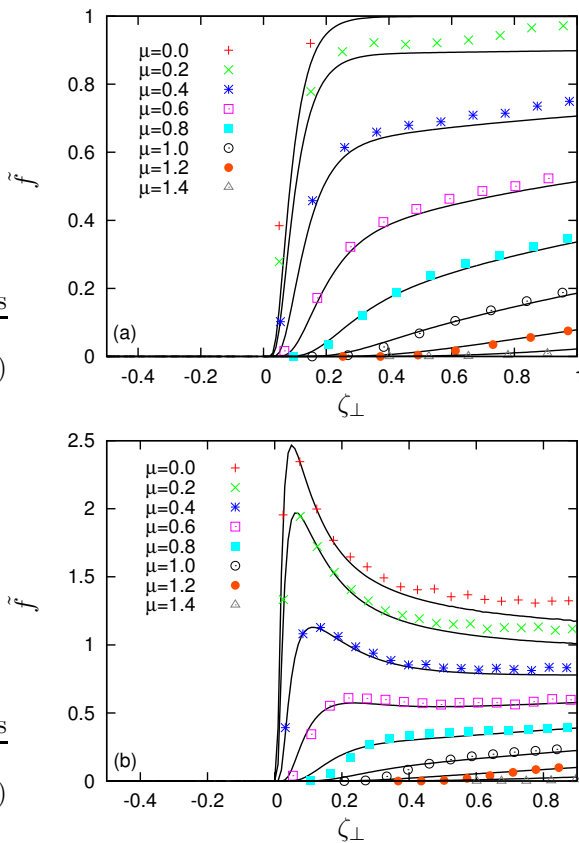


**Figure 2.17** Scaling function of the entropic force  $\tilde{f}$  in (a)  $d = 3$  and (b)  $d = 2$  as a function of  $\delta\eta_{\parallel} = \eta_{\parallel} + \frac{3}{2}\mu^2$  for a series of values of  $\mu$  as indicated in the graphs. Solid lines represent analytical results as obtained from a numerical evaluation of Eq. (2.88). Monte Carlo data for a stiffness parameter  $\varepsilon = 0.1$  are given as symbols, as indicated in the graphs. For  $\mu = 0$ , one recovers the results for  $\tilde{f}_{\parallel}(\eta_{\parallel})$  as discussed in Section 2.3.

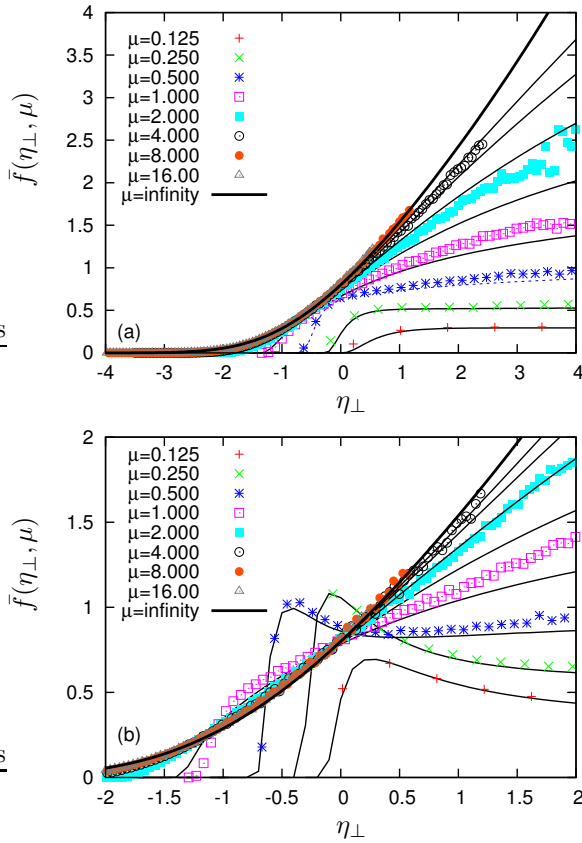


**Figure 2.18** Scaling function  $\bar{f}(\eta_{\perp}, \mu)$  in (a)  $d = 3$  and (b)  $d = 2$  for a series of values for  $\mu$  (solid lines). For large  $\mu$ , the scaling function  $\bar{f}(\eta_{\perp}, \mu)$  asymptotically converges to  $\bar{f}_{\perp}(\eta_{\perp})$  obtained within a factorization approximation. The MC data indicated by different symbols in the graphs are given for a fixed stiffness parameter  $\varepsilon = 0.1$ .

where

$$\mathcal{Z}_\perp(x) = \int_{-\infty}^x dx' P_\perp(x') \quad (2.93)$$

is the restricted partition sum for the transverse fluctuations. The longitudinal distribution function  $P_\parallel(z)$  is, for small  $L/\ell_p$ , strongly peaked at  $z \approx L$  with a characteristic width of  $L_\parallel$ , and  $\mathcal{Z}_\perp$  varies on the scale  $L_\perp$ . Then, for  $\mu \gg 1$ , the width of the longitudinal distribution function is much smaller than the transverse restricted partition sum, such that the integration over  $P_\parallel$  can be approximated by  $\mathcal{Z}(\zeta, \vartheta) \approx \mathcal{Z}_\perp([\zeta - L \cos \vartheta] \sin^{-1} \vartheta)$  which upon using that the transverse distribution function is a simple Gaussian, Eq. (2.64), results in

$$\mathcal{Z}(\zeta, \vartheta) \approx \frac{1}{2} \operatorname{erfc} \frac{\eta_\perp}{\sqrt{2}} =: \bar{\mathcal{Z}}_\perp(\eta_\perp) \quad (2.94)$$

This approximation fails when  $\mu \approx 1$ , which defines an angle

$$\vartheta_c = \arctan(L_\parallel/L_\perp) \approx \sqrt{3L/\ell_p} \quad (2.95)$$

well above which the factorization approximation is valid. The entropic force is then

$$f(\zeta, \vartheta) = \frac{k_B T}{L_\perp \sin \vartheta} \bar{f}_\perp(\eta_\perp), \quad (2.96)$$

where

$$\bar{f}_\perp(\eta_\perp) = -\frac{\bar{\mathcal{Z}}'_\perp(\eta_\perp)}{\bar{\mathcal{Z}}_\perp(\eta_\perp)} = \sqrt{\frac{2}{\pi}} \frac{e^{-\eta_\perp^2/2}}{\operatorname{erfc}(\eta_\perp/\sqrt{2})}. \quad (2.97)$$

This result for the scaling function of the entropic force is indicated as the thick solid line in Fig. 2.18. It becomes exact in the limit  $\vartheta = \pi/2$ , where starting from Eq. (2.60) one can integrate out the longitudinal coordinate to end up with

$$\mathcal{Z}(\zeta, \frac{\pi}{2}) = \frac{1}{2} \operatorname{erfc} \left( \frac{-\zeta}{\sqrt{2}L_\perp} \right). \quad (2.98)$$

Finally, for large  $\zeta$ , one recovers the linear response result  $f(\zeta, \pi/2) = 3\kappa\zeta/L^3$ .

If we compare the results of the factorization approximation for  $\vartheta > \vartheta_c$ , Eq. (2.96) and Eq. (2.97), to Eq. (2) and Eq. (5) of Ref. Mogilner and Oster

(1996a), one realizes that they are almost identical up to the minor difference that Mogilner and Oster define their  $\kappa_0$  to be  $4\kappa/L^3$  where it actually should be  $3\kappa/L^3$ . The factor 4 in Mogilner and Oster (1996a) instead of the correct value 3 is the result of assuming that the minimal energy configuration of a thin rod bent by application of a force to its non-grafted end has constant radius of curvature for small deflections, which is not the case. In fact, the boundary condition of the mechanical problem forces the curvature to vanish at the non-grafted end. In Mogilner and Oster (1996a), the entropic force was calculated by taking into account the transverse fluctuations of the grafted polymer only and completely disregarding any stored length fluctuations. Here, the factorization approximation, which treats longitudinal and transverse fluctuations as independent, gives the same result for inclination angles  $\vartheta > \vartheta_c$ . The reason behind the validity of the asymptotic results, Eq. (2.96) and Eq. (2.97), is that the tip distribution function is much narrower in the longitudinal than the transverse direction for  $\vartheta \gg \vartheta_c \sim \sqrt{L/\ell_p}$ . Hence the range of validity of the factorization approximation becomes larger as the polymers become stiffer. Of course, the analysis by Mogilner and Oster (1996a) has to fail for small inclination angles since it does not account for stored length fluctuations at all. This is seen most dramatically for  $\vartheta = 0$ , where such an approximation would give no force at all in contrast to what we find in Section 2.3.

### 2.4.3 Entropic forces: explicit results

The analysis in the previous section gives the full scaling picture for the entropic forces as a function of the scaling variables  $\eta_{\parallel}$  and  $\eta_{\perp}$ . Here we discuss our findings in terms of the actual distance of the grafted end to the wall  $\zeta$ , the inclination angle  $\vartheta$ , and the stiffness parameter  $\varepsilon = L/\ell_p$ , which may be more convenient for actual applications. Of course, the disadvantage of such a representation is that we now have to give the results for particular values of the stiffness parameter. In this section, we first discuss the results in  $3d$  and then compare it to the  $2d$  case.

In Figs. 2.19 and 2.20, the force  $f$  in units of the Euler buckling force  $f_c$  is shown as a function of  $\zeta$  (in units of the total filament length  $L$ ) for a series of values of  $\vartheta$  and vice versa ( $d = 3$ ); the stiffness parameter has been taken as  $\varepsilon = 0.1$ . Recall that the angle  $\vartheta = 0$  corresponds to a wall perpendicular to the orientation of the grafted end of the polymer, which has been discussed in detail in Section 2.3. Upon increasing the inclination angle  $\vartheta$ , the entropic force decreases for all given values of  $\zeta$ . This is to be expected since the wall then cuts off less from the probability cloud of the polymer tip. For the same reason the forces also decrease with

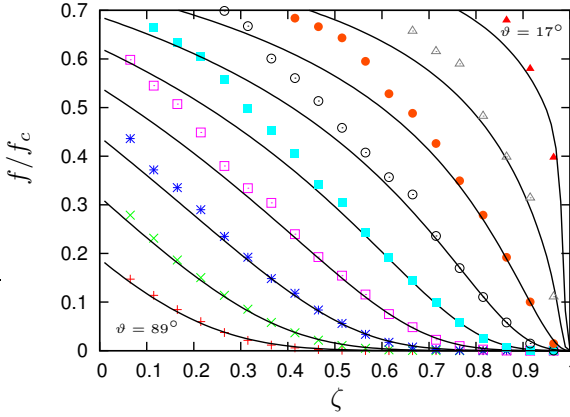


**Figure 2.19** Analytical and MC simulation results for the entropic force  $f/f_c$  as a function of the distance of the grafted end from the wall  $\zeta/L$  for a series of inclination angles  $\vartheta = 17^\circ, \dots, 89^\circ$  with steps  $9^\circ$  ( $d=3$ ).

increasing  $\zeta$  for a given value of  $\vartheta$ . The analytical results (solid lines) agree well with the MC data for not too small values of  $\zeta$ . The deviations grow larger upon decreasing the distance between the wall and the grafted end. Then non-linear effects are not taken into account by our weakly bending approximation set in.

In the limit as the inclination angle approaches  $\pi/2$ , it is certainly no longer justified to calculate the entropic force by assuming that only the polymer tip is not allowed to penetrate the membrane. Then, one has to take into account the fact that also the body of the polymer is constrained by the presence of the wall. Since this reduces the number of allowed polymer configurations even further, this effect is expected to lead to an enhancement of the entropic force. Indeed this is the case, as one may infer from Fig. 2.21, where we show a comparison with MC simulation accounting for these constraints. One also notes that the enhancement of the entropic forces becomes largest as  $\vartheta \rightarrow \pi/2$  and the distance between the wall and the grafted end becomes small.

For comparison, Fig. 2.22 shows the entropic force  $f$  in  $2d$  as a function of  $\vartheta$  for different values of  $\zeta$ . Inspection of this figure immediately tells us that in contrast to  $3d$  decreasing  $\zeta$  (for a given value of  $\vartheta$ ) is not always increasing the entropic force.

Finally, we would like to compare our full results in  $3d$  with the fac-

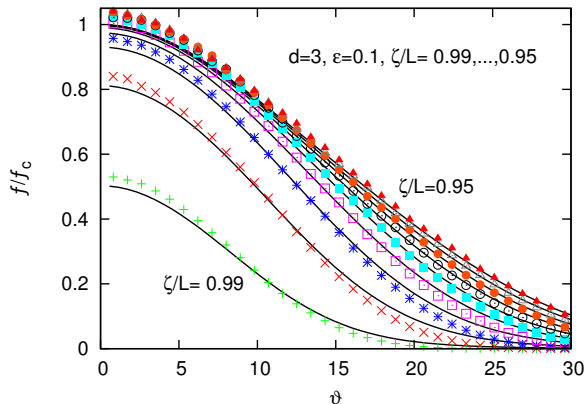


**Figure 2.20** Analytical and MC simulation results for the entropic force  $f/f_c$  as a function of the inclination angle  $\vartheta$  (in degrees) for a series of distances to the wall  $\zeta/L = 0.99, 0.985, \dots, 0.95$ .

torization approximation discussed in the previous section, Eq. (2.97), which when corrected for some minor factor is identical to the results given by Mogilner and Oster (1996a). The comparison is given in Fig. 2.23 for a stiffness parameter  $\varepsilon = 0.1$ . In the limit of large inclination angles well above  $\vartheta_c \approx 30^\circ$ , there is excellent agreement between the factorization approximation and the full results for not too small values of  $\zeta$ . As one approaches  $\vartheta_c$ , the range of validity of the factorization approximation shrinks and finally it becomes invalid for  $\vartheta < \vartheta_c$ .

To illustrate the applicability of the factorization approximation, let us take some examples. For the cytoskeletal filament F-actin with a contour length 100 nm and persistence length  $\ell_p = 15 \mu\text{m}$ , the stiffness parameter becomes  $\varepsilon = 0.006$  which gives  $\vartheta_c \approx 7.6^\circ$ . Upon increasing the stiffness parameter to  $\varepsilon = 0.1$ , which amounts to changing the contour length to a value of  $L = 1.6 \mu\text{m}$ , the critical angle  $\vartheta_c$  increases to  $28.7^\circ$ .

## 2.5 Protrusion velocity and intercalation probability

In this final section, we would like to apply our results to calculate the protrusion velocity for an idealized model system. This serves to illustrate

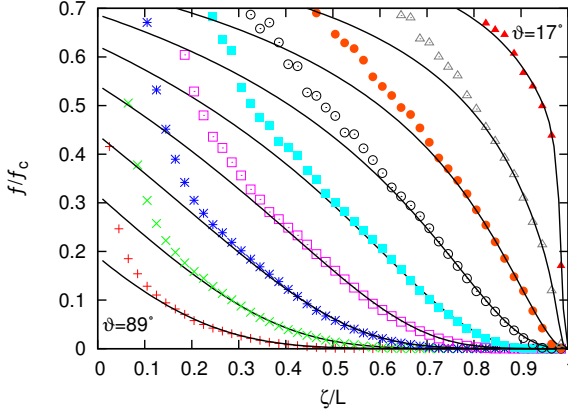


**Figure 2.21** Comparison of the analytical results for the entropic force as a function of  $\zeta/L$  (solid lines) for a series of values for  $\vartheta = 17^\circ, \dots, 89^\circ$  with steps  $9^\circ$  indicated in the graph with MC simulations (symbols in the graph), which take into account the constraints of the wall on the body of the polymer;  $\varepsilon = 0.1$ . The deviations are most pronounced for small values of  $\zeta$  and inclination angles  $\vartheta$  close to  $\pi/2$  ( $d=3$ ).

how the theoretical results obtained in this paper may be applied to arrive at a microscopic model for cell motility. As illustrated in Fig. 2.24, we consider a semiflexible polymer mesh, where each filament is inclined at a fixed angle  $\vartheta$  with respect to a membrane, which - for simplicity - is idealized as a rigid smooth wall. We ask for the average protrusion velocity of the polymerizing mesh pushing against a membrane which is under a constant external load  $f$ .

For a monomer to be appended to the tip of fluctuating semiflexible polymer near the rigid wall, the distance between tip and the wall must be at least  $\delta \cos \vartheta$  where  $\delta$  is the increase in polymer length due to the addition of a single monomer. For actin,  $\delta$  would be half a monomer radius or  $\delta \approx 2.7$  nm. The intercalation probability is given by

$$p(\zeta, \vartheta, \delta) = \frac{Z(\zeta - \delta \cos \vartheta, \vartheta)}{Z(\zeta, \vartheta)}. \quad (2.99)$$

Biologically relevant parameters are  $L \approx 30$  nm and  $\ell_p \approx 15$   $\mu$ m which corresponds to  $\vartheta_c = 4.5^\circ$  and a critical force of  $f_c \approx 150$  pN. For a given external force  $f$ , we may now find  $\zeta$  and  $\vartheta$  such that  $f(\zeta, \vartheta) = f$ . Then, following Mogilner and Oster (1996a), the intercalation probability can

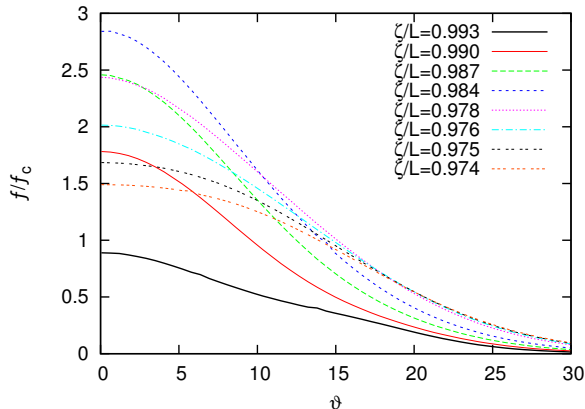


**Figure 2.22** Analytical results for the entropic force  $f/f_c$  as a function of the inclination angle  $\vartheta$  (in degrees) for different values of distances to the wall ( $d = 2$ ); stiffness parameter has been taken as  $\epsilon = 0.1$ . MC data points has been removed for more clarity

(under certain assumptions) be converted into a protrusion velocity of the tip

$$v(f, \vartheta) = \delta \cos \vartheta [k_{\text{on}} M p(\zeta(f, \vartheta), \vartheta, \delta) - k_{\text{off}}], \quad (2.100)$$

where  $M$  is the monomer concentration and  $k_{\text{on}}$  and  $k_{\text{off}}$  are the monomers attachment and detachment rates, respectively. Fig. 2.25a displays the velocity as a function of the inclination angle  $\vartheta$  and a set of forces ranging from 0.1 pN to 2.9 pN. The main feature of this figure is that the filament growth velocity is not a monotonic function of the angle  $\vartheta$ , but passes through a maximum at an optimal filament orientation  $\vartheta_{\text{opt}}$ . The physical reason for such an optimal angle is obvious. On the one hand, thermal fluctuations may not be able to bend a stiff polymer like actin which is grafted normal to the wall to permit intercalation. On the other hand, a filament polymerizing freely parallel to the wall is not able to exert force. In general,  $\vartheta_{\text{opt}}$  is an increasing function of the load force and the persistence length. For the parameters listed in Fig. 2.25a, this angle ranges from  $\vartheta_{\text{opt}} \approx 60^\circ$  at 0.1 pN to  $\vartheta_{\text{opt}} \approx 75^\circ$  at 2.9 pN. If the persistence length is lowered to  $\ell_p \approx 1 \mu\text{m}$ , the optimal angle is considerably decreased; compare Fig. 2.25b. We have also included a plot for the protrusion velocity generated using the factorization approximation for all angles. We find qualitatively the same behavior as for the full expression but significant

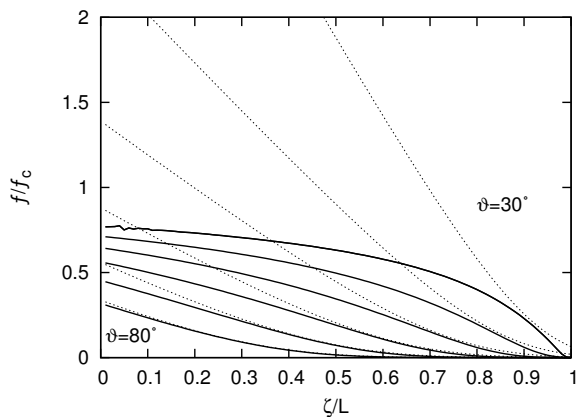


**Figure 2.23** Comparison of the full result for the entropic force as a function of  $\zeta/L$  (full lines) with the results obtained from the factorization approximation (dashed lines) for a stiffness parameter  $\varepsilon = 0.1$  and a series of inclination angles  $\vartheta = 30^\circ, 40^\circ, \dots, 80^\circ$ . The range of validity of the factorization approximation broadens as one increases the inclination angle  $\vartheta$ ; it is invalid for  $\vartheta$  smaller than  $\vartheta_c \approx 30^\circ$ .

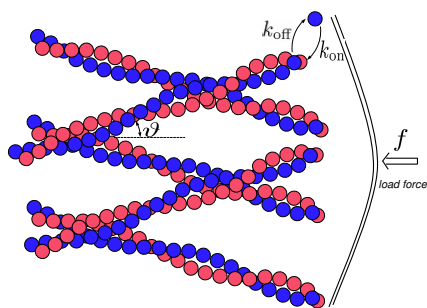


**Figure 2.24** An actin network polymerizing in the presence of an external load.  $\vartheta$  is the network orientation,  $k_{\text{on}}$  is the monomers attachment rate and  $k_{\text{off}}$  is the monomers detachment rate. The membrane - for simplicity - has been idealized as a rigid smooth wall.

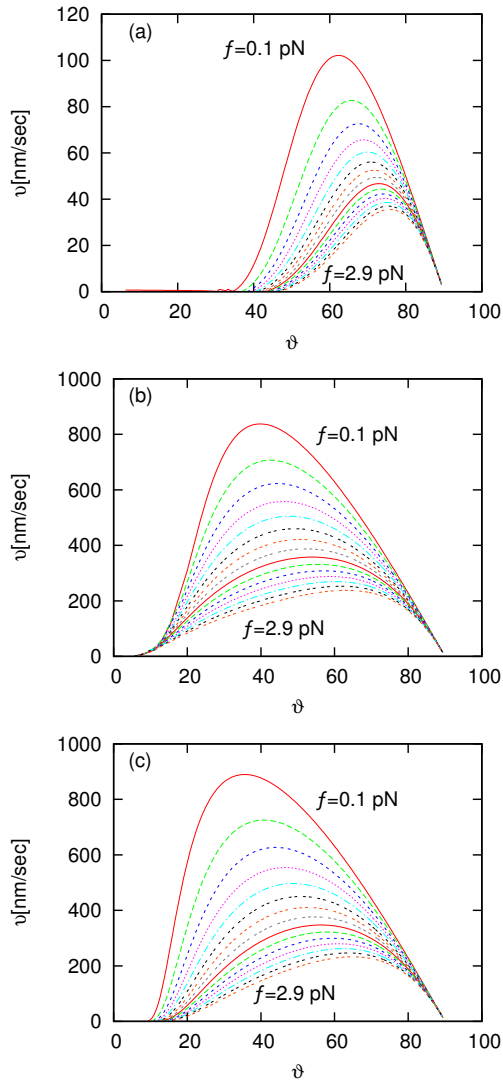


**Figure 2.25** Protrusion velocity  $v$  versus inclination angle  $\vartheta$  (in degrees) for different load forces  $f = 0.1$  pN, ..., 2.9 pN with steps 0.2 pN obtained using (a) full expressions with  $\ell_p = 15 \mu\text{m}$  (b) full expressions with  $\ell_p = 1 \mu\text{m}$ , (c) factorization approximation with  $\ell_p = 1 \mu\text{m}$ . Parameters are  $L = 30$  nm,  $k_{\text{on}}M = 110 \text{ sec}^{-1}$  and  $k_{\text{off}} = 1 \text{ sec}^{-1}$ .

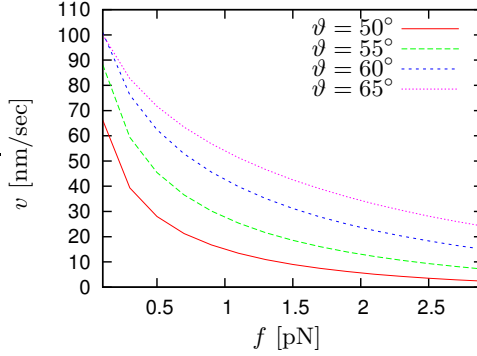


**Figure 2.26** Protrusion velocity  $v$  decreases as external force  $f$  increases. Parameters are  $L = 30$  nm,  $\ell_p = 15$   $\mu$ m,  $k_{on}M = 110$  sec $^{-1}$ .

quantitative differences (see Fig. 2.25c).

For completeness, we add Fig. 2.26 presenting decay in protrusion velocity as the external load force increases obtained using full expressions for a fix network orientation  $\vartheta$ .

## 2.6 Summary

In summary, we have presented analytical calculations and extensive Monte Carlo simulations for the entropic force  $f$  exerted by a grafted polymer on a rigid obstacle (wall). The scale for the magnitude of the entropic force is given by the *Euler buckling force*  $f_c \propto k_B T \ell_p / L^2$ . The *stiffness parameter*  $\varepsilon = L / \ell_p$  discerns the two universal regimes of a Gaussian chain ( $\varepsilon \gg 1$ ) and a semiflexible chain ( $\varepsilon \ll 1$ ). In this thesis, we have mainly focused on the *stiff limit*, where analytical calculations using a weakly bending rod approximation are possible. In comparing our results with Monte Carlo simulations, we have found that the range of applicability of the results obtained in the stiff limit extend to stiffness parameters as large as  $\varepsilon = 0.1$ . Qualitatively the asymptotic results remain valid even up to  $\varepsilon = 1$ .

For the simplest possible geometry, where the polymer is perpendicular to the wall, located at a distance  $\zeta$  from the grafted end, our analytical calculations show that the entropic force obeys a scaling law in the stiff limit

$$f_{\parallel}(\zeta, L, \ell_p) = f_c \tilde{f}_{\parallel}(\tilde{\eta}) \quad (2.101)$$

with the scaling variable  $\tilde{\eta} = (L - \zeta)/L_{\parallel}$  measuring the minimal compression of the filament in units of the longitudinal width of the tip distribution function  $L_{\parallel} = L^2/\ell_p$ , and  $f_c$  the Euler buckling force of a classical beam. For small values of the scaling variable we have derived a simple analytical expression, Eq. (2.45),

$$\tilde{f}_{\parallel}^{<}(\tilde{\eta}) = \frac{4}{\pi^{5/2}} \frac{\exp[-1/4\tilde{\eta}]}{\tilde{\eta}^{3/2} [1 - 2\text{erfc}(1/2\sqrt{\tilde{\eta}})]} \quad (2.102)$$

and a corresponding formula in 2d, Eq. (2.58), which describe the full scaling function to a high numerical accuracy for  $\tilde{\eta} \leq 0.2$ . For  $\tilde{\eta} \geq 0.2$ , there are equally simple expressions, as for example Eq. (2.46) for 3d. We expect these formulas to be useful for molecular models of cell motility. The shape of the scaling function shows dramatic differences between 2d and 3d, which are of geometric origin. In 3d the entropic forces always stay below the Euler buckling force. In contrast, in 2d it is larger than the mechanical limit for most of the parameter space and exhibits a pronounced maximum at small values of the scaling variable  $\tilde{\eta}$  before it steeply drops to zero as  $\zeta \rightarrow L$ .

Extensive Monte Carlo simulations confirm these analytical results and show that their range of applicability is  $\varepsilon \leq 0.1$ . For larger values of the stiffness parameter, there are clear deviations from the stiff scaling limit, which become qualitative for  $\varepsilon \geq 1$ . Features of the stiff limit, such as the maximum in the entropic force, are visible even for  $\varepsilon$  as large as 4.

Experimentally, one should be able to measure entropic forces in 2d and compare it to 3d. For example, 2d force measurements may be feasible by confining the filament to fluctuate between two parallel plates. Since in some important biological systems like the leading edge of a crawling cell, the system is effectively 2d, these kind of experiments might also help to understand better a complex system like a lamellipodium.

For a polymer inclined at an angle  $\vartheta$  with respect to the wall, the transverse width  $L_{\perp} = \sqrt{L^3/3\ell_p}$  of the tip distribution function plays also a significant role; note that the ratio  $L_{\parallel}/L_{\perp} = \sqrt{3\varepsilon}$ . The entropic force can now be written in the scaling form

$$f(\zeta, \vartheta; L, \ell_p) = f_c(\vartheta) \tilde{f}(\eta_{\parallel}, \eta_{\perp}), \quad (2.103)$$

where  $\eta_{\perp} = (L \cos \vartheta - \zeta)/(L_{\perp} \sin \vartheta)$ ,  $\eta_{\parallel} = (L \cos \vartheta - \zeta)/(L_{\parallel} \cos \vartheta)$  and  $f_c(\vartheta) = f_c/\cos \vartheta$ . It turned out that a proper choice of scaling variables are  $\mu = \eta_{\parallel}/\eta_{\perp} = (L_{\perp}/L_{\parallel}) \tan \vartheta$  and  $\eta_{\parallel}$  or  $\eta_{\perp}$  depending on whether the inclination angle is smaller or larger than a characteristic angle  $\tan \vartheta_c = L_{\parallel}/L_{\perp}$ , i.e.  $\mu_c = 1$ . Upon increasing the inclination parameter  $\mu$ , the shape

of the scaling function changes from a step-function-like form at  $\mu = 0$  to a purely convex shape as  $\mu \rightarrow \infty$ . The limit  $\mu \rightarrow \infty$  either corresponds to  $\vartheta \rightarrow \pi/2$  or for a fixed  $\vartheta \neq 0$  to the stiff limit  $\varepsilon \rightarrow 0$ . For 2d, in addition, the maximum vanishes at  $\mu \approx 0.6$ .

In the limit of inclination angles which are much larger than the characteristic angle  $\vartheta_c$ , we have found that an approximation, Eq. (2.96) and Eq. (2.97), based on factorizing the joint probability distribution of the polymer tip gives an excellent asymptotic representation of the full analytical results:

$$f(\zeta, \vartheta) = \frac{k_B T}{L_\perp \sin \vartheta} \sqrt{\frac{2}{\pi}} \frac{e^{-\eta_\perp^2/2}}{\operatorname{erfc}(\eta_\perp/\sqrt{2})}. \quad (2.104)$$

It is simpler than the full scaling form since it only depends on one scaling variable. Up to minor factors this asymptotic formula for the entropic force is mathematically identical to the results found by Mogilner and Oster (1996a), which was derived upon assuming that the tip of the polymer fluctuates perpendicular to its contour only. Since  $\tan \vartheta_c \propto \sqrt{\varepsilon}$  the range of applicability of this results grows with increasing stiffness parameter. For example,  $\vartheta_c$  equals approximately  $30^\circ$  and  $10^\circ$  for stiffness parameter  $\varepsilon$  equal to 0.1 and 0.006, respectively. For  $\vartheta \leq \vartheta_c$  the factorization approximation fails completely, since it gives an incorrect description of the longitudinal stored length fluctuations. Then, a full analysis in terms of a two parameter scaling function is necessary.

We have shown that filaments in a polymerizing network grow fastest in a preferred direction  $\vartheta_{\text{opt}}$ , such that one should expect that the population of those filaments growing near the optimal angle will be dominant. If the optimal angle  $\vartheta_{\text{opt}}$  is larger than the critical angle  $\vartheta_c$ , which is the case for an actin network with  $\ell_p \approx 15 \mu m$ , then one can to a large degree use the results from the factorization approximation.



# 3 Entropic forces exerted by an actin network on a sphere

## 3.1 Introduction

The past 10 years have seen remarkable advances in understanding the molecular basis of actin-driven motility (Pollard and Borisy, 2003; Pantaloni *et al.*, 2001). In all existing microscopic models, such as the Brownian ratchet model, the effects of curvature of the load surface on the generating force and polymerization velocity is not taken into account, although curvature might play an important role in the magnitude of the entropic force acting on the ActA-coated beads and vesicles in *in vitro* experiments. In the experiments of Cameron *et al.* (1999, 2000, 2001), the velocity of the plastic beads coated with ActA, depends on the size: larger beads move faster. They were also able to control the density of the actin tail by varying the bead size and ActA concentration but the density of ActA had little effect on the average speed. Filaments nucleate at the bead surface and subsequently detach such that the filament-bead interaction is not permanent and undergoes cycles of association and dissociation events. At optimal ActA concentration, often fewer than 10 filaments from the tail had contact with the surface of  $0.2 \mu\text{m}$  beads, which was sufficient for motility.

Here, we use our analytical results from Sec. 2.4 to numerically calculate the total entropic force generated by a very simple actin network on a sphere with radius  $R$ . The actin tail in a real experiment has a dendritic organization with filaments of different length and orientation. However, here, for simplicity we consider an idealized network of actin filaments, all with the same length and orientation and anchored firmly on the dense part of the actin gel. We also assume that each filament acts independently. The density of the actin tail is in general a function of the radius of the sphere and the density of the ActA protein. We consider that a fixed number,  $N$ , of filaments are crowded behind a sphere which is located at a constant distance  $\zeta$  from the graft wall (Fig. 3.1). This analysis is not realistic enough to describe actual experimental systems, but may serve as a necessary prerequisite for more detailed theoretical models. We proceed

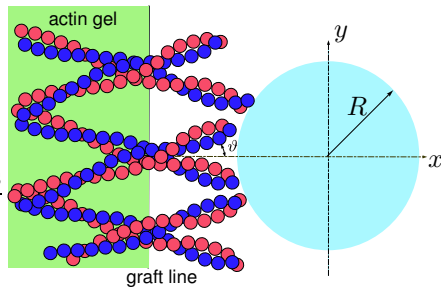


**Figure 3.1** A hard sphere constrains the fluctuations of a network of stiff polymers, oriented at an angle  $\vartheta$ , resulting in the average repulsive force between the sphere and the polymer network. One end of free fluctuating filaments is firmly anchored in the dense part of the actin gel (graft line).

as follows: Sec. 3.2, represents our analysis of a polymer network with a generic geometry of the graft surface pushing against an obstacle. We formulate the problem for a very general case and then analyse it for two specific examples: i) a sphere with radius  $R$  (Sec. 3.3) and ii) a *Listeria*-like object with radius  $R$  and length  $L$  (Sec. 3.4). At the end, we give a discussion of our main results.

## 3.2 An inhomogeneous actin network and a rigid obstacle

Consider an inhomogeneous stiff actin network fluctuating in front of an obstacle (such as bacteria) with an arbitrary shape (Fig. 3.2). The actin filaments are anchored firmly within an actin gel. The anchoring point of each filament, which fixes the position and orientation of the filament, characterizes a so called “graft surface” of the network. The graft surface might have any arbitrary shape. In the next section, for simplicity, we consider it as a flat or spherical surface. We also neglect all steric repulsions between filaments. Filaments can flex by Brownian motion, i.e. they exhibit thermal fluctuations in their shape. The presence of the obstacle reduces the number of possible configurations for each filament leading to an increase in free energy and as a result a total pushing force on the obstacle which is entropic in origin. Since the actin filaments are stiff ( $\ell_p \approx 15 \mu\text{m}$ ), they fluctuate around the completely stretched configuration. Filaments

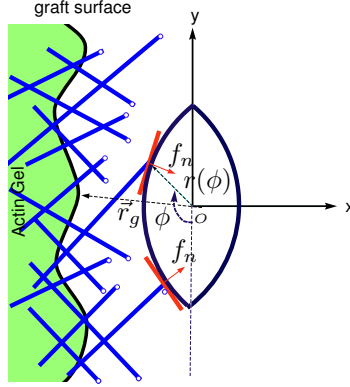


**Figure 3.2** An inhomogeneous actin network fluctuating in front of an obstacle with arbitrary geometry. The actin network exerts a repulsive force on the obstacle which is entropic in its origin.  $O$  is the centre of mass of the obstacle.

which are long enough to hit the obstacle, feel locally a plane wall, which is tangent to the object at the interacting point. In other words, the tip of each stiff filament experiences a plane wall which has different orientations at different interacting points. Since we have assumed that each filament works independently, the total entropic force due to the network on the object is just the sum over the entropic forces of each single filament. For a given shape of the obstacle and graft surface, we need to integrate over the length and angle distribution of the free fluctuating part of the actin network in order to evaluate the total entropic force

$$\vec{F} = \int r(\phi) d\phi \int d\vartheta \int dL C_{\phi, \{\vec{r}_g\}}(L, \vartheta) \times f_n(L, \ell_p, \vartheta, \vec{r}_g, \phi, r(\phi)). \quad (3.1)$$

Here,  $C_{\phi, \{\vec{r}_g\}}(L, \vartheta)$  is the number of polymers per unit length between  $\phi$  and  $\phi + d\phi$ , with orientation  $\vartheta$  and contour length  $L$ .  $f_n$  is the entropic force exerted by the filament grafted at  $\vec{r}_g$  and hitting the barrier at  $r(\phi)$ .

The length of the thermally fluctuating parts of these polymers are typically  $200 \sim 300$  nm, which is very short compared to their persistence length. At any point on the surface of the obstacle, the force  $f_n$  is perpendicular to the local tangent plane at that point. Obviously, the total force which has in general both  $x$  and  $y$  components, depends on the network geometry characterized by  $C_{\phi, \{\vec{r}_g\}}(L, \vartheta)$ , the geometry of the obstacle given by  $\{\phi, r(\phi)\}$  and the geometry of the graft surface given by  $\{\vec{r}_g\}$ . This

concludes the general framework for entropic forces generated by a polymer brush on an arbitrary shaped rigid object. In the following two sections, we present the results for a sphere and a rod-like object, which are analyzed in detail.

### 3.3 A homogeneous actin network and a sphere

In this section, we numerically calculate the integral in Eq. (3.1) for a homogeneous non-polymerizing actin network. One end of each filament is firmly anchored on a flat graft surface and the other free end undergoing thermal fluctuations and exerting force on the bead. For simplicity, we assume that half of the filaments are oriented at an angle  $\vartheta$  and the other half at  $-\vartheta$ , with all of them of the same contour length  $L$ . We define  $\zeta$  to be the minimal distance between the sphere and the graft surface (Fig. 3.3).

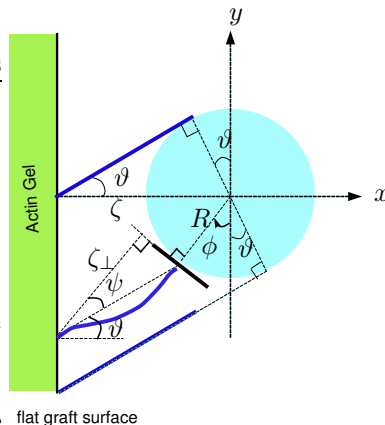


**Figure 3.3** Geometry which has been used to calculate the entropic force on a bead. The two filaments tangent to the sphere at  $-\vartheta$  and  $\pi - \vartheta$  are the first and last filaments which (if they are long enough to feel the presence of the bead) are able to exert force on it giving  $-\vartheta \leq \phi \leq \pi - \vartheta$ .

As already mentioned, we assume that each filament which hits the surface of the bead, effectively sees the flat tangent-plane at the contact point to the sphere as a barrier (Fig. 3.3). This assumption is valid for a stiff filament like actin with persistence length of  $\ell_p \approx 15 \mu\text{m}$ . The problem of calculating the total entropic force on the sphere, reduces to an integration

over the force of each single filament grafted at  $\psi = \frac{\pi}{2} - (\theta + \phi)$  and fluctuating in front of a rigid wall at distance  $\zeta_{\perp} = (\zeta + R - R \sin \phi) \cos \psi / \cos \theta$  with  $\phi$  changing from  $-\vartheta$  to  $\pi - \vartheta$ . The force of each stiff filament at the contact point is perpendicular to the local tangent surface or, in other words, is directed to the centre of the bead. We are interested in the total force in  $x$  and  $y$  directions. For symmetry reasons, the total force in the  $y$  direction vanishes, and the force in  $x$  direction (per single filament) is given by

$$f_s(\zeta, \vartheta, R) = F_x / (n\pi R) = \frac{1}{\pi} \int_{-\vartheta}^{\pi-\vartheta} f_n(\phi) \sin \phi d\phi, \quad (3.2)$$

where  $n$  is the linear density of actin filaments and  $f_n$  will be calculated from Eq. (2.88).

In a real experiment, the filaments nucleate at the bead surface and subsequently detach. Hence the assumption that all filaments have on average the same contour length would suggest that a spherical graft surface might be a better choice (see Fig. 3.4).

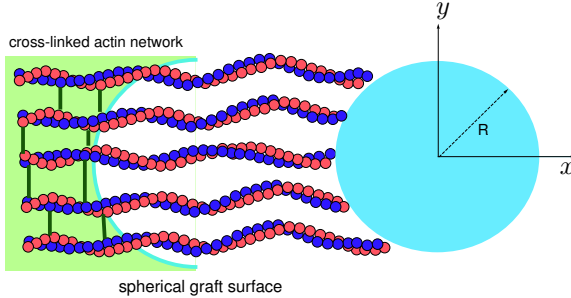


**Figure 3.4** A schematic presentation of an actin network with a spherical graft surface pushing against a sphere.

Fig. 3.5 displays  $f_n(\phi)$  as a function of  $\phi$  for  $\vartheta = 0$  for both a flat and a spherical graft surface.  $f_n$  has been scaled with  $f_c = \pi^2 \ell_p k_B T / 4L^2$ , which is the Euler buckling force. For  $\vartheta = 0$ ,  $f_n$  is symmetric around its maximum at  $\phi_{\max} = \pi/2$ . Thus the filament directing to the bead at  $\phi_{\max}$  is the most efficient pushing filament. For a flat graft surface, the force is nonzero for  $\phi_c < \phi < 180^\circ - \phi_c$ . It is not difficult to calculate the value of  $\phi_c$  at which the force vanishes. The condition that the filament should have contact

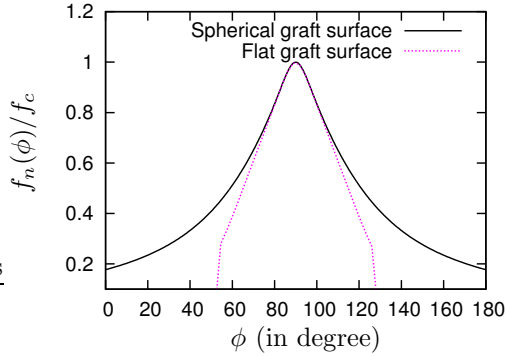


**Figure 3.5** Force  $f_n(\phi)$  in units of  $f_c$  as a function of  $\phi$  for  $\vartheta = 0$ ,  $\zeta/L = 0.85$ ,  $R/L = 0.5$  and  $L/\ell_p = 0.1$  for a flat and spherical graft surface.

with the surface of the sphere implies that  $L \cos \psi > \zeta_{\perp}$ , which for  $\vartheta = 0$ ,  $\zeta/L = 0.8$ ,  $R/L = 1$  and  $L/\ell_p = 0.1$  gives  $\phi_c = 53.1^\circ$ . For a spherical graft surface, all the filaments hitting the bead at  $0^\circ < \phi < 180^\circ$  are able to exert a force.

We now turn to a discussion of the total force  $F_x$  exerted on the bead, restricting ourselves first to a flat graft surface. See Fig. 3.6a and Fig. 3.6b for an illustration of  $F_x$  as a function of  $\vartheta$  and a fixed value of  $\zeta$  but a series of values for  $R$  and vice versa. In both cases, the total force vanishes when the orientation of the network is larger than a maximum angle  $\vartheta_{\max}$ . For constant  $\zeta$ , it is easy to approximate the value of  $\vartheta_{\max}$  at which the force goes to zero. The polymer directed to the sphere at an angle  $\phi = \pi/2$  is pushing the sphere most efficiently (see Fig. 3.5). When the total force vanishes, this means that even this polymer is not pushing anymore. In other words, the distance of this filament to the sphere is larger than its contour length,  $\zeta_{\perp} > L \cos \vartheta$ . As a result, whenever  $\vartheta > \vartheta_{\max} = \cos^{-1}(\zeta/L)$ , the force vanishes. Since  $\vartheta_{\max}$  is independent of  $R$ , the force vanishes at the same value of  $\vartheta_{\max} = \cos^{-1}(0.95) \sim 18^\circ$  for different values of  $R$  (see Fig. 3.6a). However, changing  $\zeta/L$ , would change  $\vartheta_{\max}$ , as presented in Fig. 3.6b.

Another feature of Fig. 3.6a is that for a constant linear density of working filaments  $n$ , which corresponds to a total number  $n\pi R$  of filaments, the force per single filament  $f_s$  is higher for smaller spheres. However, the total force  $F_x = f_s \times n\pi R$  is higher for larger spheres since the number of pushing filaments for fixed  $n$  is proportional to  $R$ . Here, for simplicity, we

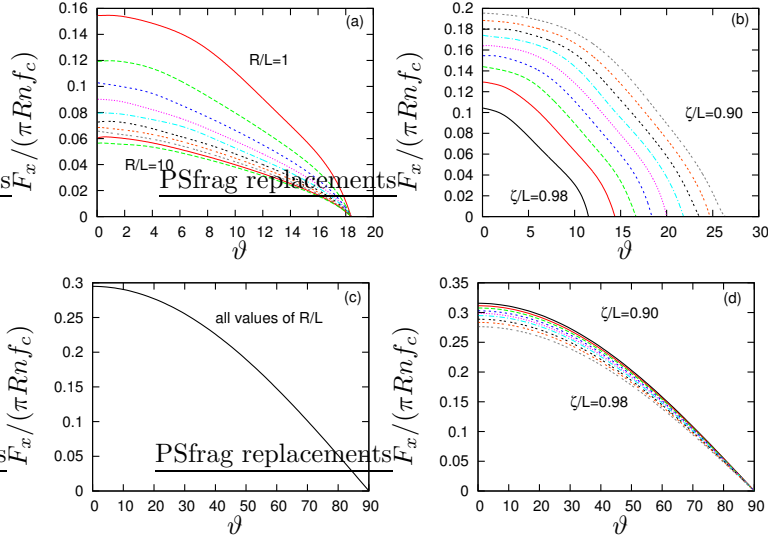


**Figure 3.6** Plot of the dimensionless force per single filament as a function of  $\vartheta$  (in degrees), exerted by a homogeneous network of stiff polymers with a flat graft surface and linear density  $n$  on (a) spheres with different radius  $R$  but the same  $\zeta/L = 0.95$ , and on (b) a sphere with radius  $R/L = 1$  but located at different  $\zeta/L$  with  $L/\ell_p = 0.1$ . (c) and (d) are the same as (a) and (b) with a spherical graft surface.

have assumed that  $n$  is not a function of  $\phi$  but can be a function of  $R$ . One can also keep the size of the bead fixed and decrease  $\zeta$ . Obviously, this will increase the total entropic force and increase  $\vartheta_{\max}$  (Fig. 3.6b).

In order to see the effect of the graft surface geometry, we have calculated the total entropic force for a spherical graft surface as well. As expected, the force drops down by a factor  $\cos \vartheta$  and the average force per filament collapses to a single curve for different values of  $R/L$  but the same value of  $\zeta/L$  (Fig. 3.6c). Again, moving the bead closer to the network increases the force per single filament (Fig. 3.6d). In contrast to a flat graft surface, where just those filaments hitting the bead at  $\phi_c < \phi < 180 - \phi_c$  are involved in exerting force, all the filaments can push against the bead for a spherical anchoring surface. As a result, the average force per single filament in Figs. 3.6c and 3.6d is higher compared to the flat graft surface in Figs. 3.6a and 3.6b.

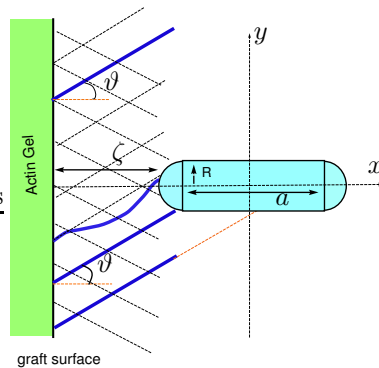


**Figure 3.7** A stiff polymer network in the presence of a rigid cylinder.

### 3.4 A homogeneous actin network and a cylinder

In this section, we consider a bacteria-like object with radius  $R$  and length  $a$  (Fig. 3.7). For those filaments in the network facing the spherical part of the obstacle, one can use the results from section 3.3 with the minor difference that the integration interval must be  $[0, \pi - \vartheta]$  instead of  $[-\vartheta, \pi - \vartheta]$ . This correction doesn't make a big difference in the results.

Now let us focus on the flat side of the obstacle. The entropic force on the circumference of the cylinder has no component in the  $y$  direction since the force exerted by the group of filaments oriented at angle  $\vartheta$  will be cancelled by those at angle  $-\vartheta$ . But what about the component of the force in the  $x$  direction which is parallel to the long axis of the cylinder? As we have mentioned already, the force generated by a fluctuating polymer on a relatively long wall has no component parallel to the wall itself and the total force is perpendicular to it. The reason is that moving the wall parallel to itself doesn't change the number of possible configurations of the filament. This force would have a tangential component if the filament could feel the finite length  $a$  of the cylinder. To make the statement more precise, consider a filament which is fixed at one end in position and orientation and which at the other free end is fluctuating near a rigid wall with finite length  $a$  (Fig. 3.8). Now the question is: how does this tangential force depend on  $a$ ,  $\theta$  and the position of the wall?

We know from the literature (Benetatos and Frey, 2003) that the probability distribution function for a free semiflexible chain in the weakly bend-

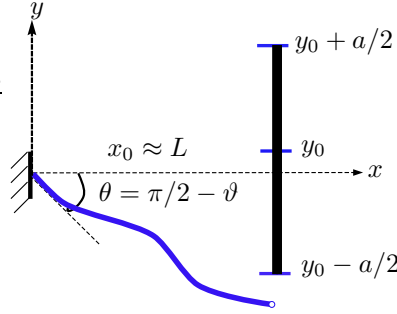


**Figure 3.8** A smooth hard wall with finite length  $a$  constrains the fluctuations of a semiflexible polymer grafted at angle  $\theta$  resulting in an average force on the wall which has both parallel and perpendicular components.

ing limit ( $L \ll \ell_p$ ,  $\theta \ll 1$ ) is given by the following propagator

$$G(y_s, \theta_s, s | y_0, \theta_0, 0) = \frac{\sqrt{3} \ell_p}{2\pi s^2} \exp\left(\frac{-3\ell_p}{s^3} [(y - y_0 - \theta_0 s)^2 - s(y - y_0 - \theta_0 s)(\theta - \theta_0) + \frac{1}{3}s^2(\theta - \theta_0)^2]\right). \quad (3.3)$$

$G(y_s, \theta_s, s | y_0, \theta_0, 0)$  is interpreted as a two point conformational probability distribution, valid only in the weakly bending limit ( $s \ll \ell_p$ ). Now consider a polymer which is grafted at an angle  $\theta$  in one end at  $x = y = 0$  and its free end is fluctuating near a wall barrier with its middle point located at  $x_0 \approx L$  and  $y_0$ . The probability of finding the free end of this polymer within a range of slopes  $-\infty < \theta_L < \infty$  and transverse displacements  $-\infty < y_L < y_0 - a/2$  and  $y_0 + a/2 < y_L < \infty$  is

$$P = \int_{-\infty}^{\infty} d\theta_L \left( \int_{y_0 + \frac{a}{2}}^{\infty} dy_L + \int_{-\infty}^{y_0 - \frac{a}{2}} dy_L \right) G(y_L, \theta_L, L | 0, 0, 0). \quad (3.4)$$

One can integrate over  $\theta_L$  using well-known formulas for Gaussian integrals, and integrate over  $y_L$  using the following integral

$$\int_a^{+\infty} \exp[A(x - B)^2] = \frac{1}{2} \sqrt{-\frac{\pi}{A}} \operatorname{Erfc}[\sqrt{-A}(a - B)]. \quad (3.5)$$

The partition function is proportional to  $P$  with a constant factor. Then

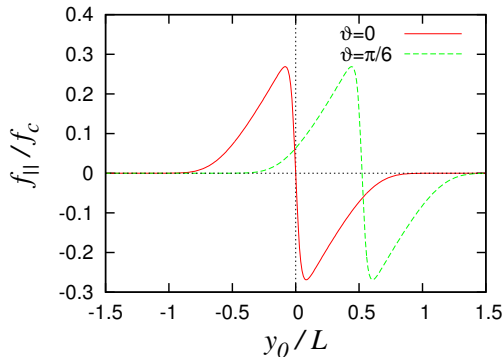


**Figure 3.9** Scaled tangential force exerted by a polymer fluctuating near a wall with finite length  $a/L = 1$ ,  $L = 500$  nm and  $\ell_p = 15$   $\mu$ m (Fig. 3.8).

after scaling all lengths to  $L$  and defining  $\epsilon = L/\ell_p$  we get

$$\begin{aligned}
 Z &= \frac{1}{2} \operatorname{Erfc} \left[ \sqrt{\frac{3}{4\epsilon}} (y_0 + a/2 - \theta L)/L \right] \\
 &+ \frac{1}{2} \left( 1 + \operatorname{Erf} \left[ \sqrt{\frac{3}{4\epsilon}} (y_0 - a/2 - \theta L)/L \right] \right). \quad (3.6)
 \end{aligned}$$

Hence, the repulsive force parallel to the wall is

$$f_{\parallel}/f_c := -\frac{4\epsilon}{\pi^2} \frac{Z'}{Z}, \quad (3.7)$$

where the derivative is with respect to  $y_0$  and  $f_c = \pi^2 \ell_p k_B T / 4L^2$ . Fig. 3.9 displays  $f_{\parallel}$  scaled by the Euler buckling force  $f_c$  as a function of  $y_0$ . As expected,  $f_{\parallel}$  is very sensitive to  $y_0$  and drops down very fast to zero for large values of  $y_0$ .

### 3.5 Summary

We have presented a general formalism to calculate the entropic forces generated by a polymer network on an arbitrarily shaped object. The results depend on the network characteristics (like orientation and length distribution of filaments) and graft surface geometry. Our focus here is

on stiff polymer networks. A polymer is stiff if its contour length is much smaller than its persistence length which is indeed the case for an actin filament with  $\ell_p \approx 15 \mu\text{m}$  and free thermally fluctuating parts of  $100 \sim 200 \text{ nm}$ . Furthermore, we have simplified the network such that it consists of two groups of filaments one, oriented at angle  $\vartheta$  and the other at angle  $-\vartheta$ . This assumption makes the system completely symmetrical in the  $y$ -direction. Moreover, in order to simplify the numerics even more, we have assumed that all the filaments in both groups have the same free fluctuating contour length  $L$ . We have introduced the concept of the graft surface. All the filaments are anchored firmly on this surface which for simplicity is considered to be either flat or spherical. In principle, it is not necessary to consider all the filaments with the same contour length and orientation. But then for a given length and orientation distribution of the network and geometry of the graft surface, one can (at least formally) calculate the total entropic force on the obstacle. The scale for the magnitude of the entropic force is given by the Euler buckling force  $f_c = \pi^2 \ell_p k_B T / 4L^2$ . For a special geometry of the obstacle (sphere and cylinder), the numerical results show that the total entropic force depends on the radius  $R$ , the network orientation  $\vartheta$  as well as graft surface geometry.



# 4 Steric repulsions between two polymers

## 4.1 Introduction

The interaction between biopolymers in the cytoskeleton or membranes in biological systems is characterized by the interplay of energy and entropy. Indeed, lipid bilayers in solution often form stacks or bunches in which several membranes are, on average, parallel to each other. If one ignores thermally excited fluctuations, the membrane or polymer can be regarded as planar sheets or lines which interact as a result of various intermolecular forces. This direct interaction consists of two contributions: “Nonspecific” interactions such as those arising from the van der Waals and electrostatic forces and “specific” interactions mediated by biologically relevant macromolecules. Shape fluctuations give rise to an effective repulsion between the membranes or polymers, which is called “Helfrich repulsion”. Helfrich’s interaction between membranes scales like (Helfrich, 1978)

$$V_{\text{Helf}} = \frac{3\pi^2(k_{\text{B}}T)^2}{128\kappa} \frac{1}{(d - \delta)^2}, \quad (4.1)$$

where  $d$  is the average distance between two membranes,  $\delta$  is the bilayer thickness, and  $\kappa$  is the bending modulus of a single bilayer.

The interplay between this fluctuation-induced repulsion and the direct interaction can lead to continuous *unbinding transitions* from a state where the membranes are bound together to a state where they are completely separated (Lipowsky and Leibler, 1986; Lipowsky, 1988, 1994). The behavior of interacting fluid membranes and their unbinding transitions have been simulated by Lipowsky and Zielinska (1989) using a vectorized Monte Carlo code. They studied the shape fluctuations of a membrane which interacts with another membrane or surface. This interaction has an attractive part which leads to a bound state of the membrane and, thus, to a confinement of its fluctuations. For the linear external potential  $V(z) = Pz$  (Fig. 4.1), MC data showed that the mean separation distance  $\langle z \rangle$  between two membranes scales like  $P^{-1/3}$ , as predicted theoretically by analytical

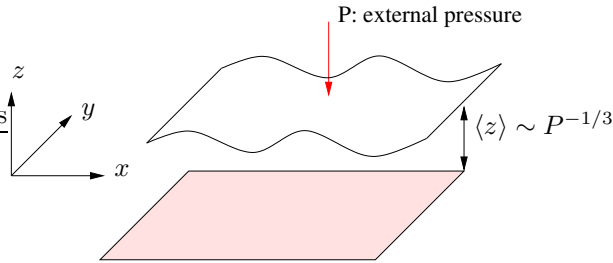


**Figure 4.1** A membrane bounds to a rigid wall at  $\langle z \rangle$  via a linear external potential  $V(z) = Pz$ . Unbinding transition of the membrane happens at  $P = 0$ .

calculations (Lipowsky, 1991; Meunier *et al.*, 1987). Lipowsky (1991) also studied more realistic interactions such as the superposition of hydration and van der Waals forces, and determined critical unbinding transitions for several interaction parameters.

In the above studies, fluctuations of a fluid membrane are restricted by the presence of a rigid wall which is oriented parallel to the membrane. Now let us replace the rigid wall by a rigid rod which is oriented perpendicular to the membrane (see Fig. 4.2). The entropic force exerted by the fluctuating membrane on the polymer rod tip was calculated by Daniels and Turner (2004). This is the situation which one often encounters in

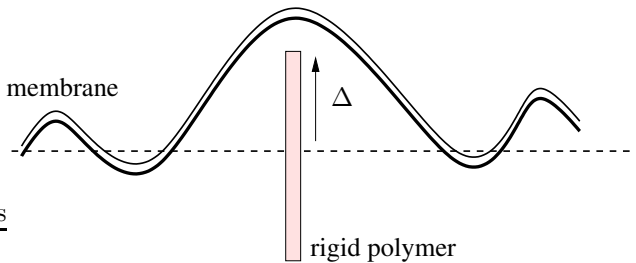


**Figure 4.2** Schematic presentation of a fluctuating membrane interacting with a fiber tip used by Daniels and Turner (2004).  $\Delta$  denotes the height of the rod as measured from the membrane frame at  $z = 0$  (shown as dashed line).

the lamellipodium of a crawling cell. In their analysis, Daniels and Turner (2004) assumed actin filaments to be rigid. They showed that the force

exerted by the membrane on the polymer rod tip is given by

$$f_{\Delta} = 2\sqrt{\frac{A}{\pi}} \frac{\exp(-A\Delta^2)}{\text{Erfc}(\sqrt{A}\Delta)} \quad (4.2)$$

in which  $A = 2\pi\gamma/\ln(1 + \gamma L^2/\kappa\pi^2)$ .  $L \times L$  is the membrane size,  $\kappa$  is the membrane bending rigidity and  $\gamma$  is the surface tension.

In this chapter, our focus is on ‘‘Helfrich repulsion’’ between biopolymers. For example, in the cell cytoskeleton, filaments are highly confined in the fiber network. This confinement increases the free energy of each single fluctuating filament, resulting in an average repulsive force, which is entropic in origin. As is shown in Fig. 4.3, filaments in the network have different orientations with respect to each other. Here, we study entropic repulsion between two filaments fluctuating either i) parallel or ii) perpendicular to each other, using Monte Carlo methods and analytical calculations. The Monte Carlo data give clear evidence for the existence of a repulsive interaction between biopolymers at short distances. We find that the form of the repulsive interaction is in good agreement with the analytical results obtained from scaling arguments.



**Figure 4.3** Microfilaments with fluorescent label in the cell cytoskeleton. The figure is from the website <http://www.biology.arizona.edu/>.

## 4.2 Steric repulsion between two parallel polymers

In this section, the aim is to calculate the repulsive force emerging through steric restrictions in a many polymer system, where the polymers are fluctuating parallel to each other. Similar calculations have been already done in a many membrane system, showing the existence of repulsive forces at

short distances which scale like  $1/d^2$  (Safran, 2003). Here,  $d$  is the average distance between membranes. These calculations can readily be recast in the language of semiflexible polymers, and will be reviewed in this section.

To start, we ask the following question: how does the entropic force between two polymers scale as a function of the average distance between them? To answer this question, in the first step, we do our analytical calculations for stiff filaments. A polymer is stiff if its contour length  $L$  is much smaller than its persistence length  $\ell_p$  ( $L \ll \ell_p$ ). In a next step, we perform Monte Carlo simulations to see the validity range of our analytical results.

Consider a system with polymers whose average positions lie on a one dimensional lattice along the  $\hat{z}$  direction, with lattice spacing  $d$  as shown in Fig. 4.4. A given polymer has an absolute height  $z_n = nd + h_n(x)$ , where  $n$  is an integer which indexes the lattice positions and  $h_n(x)$  is the local deviation of the polymer from its average value,  $\langle z_n \rangle = nd$ . If there are no thermal fluctuations of the polymers, then  $h_n(x) = 0$ . Due to the fluctuations, the polymers collide with each other and lose entropy in these collisions. This can be understood if one considers hardcore repulsions between polymers; the excluded volume of the neighboring polymers limits the configuration of any given polymer, thus reducing its entropy. This implies that the free energy per polymer of a layer of polymers must be greater than that of a single free filament.

We assume that the net result of these collisions is that each polymer experiences an effective interaction with its nearest neighbors which has its lowest energy state, the periodic configuration, where

$$z_{n+1} - z_n = d. \quad (4.3)$$

This interaction is represented as a quadratic form in the deviation of  $(z_{n+1} - z_n) - d$  from zero, or equivalently in  $h_{n+1}(x) - h_n(x)$ . In addition,

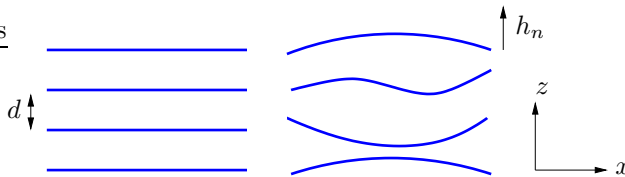


**Figure 4.4** A layer of polymers at an average spacing  $d$  but with randomness  $h_n$  due to thermal fluctuations. Roughness  $h_n$  for  $n$ th polymer is measured from the polymer frame at  $z = nd$ .

there is the bending energy of each polymer. The Hamiltonian,  $\mathcal{H}$ , is thus written as

$$\mathcal{H} = \int dx u(x), \quad (4.4)$$

$$u = \frac{1}{2}B \sum_n (h_n - h_{n+1})^2 + \frac{1}{2}\kappa \sum_n (\nabla^2 h_n)^2. \quad (4.5)$$

Here  $\kappa$  is the bending rigidity of the polymer (with dimension energy  $\times$  length), and  $\frac{1}{2}(\nabla^2 h_n)$  is the mean curvature of the  $n$ th polymer. This expression is correct for polymers with gentle undulations ( $\nabla h \ll 1$ ); otherwise the simple expressions for the curvature are incorrect and the length constraints must be reconsidered as well. The compressional elastic constant,  $B$ , represents an effective repulsion between the membranes and will be computed self-consistently. Note that this Hamiltonian is unchanged if the positions of all the polymers are uniformly shifted, representing a trivial translation of the system. After Fourier transforming in both the  $\hat{z}$  direction (Fourier wave number  $q_z$  with an upper cutoff  $\pi/d$  due to the periodicity) and the  $x$  plane (Fourier wave number  $q_x$ ) we have

$$\mathcal{H} = \sum_{q_x, q_z} |h(q_x, q_z)|^2 \left[ B (1 - \cos(q_z d)) + \frac{1}{2}\kappa q_x^4 \right] = \sum_{q_x, q_z} H(q_x, q_z). \quad (4.6)$$

At temperature  $T$ ,  $e^{-H(q_x, q_z)/k_B T}$  is a measure of the probability that a mode with wave numbers  $q_x$  and  $q_z$  will be excited. Indeed, this probability is a Gaussian function of  $h(q_x, q_z)$  and as we will see, this makes the calculations quite straightforward.

### 4.2.1 Free energy of undulations and the repulsive interaction

As we mentioned, the Boltzmann factor corresponding to the Hamiltonian of Eq. (4.6) is a Gaussian, so the free energy  $\mathcal{F}$  is easily evaluated from

$$\mathcal{F} = -k_B T \ln \left[ \prod_{q_x, q_z} \int dh(q_x, q_z) e^{-\mathcal{H}/k_B T} \right]. \quad (4.7)$$

Performing the integral, we find that the difference in free energy per unit length,  $\Delta\mathcal{F}_l$ , between the many polymer system and that of a single polymer (where  $d \rightarrow \infty$  and we anticipate that  $B \rightarrow 0$ ) is given by

$$\Delta\mathcal{F}_l = \frac{k_B T}{2(2\pi)^2} \int dq_x dq_z \ln \left[ \frac{B(q_z) + \kappa q_x^4}{\kappa q_x^4} \right], \quad (4.8)$$

where  $B(q_z) = 2B(1 - \cos q_z d)$ . Integrating first over  $q_x$  with the upper cutoff set to  $\infty$ , we find

$$\Delta\mathcal{F}_l = \frac{k_B T}{2^{5/4}\pi} \left(\frac{B}{\kappa}\right)^{1/4} \int_{-\pi/d}^{\pi/d} dq_z \sqrt[4]{(1 - \cos q_z d)}. \quad (4.9)$$

This integral can be written as

$$\Delta\mathcal{F}_l = 0.763 \frac{k_B T}{d} \left(\frac{B}{\kappa}\right)^{1/4}. \quad (4.10)$$

Now, the modulus  $B$  is related to the second derivatives of the free energy with respect to the average layer spacing; i.e, imagine a uniform expansion or compression of the system. The restoring force is just the effective value of  $B$  which is proportional to the macroscopic compressibility of the system. Thus, we may obtain a self-consistent equation to determine  $B$  from

$$B = d \frac{\partial^2 \Delta\mathcal{F}_l}{\partial d^2}. \quad (4.11)$$

Using Eq. (4.11) in Eq.( 4.10), we find that

$$B = 5.09 k_B T \left(\frac{k_B T}{\kappa}\right)^{1/3} d^{-8/3}, \quad (4.12)$$

and the free energy difference per unit length,  $\Delta\mathcal{F}_l$ , is

$$\Delta\mathcal{F}_l = 1.146 k_B T \left(\frac{k_B T}{\kappa}\right)^{1/3} d^{-2/3}, \quad (4.13)$$

representing an effective repulsion that decays algebraically as  $d$  is increased. This long-range, entropic repulsion is present in all multipolymer and multimembrane systems. In addition to this repulsion, the specific Coulomb repulsions due to charge effects and/or attractions due to Van der Waals interactions may result in an effective attractive well that binds two polymers or membranes at a particular distance.

For membranes, the Hamiltonian in Eq. 4.6 changes to (Safran, 2003)

$$\mathcal{H} = \sum_{\mathbf{q}, q_z} |h(\mathbf{q}, q_z)|^2 \left[ B(1 - \cos(q_z d)) + \frac{1}{2} \kappa \mathbf{q}^4 \right] = \sum_{\vec{q}_x, q_z} H(\mathbf{q}, q_z), \quad (4.14)$$

in which  $\mathbf{q} = (q_x, q_y)$  is the Fourier wavevector in the  $x - y$  plane (see Fig. 4.1). Similar to Eq. 4.8, the difference in free energy per unit area for the membranes reads

$$\Delta\mathcal{F}_a = \frac{k_B T}{2(2\pi)^3} \int dq_x dq_y dq_z \ln \left[ \frac{B(q_z) + \kappa \mathbf{q}^4}{\kappa \mathbf{q}^4} \right], \quad (4.15)$$

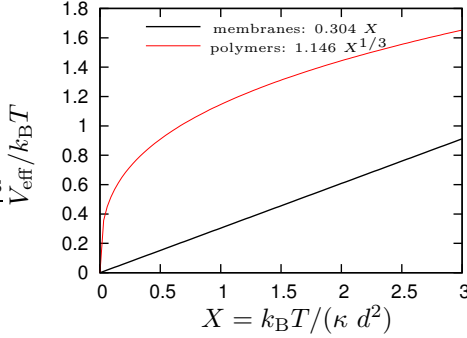


**Figure 4.5** Effective steric potential  $V_{\text{eff}}/k_{\text{B}}T$  shows different scaling behaviour for polymers and membranes. It scales as  $X$  for membranes but as  $X^{1/3}$  for polymers.

Here  $\kappa$  is the bending modulus of the membranes, which has dimension of energy.

Carrying out the integral in Eq. 4.15 and following a procedure similar to that for polymers, we arrive at our final expressions for  $B$  and  $\Delta\mathcal{F}_a$

$$\begin{aligned} B &= 3.647 k_{\text{B}}T \left( \frac{k_{\text{B}}T}{\kappa} \right) d^{-4}, \\ \Delta\mathcal{F}_a &= 0.304 k_{\text{B}}T \left( \frac{k_{\text{B}}T}{\kappa} \right) d^{-2}. \end{aligned} \quad (4.16)$$

See Fig. 4.5 for a plot of (dimensionless) effective steric potential  $V_{\text{eff}}/k_{\text{B}}T$  between two polymers or membranes as a function of variable  $X = k_{\text{B}}T/\kappa d^2$ .  $V_{\text{eff}}$  scales as  $X$  for membranes but as  $X^{1/3}$  for polymers. Note that  $X$  has the dimension of length<sup>-2</sup> for membranes but length<sup>-3</sup> for polymers.

The important conclusion here is that the effective steric repulsive potential  $V_{\text{eff}}$ , between two polymers or membranes can be written in the general form

$$V_{\text{eff}}/k_{\text{B}}T \sim C \left( \frac{k_{\text{B}}T}{\kappa} \right)^{(2D-3)/3} d^{-(4D-6)/3} \quad (4.17)$$

in which  $C \sim 1.146$ ,  $D = 2$  for polymers, and  $C \sim 0.304$ ,  $D = 3$  for membranes.

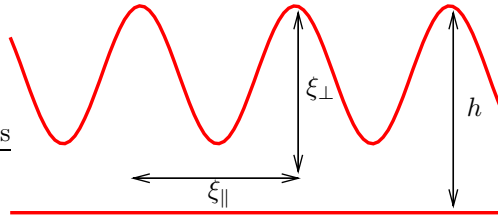


**Figure 4.6** A polymer fluctuating near a rigid line.  $\xi_{\perp}$  is the roughness and  $\xi_{\parallel}$  is the parallel correlation length.  $h$  is the average distance between the polymer and the wall.

### 4.2.2 Scaling arguments

Analytical calculations in Sec. 4.2.1 show that steric repulsion between two polymers or membranes scales like  $d^{-m_c}$ , in which  $m_c$  is equal to 2 for membranes and  $2/3$  for stiff polymers. It is possible to get the power  $m_c$  from scaling arguments. Of course, this scaling argument doesn't give any information about the constant prefactor. Similar scaling arguments have already been given for membranes (Lipowsky and Zielinska, 1989). Here, we adopt those for stiff polymers.

We start with two parallel polymers undergoing thermal fluctuations in two dimensions (2d). For simplicity we assume that one of the polymers is a rigid line, such that we actually have a fluctuating polymer near a rigid line (see Fig. 4.6). The free energy of the polymer is

$$\mathcal{F} = \frac{\kappa}{2} \int_0^L (\nabla^2 h)^2 ds, \quad (4.18)$$

where  $h$  is the average height of the polymer measured with respect to the rigid wall.

Since typical energies are of the order of the thermal energy scale  $k_B T$ , we may estimate from Eq. 4.18

$$k_B T \sim \kappa \left( \frac{\xi_{\perp}}{\xi_{\parallel}^2} \right)^2 \xi_{\parallel}, \quad (4.19)$$

where  $\xi_{\perp}$  is the typical height of the fluctuations and  $\xi_{\parallel}$  is the respective parallel correlation length. Thus

$$\xi_{\perp} \sim \left( \frac{k_{\text{B}}T}{\kappa} \right)^{1/2} \xi_{\parallel}^{3/2}. \quad (4.20)$$

For a fluctuating polymer near a wall,  $\xi_{\perp}$  is of the order of the average distance between the polymer and the rigid wall:

$$\xi_{\perp} \sim \langle h \rangle. \quad (4.21)$$

Therefore, the free energy per unit length scales as

$$\Delta\mathcal{F}_l \sim k_{\text{B}}T \left( \frac{k_{\text{B}}T}{\kappa} \right)^{1/3} \xi_{\perp}^{-2/3}, \quad (4.22)$$

or from Eq. (4.21)

$$\Delta\mathcal{F}_l \sim k_{\text{B}}T \left( \frac{k_{\text{B}}T}{\kappa} \right)^{1/3} \langle h \rangle^{-2/3}. \quad (4.23)$$

Hence, we expect to have a steric repulsion force between the polymer and the rigid wall which scales as  $\langle h \rangle^{-5/3}$ , since steric potential scales as  $\langle h \rangle^{-2/3}$ .

In the Monte Carlo simulations, we apply an external constant pressure  $P$  to the polymer to bring the polymer close to the wall. Now the question arises, how does  $\langle h \rangle$  scales as a function of external pressure  $P$ ? In the presence of an external pressure, the free energy per unit length reads

$$\Delta\mathcal{F}_l \sim k_{\text{B}}T \left( \frac{k_{\text{B}}T}{\kappa} \right)^{1/3} \langle h \rangle^{-2/3} + P\langle h \rangle. \quad (4.24)$$

The equilibrium distance is found from  $\partial\Delta\mathcal{F}_l/\partial\langle h \rangle = 0$  as

$$-\frac{2}{3}k_{\text{B}}T \left( \frac{k_{\text{B}}T}{\kappa} \right)^{1/3} \langle h \rangle^{-5/3} + P = 0, \quad (4.25)$$

$$\langle h \rangle \sim P^{-3/5}. \quad (4.26)$$

Similarly, for a fluctuating membrane, Eq. 4.19 changes to

$$k_{\text{B}}T \sim \kappa \left( \frac{\xi_{\perp}}{\xi_{\parallel}^2} \right)^2 \xi_{\parallel}^2, \quad \text{or} \quad \xi_{\parallel} \sim \xi_{\perp} \left( \frac{\kappa}{k_{\text{B}}T} \right)^{1/2}. \quad (4.27)$$

Thus, the free energy per unit area reads as

$$\Delta\mathcal{F}_a \sim k_B T \left( \frac{k_B T}{\kappa} \right) \xi_{\perp}^{-2}, \quad \text{or} \quad \Delta\mathcal{F}_a \sim k_B T \left( \frac{k_B T}{\kappa} \right) \langle h \rangle^{-2}. \quad (4.28)$$

In the presence of an external pressure which pushes the membrane close to a rigid wall (see Fig. 4.1), the free energy per unit area is

$$\Delta\mathcal{F}_a \sim k_B T \left( \frac{k_B T}{\kappa} \right) \langle h \rangle^{-2} + P \langle h \rangle, \quad (4.29)$$

and the equilibrium distance is found by  $\partial\Delta\mathcal{F}_a/\partial\langle h \rangle = 0$  to be

$$\langle h \rangle \sim P^{-1/3}. \quad (4.30)$$

In summary, the length scales  $\langle h \rangle$  and  $\xi_{\perp}$  show algebraic behavior  $\langle h \rangle \sim \xi_{\perp} \sim P^{-\eta_c}$ , in which  $\eta_c = 3/5$  for polymers and  $\eta_c = 1/3$  for membranes. For polymers, the parallel correlation length  $\xi_{\parallel}$  scales as  $P^{-2\eta_c/3}$  but for membranes as  $P^{-\eta_c}$ .

### 4.2.3 Monte Carlo simulations

To investigate the validity range of our analytical calculations, we did some Monte Carlo simulations. Monte Carlo simulations have been performed in the presence of a constant external pressure  $P$ , which pushes the polymer close to the wall (see Fig. 4.7). This external pressure leads to a bound state of the polymer and, thus, to a confinement of its fluctuations.

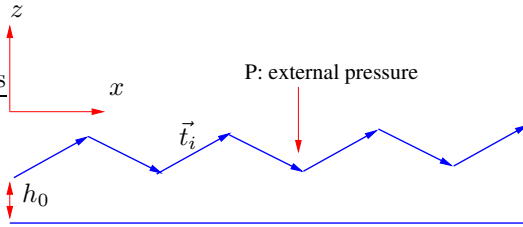


**Figure 4.7** A polymer fluctuating near a wall in presence of an external pressure. The polymer is represented by  $N$  segments  $\vec{t}_i$ , whose direction is tangent to the polymer contour length  $L$ .

The Hamiltonian of such a system from Eq. 1.4 reads

$$\frac{\mathcal{H}}{k_B T} = -\frac{\lambda}{k_B T} \sum_{i=1}^N \vec{t}_i \cdot \vec{t}_{i+1} + \frac{P}{k_B T} \sum_{i=1}^N (N+1-i)(\vec{t}_i)_z + \frac{P}{T} N h_0, \quad (4.31)$$

where  $h_0$  is the height of one end of the polymer.

Now, we define the dimensionless quantities  $\hat{z}_i = \vec{t}_i/a$  and  $z_0 = h_0/a$ . Then

$$\frac{\mathcal{H}}{k_B T} = -R \sum_{i=1}^N \hat{z}_i \cdot \hat{z}_{i+1} + p \sum_{i=1}^N (N+1-i)(\hat{z}_i)_z + pNz_0, \quad (4.32)$$

where  $R = \lambda a^2/k_B T = \ell_p/a$  and  $p = aP/k_B T$ . Indeed,  $R/N = \ell_p/L$  is a measure of the filament's stiffness. A filament is stiff if  $R/N \gg 1$  and is flexible if  $R/N \ll 1$ . For  $R \sim N$ , our filament is termed semiflexible.

Fig. 4.8a shows Monte Carlo results for the  $\langle z \rangle$  and  $\xi_\perp = (\langle z^2 \rangle - \langle z \rangle^2)^{1/2}$  as a function of  $p$  where  $N = 100$ ,  $R = \ell_p/a = 100$  (semiflexible polymer). The figure shows that  $\xi_\perp \sim \langle z \rangle \sim p^{-3/5}$  which is in agreement with Eq. (4.26) and Eq. (4.21). Monte Carlo simulations have been repeated for

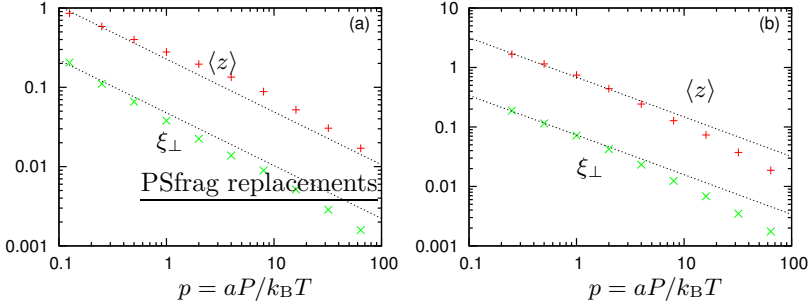


**Figure 4.8** The Monte Carlo results for the  $\langle z \rangle$  and  $\xi_\perp$  as a function of  $p$  with (a)  $\ell_p/L = 1$  and (b)  $\ell_p/L = 0.01$  ( $N=100$ ). The straight lines have slope  $-3/5$ .

a flexible polymer with  $\ell_p/L = 0.01$ , as well. The results show the same scaling behavior for both  $\langle z \rangle$  and  $\xi_\perp$ . (See Fig. 4.8b). At high pressures ( $p > 10$ ), Monte Carlo data start to deviate from scaling curves. These deviations might be due to the fact that for high external pressures, filaments undulations are not small any more and the assumption  $\nabla h \ll 1$  breaks down. This means that one needs to take higher order terms into account.

Similar Monte Carlo simulations on membranes by Lipowsky and Zielinska (1989) showed that, in the presence of a linear external pressure, all three length scales  $\langle z \rangle$ ,  $\xi_\parallel$  and  $\xi_\perp$  scale as  $p^{-1/3}$  (Fig. 4.9). This scaling behaviour was predicted theoretically in Eqs. 4.27, 4.30. Their MC data also deviates from scaling lines for pressures  $p > 1$ . This show that the scaling arguments breakdown for large pressures, in which membranes undulations might not be small any more.

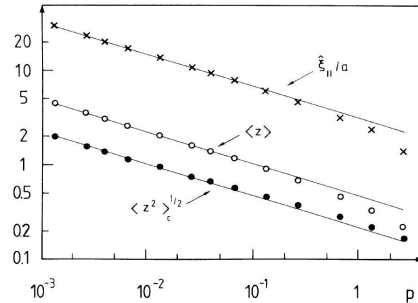


**Figure 4.9** The results of Monte Carlo simulation on membranes, taken from the paper by Lipowsky and Zielinska (1989). The straight lines have slope  $-1/3$  showing the same scaling behaviour for all three length scales  $\langle z \rangle$ ,  $\xi_{\parallel}$  and  $\xi_{\perp}$ . Here,  $p = a^3 P / (k_B T \kappa)^{1/2}$  in which  $a$  is the lattice constant,  $P$  is the external pressure and  $\kappa$  is the membranes' bending modulus.

#### 4.2.4 Probing steric repulsion between two parallel polymers by MC simulations

In the presence of an external pressure, the polymer binds to the wall at an average distance  $\langle z \rangle$ . Indeed, at  $p = 0$  the polymers unbind from each other and  $\langle z \rangle \rightarrow \infty$ . The fluctuations around  $\langle z \rangle$ , which we record from our Monte Carlo simulations, give information about the effective potential between the polymer and the wall. We expect an effective potential of a form like  $V(z)/k_B T = \alpha z^{-2/3} + \beta z + \gamma$ , in which  $\alpha$ ,  $\beta$  and  $\gamma$  are fitting parameters. The first term is the Helfrich repulsion term, the second one is the external linear potential and the last term is just a constant. We will fit this potential to our MC data to get values of  $\alpha$ ,  $\beta$  and  $\gamma$ .

Fig. 4.10a shows the effective potential between two flexible polymers in the presence of different external pressures ( $\ell_p/L = 0.01$ ,  $N = 100$ ). Obviously, there is an effective repulsion near the wall which scales as  $\langle z \rangle^{-2/3}$ . This is in agreement with Eq. (4.23). This long-range entropic repulsion together with the attractive external pressure result in an effective well that binds the polymer at a particular distance. As we increase  $p$ , the polymer binds to the wall at a closer distance (Fig. 4.10c). Coefficients  $\alpha$ ,  $\beta$  and  $\gamma$  are collected in Table 4.1. As expected  $\beta$  increases with external pressure  $p$ . The coefficient  $\alpha$  which we expect to be dependent on  $L/\ell_p$  but independent of external pressure, shows dependency on  $p$ : it first increases and then decreases. However, as one can see from Fig. 4.11a, in the range

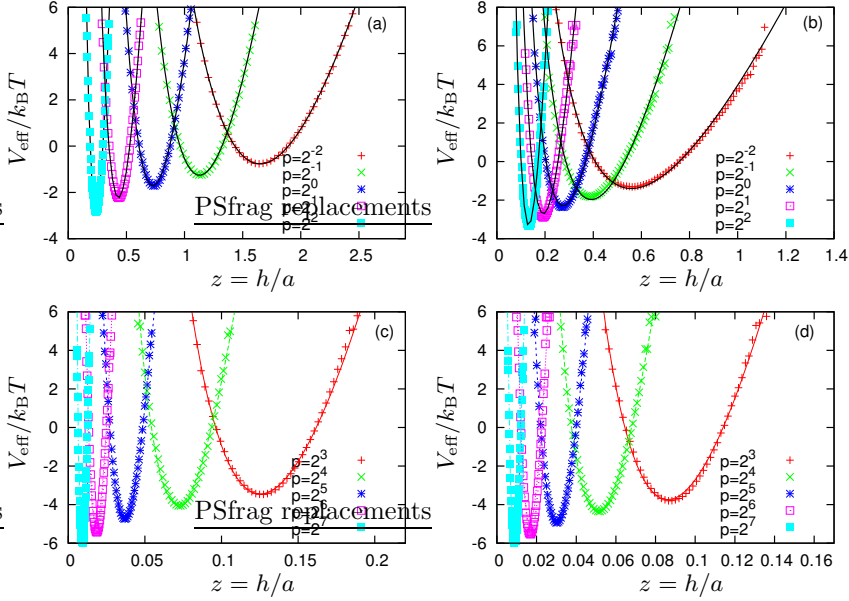


**Figure 4.10**  $V_{\text{eff}}/k_{\text{B}}T$  of (a), (c) a flexible polymer with  $\ell_{\text{p}}/L = 0.01$  and (b), (d) a semiflexible with  $\ell_{\text{p}}/L = 1$  for different values of external pressure  $p = aP/k_{\text{B}}T$  ( $N = 100$ ). The solid lines are the scaling functions of the form  $V(z)/k_{\text{B}}T = \alpha z^{-2/3} + \beta z + \gamma$ , in which  $\alpha$ ,  $\beta$  and  $\gamma$  are the fitting parameters, presented in Table 4.1 and 4.2.

of  $0.125 \leq p \leq 128$  that  $\beta$  changes 3 order of magnitude, both  $\alpha$  and  $\gamma$  don't change significantly.

MC simulations also have been done for a semiflexible polymer with  $\ell_{\text{p}}/L = 1$  ( $R = \ell_{\text{p}}/a = 100, N = 100$ ). Fig. 4.10b,d shows  $V_{\text{eff}}$  in this regime. Comparison of  $V_{\text{eff}}$  for a flexible polymer with a semiflexible polymer shows that flexible polymer feels a higher repulsion due to more thermal fluctuations, so binds to the wall at higher distances compare to a semiflexible polymer. Coefficients  $\alpha$ ,  $\beta$  and  $\gamma$  are collected in Table 4.2. Again,  $\beta$  increases with pressure but,  $\alpha$  first increases and then decreases with external pressure  $p$ .

**Table 4.1** Coefficients of effective potential  $V_{\text{eff}}$  for  $\ell_p/L = 0.01$ .

$p$	$\alpha$	$\beta$	$\gamma$	$p$	$\alpha$	$\beta$	$\gamma$
$2^{-3}$	91.5529	14.5783	-86.2964	$2^{-2}$	99.056	28.699	-119.058
$2^{-1}$	96.362	52.496	-149.403	$2^0$	76.669	86.4875	-159.416
$2^1$	53.642	145.357	-158.901	$2^2$	35.536	260.600	-157.359
$2^3$	22.8439	485.778	-155.534	$2^4$	16.8329	911.355	-166.876
$2^5$	10.3079	1732.27	-161.515	$2^6$	6.43172	3410.55	-160.281
$2^7$	3.97222	6786.83	-158.87				

**Table 4.2** Coefficients of effective potential  $V_{\text{eff}}$  for  $\ell_p/L = 1$ .

$p$	$\alpha$	$\beta$	$\gamma$	$p$	$\alpha$	$\beta$	$\gamma$
$2^{-3}$	13.49	12.5741	-26.35	$2^{-2}$	17.756	31.228	-45.021
$2^{-1}$	19.791	62.909	-63.582	$2^0$	20.106	114.911	-81.442
$2^1$	21.062	217.964	-107.847	$2^2$	21.282	416.415	-140.381
$2^3$	16.1365	639.529	-141.548	$2^4$	12.2864	1175.82	-153.643
$2^5$	9.27367	2163.43	-165.733	$2^6$	5.92352	3688.52	-157.258
$2^7$	3.81547	6922.6	-156.207				

### 4.3 Steric repulsion between two perpendicular polymers

In cross-linked polymer networks, like the cytoskeleton, filaments are highly entangled. Here, we focus on the case that two filaments are entangled perpendicular to each other. One or both ends of the filaments might be firmly anchored inside the fiber network, and so we can have different boundary conditions. Again, the aim is to calculate the Helfrich repulsion force for different boundary conditions.

To start, consider two polymers embedded in three dimensional space (3d). For simplicity, we assume that one of the polymers is rigid and the other polymer is fluctuating perpendicular to it. Now the question is how does the entropic repulsion between these two polymers scale as a function of minimal distance? One can map this problem to 2d in which a polymer is fluctuating in 2d near a point barrier (Fig. 4.12b). The next subsection is a collection of our calculations in 2d, using two different methods: i) propagator method and ii) path integral method which is similar to the work by Daniels and Turner (2004) on membranes.

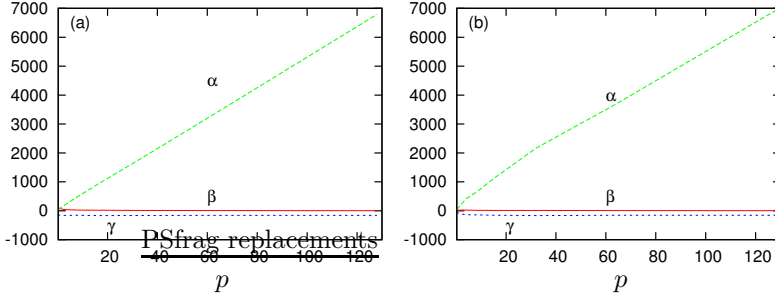


**Figure 4.11**  $\alpha$ ,  $\beta$  and  $\gamma$  as a function of external pressure for (a)  $\ell_p/L = 0.01$  and (b)  $\ell_p/L = 1$ . In both cases, at the range of  $p$  in which  $\beta$  increases strongly with external pressure, the coefficients  $\alpha$  and  $\gamma$  don't change significantly.

### 4.3.1 Analytical calculations

#### Propagator Method

One intuitive way of looking at the problem is to “count” the number of possible configurations of the filament in the presence of the barrier. Obviously, compared to a free fluctuating filament, this number is reduced. This number is a measure of the probability to find the filament above the barrier. We know already from the literature that the probability distribution function for a free semiflexible chain in the weakly bending limit ( $L \ll \ell_p$ ,  $\theta \ll 1$ ) is given by the following propagator (Benetatos and Frey, 2003)

$$G(y_s, \theta_s, s | y_0, \theta_0, s = 0) = \frac{\sqrt{3} \ell_p}{2\pi s^2} \exp \left( \frac{-3\ell_p}{s^3} \left[ (y - y_0 - \theta_0 s)^2 - s(y - y_0 - \theta_0 s)(\theta - \theta_0) + \frac{1}{3} s^2 (\theta - \theta_0)^2 \right] \right). \quad (4.33)$$

Here,  $(\theta_0, y_0)$  and  $(\theta_s, y_s)$  are the orientation and transversal position of the polymer at contour lengths 0 and  $s$ , respectively. For fixed  $y_0 = \theta_0 = 0$ , the probability of finding the free end of the polymer within a very small range of slopes and transverse displacements ( $-\Delta\theta < \theta_L < \Delta\theta$  and  $-\Delta y < y_L < \Delta y$ ) is

$$P(\Delta\theta, \Delta y) = \int_{-\Delta\theta}^{\Delta\theta} d\theta_L \int_{-\Delta y}^{\Delta y} dy_L G(y_L, \theta_L, L | 0, 0, 0), \quad (4.34)$$

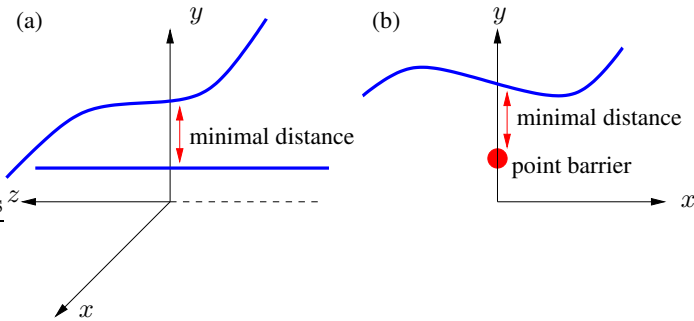


**Figure 4.12** (a) A polymer fluctuating perpendicular to a rigid polymer in  $3d$ . It is possible to map this problem to  $2d$  in which a polymer is fluctuating in the presence of a point barrier (b).

in which  $G(y_L, \theta_L, L|0, 0, 0)$  is interpreted as a two point conformational probability density, valid only in the weakly bending limit ( $L \ll \ell_p$ ).

To start, we consider a polymer which is clamped at one end at  $y = d$  and is fluctuating near a point barrier located at  $y = h_0$ . The other end of the polymer is hinged at  $x \sim L$ , but is free to slide in the  $y$  direction and choose different orientations (Fig. 4.13).

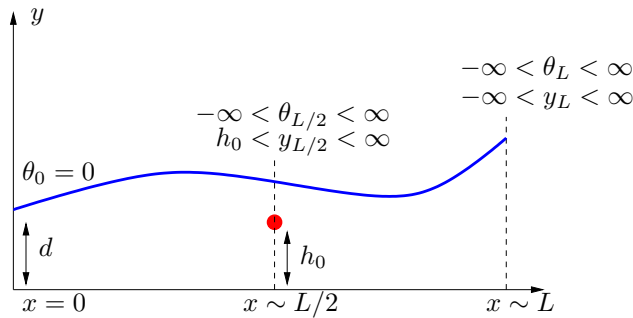


**Figure 4.13** A polymer fluctuating near a point barrier. One end of the filament is clamped at  $x = 0$ ,  $y = d$  and has a fixed orientation  $\theta_0 = 0$ . The other end is hinged at  $x \sim L$  such that it can slip in the  $y$  direction and change orientation as well. We call this case clamped-hinged (slip  $y$ ).

The probability of finding the free end of this polymer within a range of

slopes  $-\infty < \theta_L < \infty$  and transverse displacements  $-\infty < y_L < \infty$  is

$$P = \int_{-\infty}^{\infty} d\theta_L \int_{-\infty}^{\infty} d\theta_{L/2} \int_{h_0}^{\infty} dy_{L/2} \int_{-\infty}^{\infty} dy_L \times \\ G(y_L, \theta_L, L|y_{L/2}, \theta_{L/2}, \frac{L}{2}) \times G(y_{L/2}, \theta_{L/2}, \frac{L}{2}|d, 0, 0). \quad (4.35)$$

By using Eq. (4.33)

$$P = \frac{12\ell_p^2}{\pi^2 L^4} \int_{-\infty}^{\infty} d\theta_L \int_{-\infty}^{\infty} d\theta_{L/2} \int_{h_0}^{\infty} dy_{L/2} \int_{-\infty}^{\infty} dy_L \\ \times \exp\left(-\frac{24\ell_p}{L^3} \left[ (y_{L/2} - d)^2 - \frac{L}{2}(y_{L/2} - d)(\theta_{L/2}) + \frac{L^2}{12}\theta_{L/2}^2 \right]\right) \\ \times \exp\left(-\frac{24\ell_p}{L^3} \left[ (y_L - y_{L/2} - \theta_{L/2}\frac{L}{2})^2 - \frac{L}{2}(y_L - y_{L/2} - \theta_{L/2}\frac{L}{2}) \right. \right. \\ \left. \left. \times (\theta_L - \theta_{L/2}) + \frac{L^2}{12}(\theta_L - \theta_{L/2})^2 \right]\right). \quad (4.36)$$

One can integrate over  $\theta_L, \theta_{L/2}$  and  $y_L$  using the well-known Gaussian integral

$$\int_{-\infty}^{+\infty} \exp[A(x - \alpha) + B(x - \alpha)^2] = \sqrt{-\frac{\pi}{B}} \exp(-A^2/4B), \quad (4.37)$$

and integrate over  $y_{L/2}$  using the following integral

$$\int_a^{+\infty} \exp[A(x - B)^2] = \frac{1}{2} \sqrt{-\frac{\pi}{A}} \operatorname{Erfc}[\sqrt{-A}(a - B)]. \quad (4.38)$$

Then, we end up with our final expression for  $P$

$$P = \frac{1}{2} \operatorname{Erfc} \left[ \left( \frac{6\ell_p}{L} \right)^{1/2} (h_0 - d)/L \right]. \quad (4.39)$$

The partition function  $\mathcal{Z}$  is proportional to  $P$  with a constant factor. As a result we have (Fig. 4.14a)

$$\mathcal{Z} \sim \frac{1}{2} \operatorname{Erfc} \left[ \left( \frac{6\ell_p}{L} \right)^{1/2} (h_0 - d)/L \right]. \quad (4.40)$$

Then the effective repulsion between the polymer and barrier is given by

$$V_{\text{eff}}/k_B T \sim -\ln \left( \frac{1}{2} \operatorname{Erfc} \left[ \left( \frac{6\ell_p}{L} \right)^{1/2} (h_0 - d)/L \right] \right) = -\ln \left( \frac{1}{2} \operatorname{Erfc}[\sqrt{C} X] \right), \quad (4.41)$$

in which  $C = 6\ell_p/L$  and  $X = (h_0 - d)/L$ .

Now we are in a position to calculate the force between the polymer and barrier as follows

$$f_s = \frac{fL}{k_B T} = \frac{\partial V_{\text{eff}}}{\partial X} \sim 2\sqrt{\frac{C \exp(-CX^2)}{\pi \operatorname{Erfc}[\sqrt{C} X]}}. \quad (4.42)$$

The (dimensionless) force  $f' = f_s/(2\sqrt{C/\pi})$ , as given by Eq. 4.42, is plotted in Fig. 4.14b as a function of  $\sqrt{C}X$  and has the following limits

$$\begin{aligned} f' &\rightarrow \sqrt{\pi}(\sqrt{C}X) & \text{as } X &\rightarrow \infty, \\ f' &\rightarrow 1 + \frac{2}{\sqrt{\pi}}(\sqrt{C}X) & \text{as } X &\rightarrow 0, \\ f' &\rightarrow \frac{1}{2} \exp(-CX^2) & \text{as } X &\rightarrow -\infty. \end{aligned} \quad (4.43)$$

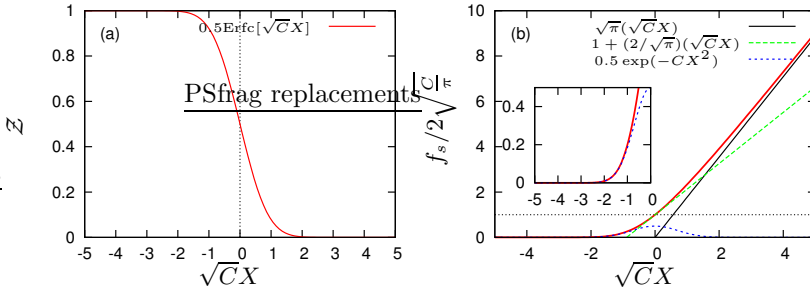


**Figure 4.14** (a) Partition function  $\mathcal{Z}$  and (b) dimensionless force (red curve) as well as its three limits from Eq. 4.43, are plotted as a function of  $\sqrt{C}X$ . For large positive  $X$  and also for small  $X$ , the force on the polymer becomes linear with spring constants  $2C$  (black line) and  $4C/\pi$  (green line), respectively. For large negative  $X$ , the force decays exponentially (blue curve).

From these limits and Fig. 4.14b, we can understand the following behavior for our polymer-point barrier system. For large, positive  $X$  (when the barrier strongly limits the polymer's thermal fluctuations) the force on the polymer becomes linear with a spring constant  $\approx 2C$ . For small  $X$ , the force is again linear (with a spring constant  $4C/\pi$ ), but does not vanish at  $h_0 = d$ . Rather, it approaches the constant value  $2\sqrt{\frac{C}{\pi}}$ . Finally, when the point barrier is far from the polymer, the force decays rapidly to zero, as one would expect.

We can also use the partition function  $\mathcal{Z}$  to calculate the average distance  $\langle X \rangle$  between the polymer and the point barrier.  $\langle X \rangle$  is given by

$$\langle X \rangle = \frac{\int_X^\infty dx x \mathcal{Z}}{\int_X^\infty dx \mathcal{Z}}. \quad (4.44)$$

Calculating the integral in Eq. 4.44, we get the following expression for the average  $\langle X \rangle$

$$\langle X \rangle = \sqrt{\frac{1}{\pi C}} \frac{\exp(-CX^2)}{\operatorname{Erfc}(\sqrt{CX})}. \quad (4.45)$$

By combining Eq. 4.45 with Eq. 4.42, we get

$$f_s = 2C\langle X \rangle, \quad (4.46)$$

which has the simple linear form with spring constant  $2C$ .

In order to get an idea about the order of magnitude of the repulsive force, we plug in the following set of parameters:  $\ell_p = 15 \mu\text{m}$ ,  $L = 500 \text{ nm}$ ,  $d = 0$ ,  $h_0 = L/3$  and  $k_B T = 4.1 \text{ pN nm}$  to get  $f \sim 4 \text{ pN}$ . By increasing  $h_0$  to the value  $L/2$ , the force increases roughly to  $6 \text{ pN}$  and by choosing  $h_0 = L$ , we get  $f \sim 12 \text{ pN}$ .

For completeness, we performed Monte Carlo simulations for different values of  $\epsilon = L/\ell_p$ , in order to find out the validity range of our analytical calculations. There is a nice agreement between MC data and analytical results for  $\epsilon \leq 0.1$  (stiff filaments). For  $X > 0.2$ , MC data deviates significantly from analytical results as  $\epsilon$  increases (see Fig. 4.15).

Finally, we would like to mention that one can repeat the calculations for different boundary conditions of polymer. For example, one can clamp or hinge one or both ends. The only difference in the final results would appear in the constant number  $C$  which is summarized for different boundary conditions in Table 4.3.

**Table 4.3** Coefficient  $C$  for different boundary conditions.

boundary conditions	$C$
clamped-clamped (slip y)	$24\ell_p/L$
clamped-hinged (slip y)	$6\ell_p/L$
hinged-clamped (slip y)	$3\ell_p/2L$

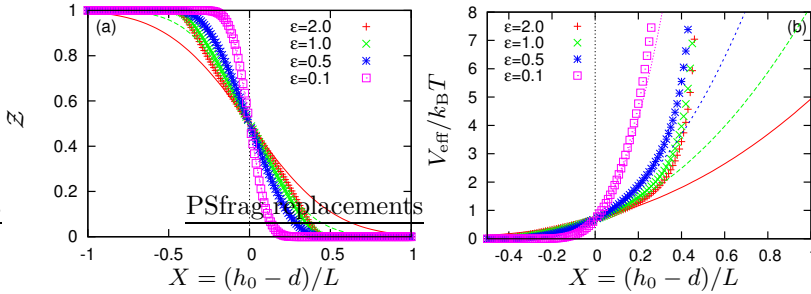


**Figure 4.15** MC simulations (data points) in comparison to analytical results (lines) for (a) partition function and (b) effective steric potential. As expected, MC data deviates from analytical results for flexible and semiflexible polymers (values of  $\epsilon = L/\ell_p > 0.1$ ) and is in good agreement for stiff filaments (values of  $\epsilon = L/\ell_p \leq 0.1$ ).

### Path Integral Method

In this part, we use the same method as described by Daniels and Turner (2004) to calculate the entropic force. Consider a stiff polymer with contour length  $L$  and persistence length  $\ell_p$ , where one of its end is fixed at  $(x = 0, y = d)$  and crosses the barrier at  $(x \sim L/2, y)$ . The other end is hinged at  $x \sim L$  such that it can slip in the  $y$  direction and choose different orientations. Since the polymer is stiff, we parameterize the position  $\mathbf{R}$  of our polymer as  $\mathbf{R} = x\hat{\mathbf{i}} + h(x)\hat{\mathbf{j}}$  (see Fig. 4.16).

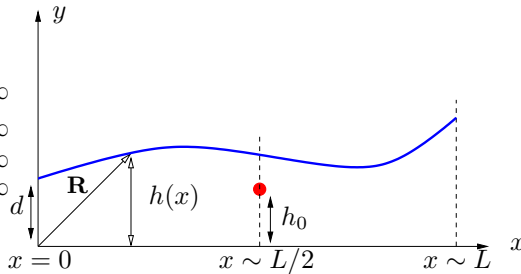


**Figure 4.16** A polymer starting from a fixed position and orientation (clamped) and fluctuating above a point barrier. The other end is hinged at  $x \sim L$  such that it can slip in the  $y$  direction and choose different orientations.

We can write  $h(x)$  in terms of the following discrete Fourier modes

$$h(x) = d + \sum_{n=1}^{\infty} h_n \sin\left(\frac{n\pi x}{L}\right), \quad (4.47)$$

which satisfies the boundary condition  $h(x=0) = d$ .

The harmonic bending energy of the polymer for the displacement  $h(x)$  is

$$\begin{aligned} \mathcal{H} &= \frac{\kappa}{2} \int_0^L \left(\frac{\partial^2 h}{\partial x^2}\right)^2 dx \\ &= \frac{\kappa}{2} \int_0^L \sum_{n,n'} h_n h'_{n'} \left(\frac{n\pi}{L}\right)^2 \left(\frac{n'\pi}{L}\right)^2 \sin\left(\frac{n\pi x}{L}\right) \sin\left(\frac{n'\pi x}{L}\right) dx \\ &= \frac{\kappa L}{4} \sum_n \left(\frac{n\pi}{L}\right)^4 h_n^2, \end{aligned} \quad (4.48)$$

which contains bending rigidity  $\kappa$  as well as contour length  $L$ .

To begin with, we fix the midpoint fluctuations of our polymer at some arbitrary value,  $y$ , as follows:

$$y = d + \sum_{n=1}^{\infty} h_n \sin\left(\frac{n\pi}{2}\right). \quad (4.49)$$

We incorporate this constraint into the calculation of the sum over all the polymer conformations, represented by our partition function  $\mathcal{Z}_y$

$$\begin{aligned} \mathcal{Z}_y &= \mathcal{N}^{-1} \int_{-\infty}^{+\infty} \prod_n dh_n \delta\left(d - y + \sum_{n=1}^{\infty} h_n \sin\frac{n\pi}{2}\right) e^{-\beta\mathcal{H}} \\ &= \frac{\mathcal{N}^{-1}}{2\pi} \int_{-\infty}^{+\infty} \prod_n dh_n \int_{-\infty}^{+\infty} d\mu e^{i\mu(d-y+\sum_{n=1}^{\infty} h_n \sin\frac{n\pi}{2})} \\ &\quad \times e^{-\frac{\beta\kappa L}{4} \left(\frac{\pi}{L}\right)^4 \sum_{n=1}^{\infty} n^4 h_n^2}, \end{aligned} \quad (4.50)$$

in which  $\mathcal{N}$  is a normalization factor. We have also used the following equality (Abramowitz and Stegun, 1970)

$$\delta(z) = \frac{1}{2\pi} \int_{-\infty}^{\infty} d\mu e^{-iz\mu}. \quad (4.51)$$

Carring out the functional integral over  $h_n$  in Eq. 4.50, we arrive at the following expression for  $\mathcal{Z}_y$

$$\begin{aligned} \mathcal{Z}_y &= \frac{\mathcal{N}^{-1}}{2\pi} \int_{-\infty}^{+\infty} d\mu \exp \left[ \sum_{n=1}^{\infty} \ln \left( \frac{4L^3}{\beta\kappa\pi^3 n^4} \right)^{1/2} \right] \\ &\times \exp[i\mu(d-y)] \exp \left[ - \sum_{n=1}^{\infty} \frac{\mu^2 \sin^2(\frac{n\pi}{2}) L^3}{\beta\kappa\pi^4 n^4} \right]. \end{aligned} \quad (4.52)$$

The second summation over  $n$  leads to the following closed form (Hansen, 1975)

$$\sum_{n=1}^{n=\infty} \frac{\sin^2(n\pi/2)}{n^4} = \frac{\pi^4}{96}. \quad (4.53)$$

We use Eq. 4.53 to sum up the second series over  $n$ , enabling us to write

$$\begin{aligned} \mathcal{Z}_y &= \frac{\mathcal{N}^{-1}}{2\pi} \int_{-\infty}^{+\infty} d\mu \exp[i\mu(d-y)] \times \\ &\exp \left[ \sum_{n=1}^{n=\infty} \left( \frac{4L^3}{\beta\kappa\pi^3 n^4} \right)^{1/2} \right] \times \exp \left[ - \frac{1}{96} \frac{\mu^2 L^3}{\beta\kappa} \right]. \end{aligned} \quad (4.54)$$

Now, carrying out a final integration over  $\mu$ , we arrive at the desired expression for  $\mathcal{Z}_y$

$$\mathcal{Z}_y = B \exp[-CY^2], \quad (4.55)$$

in which  $B = \sqrt{6\beta\kappa/\pi L^3}$ ,  $C = 6\beta\kappa/L$  and  $Y = (d-y)/L$ . The normalization factor is calculated to be

$$\mathcal{N} = \exp \left[ \sum_{n=1}^{n=\infty} \left( \frac{4L^3}{\beta\kappa\pi^3 n^4} \right)^{1/2} \right], \quad (4.56)$$

such that  $\int_{-\infty}^{\infty} dy \mathcal{Z}_y = 1$ .

In order to complete the calculations of the partition function for our polymer, including the presence of the point barrier, we need to further integrate  $\mathcal{Z}_y$  from the position of the point barrier,  $h_0$ , to  $\infty$ . In this way, we realize the physical constraint that we wish to impose; that the polymer midpoint must fluctuate entirely above the point barrier and never below it (Fig. 4.16). So we write

$$\mathcal{Z}_{h_0} = \int_{h_0}^{\infty} dy \mathcal{Z}_y. \quad (4.57)$$

Carring out the integral in Eq. 4.57, we end up with our final expression for  $\mathcal{Z}_{h_0}$

$$\mathcal{Z}_{h_0} = \frac{1}{2} \operatorname{Erfc}[\sqrt{C}X], \quad (4.58)$$

which is the same as Eq. 4.39 with  $C = 6\beta\kappa/L = 6\ell_p/L$  and  $X = (h_0 - d)/L$ .

## 4.4 Summary

We have presented analytical calculations as well as Monte Carlo simulations for the force exerted by a fluctuating polymer on a rigid rod. The system has been analysed for two different geometries:

I) The filament fluctuates parallel to the rigid rod. In this case, the free energy of the polymer is greater than that of a free filament. As a result, the polymer feels an effective repulsive force which scales as  $\langle h \rangle^{-5/3}$ , in which  $\langle h \rangle$  is the average distance between polymer and rigid rod. The same results can be obtained by using scaling arguments. We also performed MC simulations for different persistence lengths in the presence of a constant external pressure. MC data, clearly shows that the polymer binds to the rigid rod at a given distance in which the external attractive force is in balance with the steric repulsive force. At very small distances, the entropic force is dominated but decays very fast at larger distances.

II) The filament fluctuates perpendicular to the rigid rod. We have outlined the calculations for the force exerted by a fluctuating polymer on a point barrier using statistical mechanical methods. We explicitly and quantitatively derive the polymer force acting on a point barrier in terms of polymer contour length  $L$  and persistence length  $\ell_p$ . We calculated the force in two ways: path integral method and propagator method. We find that at large negative distances, the force between the polymer and the point barrier decays exponentially to zero. However, at small and large positive distances, force can be approximated by a Hookian force with dimensionless spring constants  $24\ell_p/L$  and  $12\ell_p/L$ , respectively. MC simulations fits very good to the analytical results just for stiff filaments ( $\epsilon \leq 1$ ) and deviates at intermediate and large values of  $\epsilon$ .



# 5 Velocity oscillations in actin-based motility

This chapter is under review in Phys. Rev. Lett. as: A. Gholami, M. Falcke, and E. Frey: *Velocity oscillations in actin-based motility* (arXiv:0704.1390v1).

## Abstract

We present a simple and generic theoretical description of actin-based motility, where polymerization of filaments maintains propulsion. The dynamics is driven by polymerization kinetics at the filaments' free ends, crosslinking of the actin network, attachment and detachment of filaments to the obstacle interfaces and entropic forces. We show that spontaneous oscillations in the velocity emerge in a broad range of parameter values, and compare our findings with experiments.

## 5.1 Introduction

Force generation by semiflexible polymers is versatily used for cell motility. The leading edge of lamellipodia of crawling cells (Bray, 2001) is pushed forward by a polymerizing actin network and bacteria move inside cells by riding on a comet tail of growing actin filaments (Plastino and Sykes, 2005; Gouin *et al.*, 2005). In vivo systems are complemented by in vitro assays using plastic beads and lipid vesicles (Loisel *et al.*, 1999; Marcy *et al.*, 2004; Parekh *et al.*, 2005). The defining feature of semiflexible polymers is the order of magnitude of their bending energy which is in the range of  $k_B T$ . They undergo thermal shape fluctuations and the force exerted by the filaments against an obstacle arises from *elastic and entropic* contributions (Mogilner and Oster, 1996a; Gholami *et al.*, 2006).

Mathematical models have quantified the force generated by actin filaments growing against obstacles (Hill, 1981b; Mogilner and Oster, 1996a; Gholami *et al.*, 2006). The resisting force depends on the obstacle which is pushed. In case of pathogens, it has a small component from viscous drag of the moving obstacle but consists mainly of the force exerted by

actin filaments bound to the surface of the bacteria and pulling it backwards (Cameron *et al.*, 2001; Kuo and McGrath, 2000). The tethered ratchet model (Mogilner and Oster, 2003) is a mathematical formulation of these experimental findings in terms of the dynamics of the number of attached and detached polymers. The starting point of our approach will be the dynamics of the distributions of the free length of both polymer populations.

Actin polymerization in living cells and extracts is controlled by a complex molecular network (Gouin *et al.*, 2005). Nucleation of new filaments, capping of existing ones, exchange of ADP for ATP on actin monomers, buffering of monomers etc. all contribute to that control and have been modeled (Carlsson, 2003; Mogilner and Oster, 2003; Gracheva and Othmer, 2004). Our goal is not to model the full complexity of that biochemical network. Rather we focus on the core process of force generation and force balance ensuing from the interplay between bound pulling filaments and polymerizing pushing filaments, the transition between these two groups and the motion of the whole force generating configuration. This is motivated by recent observations of complex dynamics in simple reconstituted systems: the velocity of beads or pathogens propelled by actin polymerization may oscillate (Lasa *et al.*, 1997; Gerbal *et al.*, 2000a; Bernheim-Groswasser *et al.*, 2005). Our goal is to describe the dynamics of such biochemically simpler systems and find a robust microscopic description for oscillation mechanisms, which may then be controlled by higher order processes. Such a study is meant to complement investigations based on a continuum approach (Gerbal *et al.*, 2000a; Bernheim-Groswasser *et al.*, 2005).

## 5.2 Definition of the model

We consider a fixed number  $N$  of actin filaments <sup>1</sup> firmly anchored into a rigid cross-linked network, which advances with velocity  $v_g$ ; for an illustration see Fig. 5.1. Filaments of variable length  $l$  are either attached to the obstacle interface via a protein complex or detached from it, with time-dependent number distributions denoted by  $N_a(l, t)$  and  $N_d(l, t)$ , respectively. In the detached state, filaments polymerize at a velocity  $v_p(l, x)$ , which depends on both the polymer length  $l$  and the distance  $x$  between rigid support and obstacle. Transitions between the two filament popu-

---

<sup>1</sup>A constant number is assumed to simplify matters. It has been shown, however, that a variable number of filaments is not required for propulsion; see e.g. Briehner *et al.* (2004)

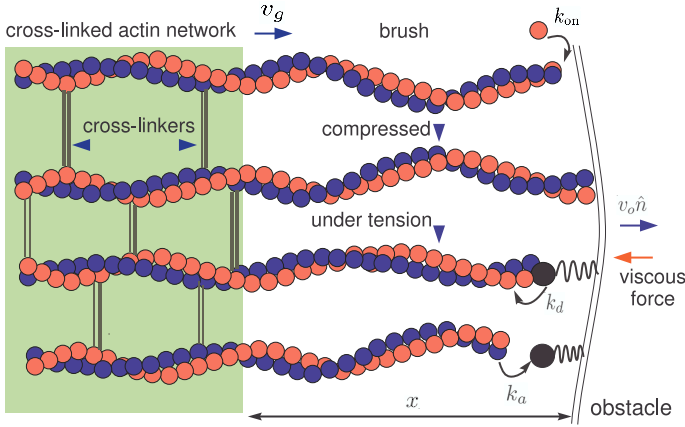


**Figure 5.1** Schematic representation of an ensemble of actin filaments oriented at  $\vartheta = 0$  with respect to the normal  $\hat{n}$  of an obstacle interface, which may either be a cell membrane or a bacterium. While attached filaments are under tension and pull the interface back, detached filaments are compressed, elongate by polymerization with rate  $k_{on}$  and push the interface forward. All filaments in the brush are firmly anchored in a cross-linked network, whose front advances with velocity  $v_g$  reducing the free length  $l$  of the filaments. Attached filaments detach with stress dependent rate  $k_d$  and detached filaments attach with constant rate  $k_a$ .  $v_o$  is the interface velocity in the extracellular medium, and  $x$  is the distance between the front of the network and the interface.

lations occur with a constant attachment rate  $k_a$  and a stress-dependent detachment rate  $k_d$  (Evans and Ritchie, 1999). This results in the evolution equations

$$\frac{\partial}{\partial t} N_d - \frac{\partial}{\partial l} \left[ \frac{l}{x} v_g(l) - v_p \right] N_d = -k_a N_d + k_d N_a, \quad (5.1a)$$

$$\frac{\partial}{\partial t} N_a - \frac{\partial}{\partial l} \left[ \frac{l}{x} v_g(l) \right] N_a = k_a N_d - k_d N_a. \quad (5.1b)$$

The right hand side of Eq. (5.1) describes attachment and detachment process. The second term on the left hand side accounts for the gain and loss of attached and detached polymers due to the dynamics of the polymer mesh, growing with velocity  $v_g$ , and the polymerization kinetics of the filaments in the brush. The correction factor  $l/x$  in front of  $v_g$  is due to the fact that for bent polymers the rigid network swallows by this amount more in contour length than for straight filaments. This factor is equal to

1 for  $l \leq x$ .

Processes contributing to the growth of the rigid polymer mesh are entanglement and crosslinking of filaments in the brush. Both imply a vanishing  $v_g$  for  $l \rightarrow 0$ , since short polymers do not entangle and crosslinking proteins are unlikely to bind to them. At the same time  $v_g$  can not grow without bound but must saturate at some value  $v_g^{\max}$  due to rate limitations for crosslinker binding. This suggests to take the following sigmoidal form

$$v_g(l) = v_g^{\max} \tanh(l/\bar{l}), \quad (5.2)$$

with a characteristic length scale  $\bar{l}$ .

The polymerization rate is proportional to the probability of a gap of sufficient size  $\delta$  ( $\approx 2.7$  nm) between the polymer tip and the obstacle for insertion of an actin monomer (Mogilner and Oster, 1996a). This implies an exponential dependence of  $v_p$  on the force  $F_d$  by which the polymer pushes against the obstacle,

$$v_p(l, x) = v_p^{\max} \exp[-\delta \cdot F_d(l, x)/k_B T]. \quad (5.3)$$

Here,  $v_p^{\max} \approx 500$  nm s<sup>-1</sup> (Mogilner and Oster, 1996a) is the free polymerization velocity. For the entropic force  $F_d$  we use the results obtained in Ref. Gholami *et al.* (2006) for  $d = 2, 3$  spatial dimensions, where we take the accepted value of  $\ell_p \approx 15$   $\mu$ m (LeGoff *et al.*, 2002; Ott *et al.*, 1993) for the persistence length of F-actin.

The dynamics of the distance  $x$  between grafted end of the filament and the obstacle interface (see Fig. 5.1) is given by the difference of the average  $v_g$  and the velocity of the obstacle

$$\begin{aligned} \partial_t x = & -\frac{1}{N} \int_0^\infty dl v_g(l) [N_a(l, t) + N_d(l, t)] \\ & + \frac{1}{\eta} \int_0^\infty dl [N_a(l, t) F_a(l, x) + N_d(l, t) F_d(l, x)], \end{aligned} \quad (5.4)$$

where  $\eta$  is an effective friction coefficient of the obstacle. The force  $F_a(l, x)$  acting on the obstacle interface results from the compliance of the filaments attached to it by some linker protein complex, which we model as springs with spring constant  $k_l$  and zero equilibrium length. This complex has a nonlinear force-extension relation which we approximate by a piece-wise linear function; for details see the supplementary material. Let  $R_{||} \approx l[1 - l(d-1)/4\ell_p]$  be the equilibrium length of the filament. Then, the elastic response of filaments experiencing small compressional forces ( $x \leq R_{||}$ ) is approximated by a spring constant  $k_{||} = 12k_B T \ell_p^2/(d-1)l^4$  (Kroy and

Frey, 1996). For small pulling forces ( $x \geq R_{\parallel}$ ), the linker-filament complex acts like a spring with an effective constant  $k_{\text{eff}} = k_l k_{\parallel} / (k_l + k_{\parallel})$ . In the strong force regime, the force-extension relation of the filament is highly nonlinear and diverges close to full stretching (Marko and Siggia, 1995). Therefore, only the linker will stretch out. The complete force-extension relation is captured by

$$F_a = \begin{cases} -k_{\parallel}(x - R_{\parallel}), & x \leq R_{\parallel}, \\ -k_{\text{eff}}(x - R_{\parallel}), & R_{\parallel} < x < l, \\ -k_l(x - l) - k_{\text{eff}}(l - R_{\parallel}), & x \geq l. \end{cases} \quad (5.5)$$

Finally, we specify the force-dependence of the detachment rate by

$$k_d = k_d^0 \exp[-\delta \cdot F_a(l, x) / k_B T]. \quad (5.6)$$

Here,  $k_d^0 \approx 0.5 \text{ s}^{-1}$  (Mogilner and Oster, 2003) is the detachment rate in the absence of forces and we have followed Ref. Evans and Ritchie (1999).

## 5.3 Monodisperse distribution and set of ODEs

Eq. (5.1a) has a singularity at  $v_p(l_s) = v_g(l_s)l_s/x$  since the coefficient of the derivative of  $N_d$  with respect to  $l$  is zero at  $l_s$ . To illustrate the key physical features at that singularity, we start with the simple equation  $\partial_t N_d - \partial_l [v_g(l)l/x - v_p(l, x)]N_d = 0$  with  $x$  kept constant. Then those parts of the distribution of  $N_d$  with  $l < l_s$  will grow and catch up with  $l_s$  since  $v_g(l)l/x - v_p(l, x)$  is positive there, while the parts with  $l > l_s$  will shorten towards  $l_s$ . As a consequence the whole distribution will become concentrated at  $l_s$ . To quantify this heuristic argument we expand  $v_g(l)l/x - v_p(l, x)$  up to linear order around  $l_s$  like  $v_1(l - l_s)$  and use the method of characteristics to solve the equation. Starting initially with a Gaussian distribution we obtain  $N_d(l, t) = c(t) \exp[-(l - \bar{l}(t))^2 / w(t)^2]$  with  $c(t) = c_0 \exp(v_1 t)$ ,  $\bar{l}(t) = l_s + (\bar{l}_0 - l_s) \exp(-v_1 t)$  and  $w(t) = w_0 \exp(-v_1 t)$ . This shows that  $N_d$  evolves to a monodisperse distribution which is localized around  $l_s$ . Its width decreases exponentially with time while its height grows exponentially. The time scale for this contraction is given by  $[\partial_l (v_g l/x - v_p)]^{-1}$  (see Fig. 5.2).

Since the same kind of singularity also occurs in the full set of dynamic equations, Eqs. (5.1), we may readily infer that  $N_a$  and  $N_d$  evolve into delta-functions with that dynamics. This is well supported by simulations,

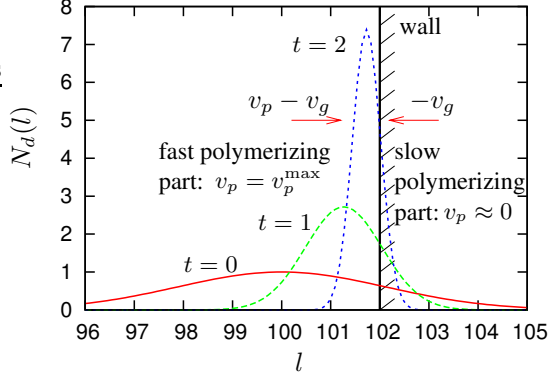


**Figure 5.2** The width of the initial Gaussian distribution of detached filaments decreases exponentially with time and the peak of the distribution grows and localizes around  $l_s$ . In the complete system,  $l_s$  is close to  $\eta$  since  $v_p$  drops from  $v_p^{\max}$  to almost 0 in a narrow range around  $l = \eta$ .

and allows us to continue with the ansatz

$$N_d(l, t) = n_d(t) \delta(l - l_d(t)), \quad (5.7a)$$

$$N_a(l, t) = n_a(t) \delta(l - l_a(t)). \quad (5.7b)$$

It defines the dynamic variables  $n_d(t)$ ,  $l_d(t)$ ,  $n_a(t)$  and  $l_a(t)$ . Upon inserting Eqs. (5.7) into Eqs. (5.1) and Eq. (5.4), we obtain the following set of ordinary differential equations

$$\partial_t l_d(t) = v_p(l_d, x) - \frac{l_d}{x} v_g(l_d) + k_d \frac{n_a}{n_d} (l_a - l_d), \quad (5.8a)$$

$$\partial_t l_a(t) = -\frac{l_a}{x} v_g(l_a) + k_a \frac{n_d}{n_a} (l_d - l_a), \quad (5.8b)$$

$$\partial_t n_a(t) = -k_d(l_a, x) n_a(t) + k_a n_d(t), \quad (5.8c)$$

$$\begin{aligned} \partial_t x(t) &= \frac{1}{\eta} [n_a(t) F_a(l_a, x) + n_d(t) F_d(l_d, x)] \\ &\quad - \frac{1}{N} [v_g(l_a) n_a(t) + v_g(l_d) n_d(t)], \end{aligned} \quad (5.8d)$$

where  $n_d(t) = N - n_a(t)$  since we keep the total number of filaments fixed.

The values of many parameters in the dynamics can be estimated using known properties of actin filaments. We choose the linker spring constant

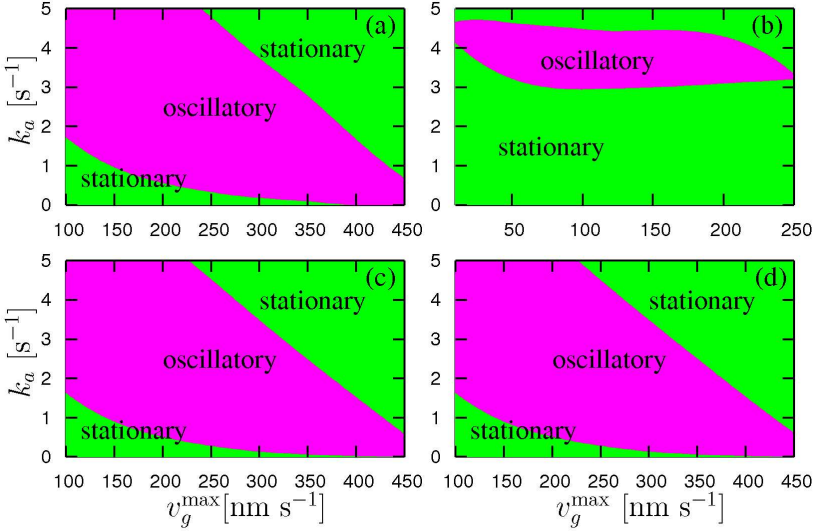


**Figure 5.3** Phase diagram of Eqs. (5.8a) - 5.8d outlining stationary and oscillatory regimes with  $\eta = 10^{-3}$  pN s nm $^{-1}$  for (a-c) and (a)  $d = 2$ ,  $\vartheta = 0$ , (b)  $d = 2$ ,  $\vartheta = \pi/4$ , (c)  $d = 3$ ,  $\vartheta = 0$  and (d)  $d = 3$ ,  $\vartheta = 0$ ,  $\eta = 10^{-5}$  pN s nm $^{-1}$ .  $\bar{l} = 100$  nm, all other parameter values are specified in the text.

$k_l \approx 1$  pN nm $^{-1}$  (Mogilner and Oster, 2003) and assume  $N = 200$  (Mogilner and Oster, 2003) filaments to be crowded behind the obstacle. A realistic value of the drag coefficient  $\eta$  is  $10^{-3}$  pN s nm $^{-1}$  but results did not change qualitatively for a range from  $10^{-5}$  pN s nm $^{-1}$  to  $1$  pN s nm $^{-1}$ .

We have numerically solved Eqs. (5.8) in both  $d = 2$  and  $d = 3$  dimensions, and found the dynamic regimes shown in Fig. 5.3: *stationary states and oscillations*. The existence of an oscillatory regime is very robust against changes of parameters within reasonable limits including the spatial dimension. We checked robustness against changes in the parameter values for the number of polymers  $N$ ,  $\bar{l}$  (see Eq. (5.2)),  $k_l$ ,  $v_p^{\max}$  and  $k_d^0$ , in addition to the examples shown in Fig. 5.3. In general, we find that oscillations occur for  $v_g^{\max} \lesssim 500$  nm s $^{-1}$  and within a range of values for  $k_a$ . Note that the oscillatory region in parameter space depends on the orientation  $\vartheta$  of filaments with respect to the obstacle surface, i.e. oscillating and non-oscillating sub-populations of filaments may coexist in the same network.

Oscillations appear with finite amplitude and period at the lower bound-

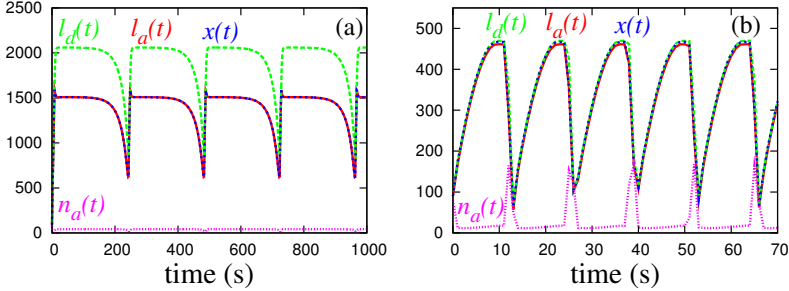


**Figure 5.4**  $x$ ,  $l_a$ ,  $l_d$  (in nm) and  $n_a$  as a function of time, as obtained from a numerical solutions of Eqs. (5.8a - 5.8d) with  $v_g^{\max} = 300 \text{ nm s}^{-1}$  and (a)  $k_a = 0.143 \text{ s}^{-1}$  (b)  $k_a = 3.49 \text{ s}^{-1}$ .  $d = 3$ ,  $\bar{l} = 100 \text{ nm}$  in both panels.

ary of the oscillatory region; compare the example shown in Fig. 5.4a. The stationary state changes stability slightly inside the oscillatory regime and oscillations set in with a finite period. That is compatible with oscillations appearing by a saddle node bifurcation of limit cycles. The upper boundary of the oscillatory region is determined by a Hopf bifurcation. An example of an oscillation close to that bifurcation is shown in Fig. 5.4b.

We start with the description of oscillations in the phase with  $v_g > v_p$ , i.e., decreasing lengths  $x$ ,  $l_a$  and  $l_d$ ; see Fig. 5.4. Then the magnitude of pulling and pushing forces increases due to their length-dependence. When the pushing force becomes too strong, an avalanche-like detachment of attached filaments is triggered and the obstacle jerks forward; compare the steep rise in  $l_d$ ,  $l_a$  and  $x$  shown in Fig. 5.4. That causes a just as sudden drop of the pushing force. With low pushing force now, polymerization accelerates and increases the length of detached filaments. The restoring force of attached filaments is weak in this phase due to their small number. Hence, despite of not so strong pushing forces, the obstacle moves forward. In the meantime, some detached filaments attach to the surface such that the average length and number of attached filaments increases as well. When the detached filaments are long enough to notice the presence of the obstacle interface, they start to buckle. This, in turn, increases the pushing force and slows down the polymerization velocity. Therefore, the graft velocity now exceeds the polymerization velocity and the average lengths of attached and detached filaments start to decrease again and the cycle starts anew. The period of oscillations is dependent on the parameter values. It reduces from 240 s in Fig. 5.4a to 13 s in Fig. 5.4b as  $k_a$  increases

from  $0.143 \text{ s}^{-1}$  to  $3.49 \text{ s}^{-1}$  at  $v_g^{\max} = 300 \text{ nm s}^{-1}$ .

The oscillations in  $x$  correspond to the saltatory motion of the obstacle in the lab frame and the oscillations of its velocity since  $v_g$  stays essentially constant. An illustration is shown in Fig. 5.5 for a given set of parameters which leads to oscillations with periods of the order of 100 s and velocity of the order of  $0.7 \mu\text{m s}^{-1}$ . This is in good agreement with the results of experiments on oscillatory *Listeria* propulsion (Lasa *et al.*, 1997). The period of velocity oscillations with beads propelled by actin polymerization differs from those of *Listeria* by one order of magnitude (8 – 15 min Bernheim-Groswasser *et al.* (2005)). Periods of that length can be obtained within our model upon using values for  $k_a$  close to the lower boundary of the oscillatory regime.

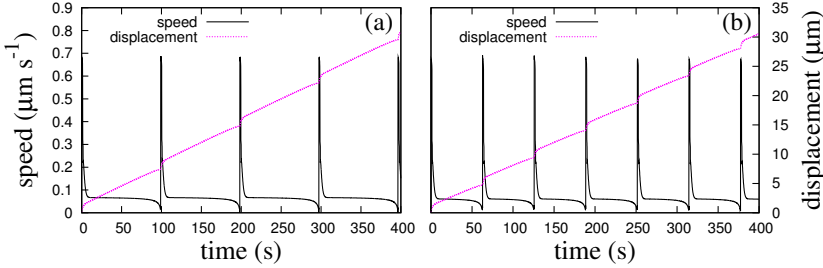


**Figure 5.5** Velocity and displacement of the obstacle as a function of time with (a)  $k_a = 0.9 \text{ s}^{-1}$ , (b)  $k_a = 1 \text{ s}^{-1}$ .  $v_p^{\max} = 750 \text{ nm s}^{-1}$ ,  $v_g^{\max} = 75 \text{ nm s}^{-1}$ ,  $k_d^0 = 0.1 \text{ s}^{-1}$ ,  $\bar{l} = 100 \text{ nm}$ ,  $\eta = 10^{-3} \text{ pN s nm}^{-1}$  and  $d = 3$  in both panels.

We have also studied the system when the network is oriented at an angle  $\vartheta = \pi/4$ . In this case, the spring constant of the attached filaments parallel to  $\hat{n}$  for  $d = 2$  reads  $k_{\parallel}^{-1}(\vartheta) = 4\ell_p^2[\frac{\epsilon}{2} + e^{-\epsilon/2} - 1 + \cos 2\vartheta(\frac{1}{4} + \frac{1}{12}e^{-2\epsilon} - \frac{1}{3}e^{-\epsilon/2}) - \cos^2 \vartheta(e^{-\epsilon/2} - 1)^2]/k_B T$ , where  $\epsilon = l/\ell_p$  and  $R_{\parallel}(\vartheta) = l(1 - l/4\ell_p) \cos \vartheta$  (Kroy and Frey, 1996). For the pushing force of a filament grafted at  $\vartheta = \pi/4$ , we use the results of the factorization approximation given in Ref. Gholami *et al.* (2006), which is well valid for a stiff filament like actin. A numerical solution of Eqs. (5.8a- 5.8d) results in the phase diagram shown in Fig. 5.3b with the adapted forms of  $F_d$  and  $F_a$ . The main effect is that one needs higher values for the attachment rates and lower values for  $v_g$  to obtain oscillations.

## 5.4 Summary

In summary, we have presented a simple and generic theoretical description of oscillations arising from the interplay of polymerization driven pushing forces and pulling forces due to binding of actin filaments to the obstacle. The physical mechanism for such oscillations relies on the load-dependence of the detachment rate and the polymerization velocity, mechanical restoring forces and eventually also on the cross-linkage and/or entanglement of the filament network. The oscillations are very robust with respect to changes in various parameters, i.e. are generic in this model. Therefore, complex biochemical regulatory systems supplementing the core process described here may rather stabilize motion and suppress oscillations than generate them.

Oscillations of the velocity were observed during propulsion of pathogens by actin polymerization. There, the core mechanism described here is embedded into a more complex control of polymerization, which e.g. also comprises nucleation of new filaments and capping of existing ones. Hence, the study presented here can not be expected to fully capture all features of such processes. Our results still agree well with respect to velocity spike amplitudes and periods in *Listeria* experiments reported in Refs. Lasa *et al.* (1997); Gerbal *et al.* (2000a). The velocity in between spikes appears to be smaller in experiments than in our simulations. This may be accounted for in our model by including capping of filaments upon dissociation from the obstacle. Periods may also become longer when capping and nucleation were included since it would take longer to restore the pushing force after the avalanche like rupture of attached filaments. Altogether, qualitative and quantitative comparison with experiments suggests that our model may be a promising candidate for a robust mechanism of velocity oscillations in actin-based bacteria propulsion.

## 6 Summary

Spatially controlled polymerization of actin is at the origin of cell motility and is responsible for the formation of cellular protrusions like lamellipodia. The pathogens *Listeria monocytogenes* and *Shigella flexneri*, move inside the infected cells by riding on an actin tail. The actin tail is formed from highly crosslinked polymerizing actin filaments, which undergo cycles of attachment and detachment to and from the surface of bacteria.

In this thesis, we formulated a simple theoretical model of actin-based motility. The physical mechanism for our model is based on the load-dependent detachment rate, the load-dependent polymerization velocity, the restoring force of attached filaments, the pushing force of detached filaments and finally on the cross-linkage and/or entanglement of the filament network. We showed that attachment and detachment of filaments to the obstacle, as well as polymerization and cross-linking of the filaments lead to spontaneous oscillations in obstacle velocity. The velocity spike amplitudes and periods given by our model are in good agreement with those observed experimentally in *Listeria*. In this model, elasticity and curvature of the obstacle is not included. Future modelling will yield insight into the role of curvature and elasticity in the actin-based motility.

As an important prerequisite for this model, we used analytical calculations as well as extensive Monte Carlo (MC) simulations to investigate the pushing force of detached filaments. The analysis starts with calculations of the entropic force exerted by a grafted semiflexible polymer on a rigid wall. The pushing force, which is purely entropic in origin, depends on the polymer's contour length, persistence length, orientation and eventually on the distance of the grafting point from the rigid wall. We checked the validity range of our analytical results by performing extensive Monte Carlo simulations. This was done for stiff, semiflexible and flexible filaments. In this analysis, the obstacle is always assumed to be a rigid wall. In the real experimental situations, the obstacle (such as membrane) is not rigid and performs thermal fluctuations. Further analytical calculations and MC simulations are necessary to include the elasticity of the obstacle

ActA coated beads are used widely in *in vitro* experiments to study actin-based motility. To investigate the effect of the obstacle curvature on entropic forces, we calculated the total pushing force generated by a

homogeneous actin network on a rigid sphere. Our analysis clearly shows that, the obstacle parameters (like the radius of the sphere) and network properties (such as the orientation of the network) have a direct effect on the magnitude and direction of the total pushing force. These calculations are done for a static system: a constant number of filaments (all with the same contour length) push against a sphere located at a given distance. Attachment and detachment of filaments to and from the sphere, polymerization and crosslinking of filaments, are dynamic processes which have to be included in future modelling.

In the cell cytoskeleton, which is a fiber network of biopolymers, thermal fluctuations of filaments are highly restricted due to the presence of the other filaments. This confinement increases the free energy of each single fluctuating polymer, resulting in an average repulsive force which is entropic in origin. Chapter 4 of this thesis is dedicated to the study of entropic forces between two parallel and perpendicular polymers. Our analytical results, which are complemented by Monte Carlo simulations, clearly show the presence of steric “Helfrich repulsion” between two parallel polymers at short distances.

# Appendix



# A Monte Carlo method

Using standard Monte Carlo methods, we have studied the statistical mechanics of grafted polymers with arbitrary stiffness. In the intermediate values of stiffness (semiflexible polymers), analytical results are difficult to obtain, hence, computer simulations become crucial

The polymer model consists of a chain of  $N$  identical segments. The first segment of the filament is assumed to be clamped, i.e., the orientation of its tangent vector is held fixed along a direction, named the  $z$  axis. The last segment is left free to choose any possible orientation. The way the Metropolis algorithm implemented can be described by a simple recipe:

1. Choose an initial configuration randomly in the proximity of the full stretching condition, thus ensuring a fast convergence to equilibrium,
2. Generate a new configuration by changing orientation of the segment  $i$  (by amount  $\Delta\theta$ ) and parallel translation of the segments  $i+1, \dots, N$ ,
3. Calculate the change in energy  $\Delta E = E_{\text{new}} - E_{\text{old}}$  using the discrete Hamiltonian Eq. 1.4,
4. Generate a random number  $r$  such that  $0 < r < 1$ ,
5. If  $r < \exp(-\Delta E/k_B T)$ , accept the new configuration,
6. Choose another segment and change its orientation and go to 3.

We adjust  $\Delta\theta$  such that to have almost 50 percent acceptance rate. Effects resulting from self-avoidance are not consider, but we notice that configurations where the chain folds back onto itself are strongly energetically suppressed for sufficiently stiff polymers. Results ceased to depend on the number of segments for  $N = 50$ . On the order of  $10^6$  Monte Carlo steps per segment were preformed and at each step the position of the tip was recorded. Histogram of the tip position is a measure of probability distribution of the free fluctuating end,  $P_{\parallel}(z)$ . In the MC simulations to study interaction between a stiff polymer and a point barrier, we also record the position of the segment at the middle of filament.

To study the interaction between a stiff polymer and a rigid wall by MC simulations (Sec. 4.2), another step needs to be added to the above algorithm (after step 2):

2'. If the new configuration crosses the rigid wall, then go to step 2.

## B Euler buckling instability

Consider a rigid rod with contour length  $L$  and bending rigidity  $\kappa$  which is under exertion of an axial force  $f$  in  $-\hat{y}$  direction (Fig. B.1). The question is: how does the end-to-end distance of the beam changes as a function of  $f$ .

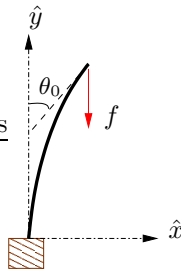


**Figure B.1** A beam under exertion of an axial force  $f$ .

The boundary conditions for this problem are  $\theta = 0$  for  $l = 0$  and  $\theta' = 0$  for  $l = L$ . Then (Landau and Lifshitz, 1959)

$$l = \sqrt{\frac{\kappa}{2f}} \int_0^{\theta_0} \frac{d\theta}{\sqrt{(\cos \theta - \cos \theta_0)}}, \quad (\text{B.1})$$

where  $\theta_0$  is determined by the equation  $l(\theta_0) = L$ . For  $x$  and  $y$  we obtain

$$\begin{aligned} x &= \sqrt{\frac{2\kappa}{f}} [\sqrt{1 - \cos \theta_0} - \sqrt{\cos \theta - \cos \theta_0}], \\ y &= \sqrt{\frac{\kappa}{2f}} \int_0^{\theta} \frac{\cos \theta \, d\theta}{\sqrt{(\cos \theta - \cos \theta_0)}}. \end{aligned} \quad (\text{B.2})$$

For a small deflection,  $\theta_0 \ll 1$ , and we can write

$$L \cong \sqrt{\kappa/f} \int_0^{\theta_0} \frac{d\theta}{\sqrt{(\theta_0^2 - \theta^2)}} = \frac{\pi}{2} \sqrt{\kappa/f}, \quad (\text{B.3})$$

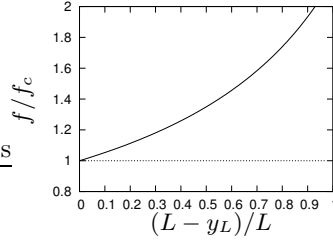


**Figure B.2**  $f/f_c$  as a function of projection of the end-to-end distance of the beam in  $y$ -direction.

i.e.  $\theta_0$  does not appear. This shows that, the solution in problem exists only for  $f > f_c = \pi^2 \kappa / 4L^2$ , i.e. when the rectilinear shape ceases to be stable. For  $f > f_c$ ,  $f$  as a function of  $(L - y_L)/L$  has been presented in Fig. B.2.

Fig. B.3 shows entropic force exerted by a grafted semiflexible polymer on a rigid wall in  $3d$  as well as corresponding mechanical limits. As we see, entropic forces for stiff filaments (small  $\epsilon$ ) approach to mechanical limits, as wall comes closer.

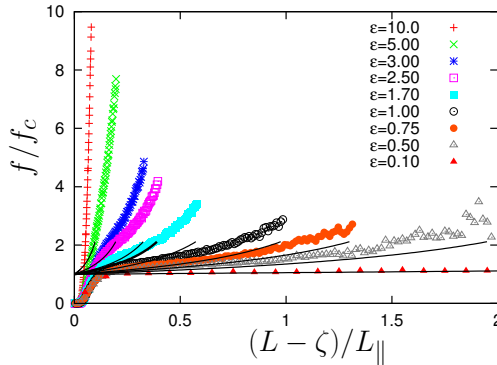


**Figure B.3** Mechanical limits have been presented together with entropic forces generated by a grafted semiflexible polymer on a rigid wall. Entropic forces for stiff filaments (small  $\epsilon$ ) approach mechanical limits as wall comes closer ( $L_{\parallel} = L\epsilon$ ).

# C Laplace and Jacobi transformations

## C.1 Inverse Laplace transform

In this appendix, we collect our calculations of the inverse Laplace transform of the moment generating functions. This will give us two sets of series representations, which show good convergence properties either close to full stretching or for strong compression of the filament.

### C.1.1 Series representation of the 3d tip distribution function for large stored length

Starting from the moment generating function  $\mathcal{P}_{\parallel}(f)$ , one can calculate the distribution function  $P_{\parallel}(z)$  by an inverse Laplace, i.e. an integral along the imaginary axis,

$$P_{\parallel}(z) = \int_{-i\infty}^{+i\infty} \frac{df}{2\pi i} e^{f(L-z)} \mathcal{P}_{\parallel}(f). \quad (\text{C.1})$$

Since the moment generating function

$$\mathcal{P}_{\parallel}(f) = \prod_{k=1}^{\infty} \left( 1 + \frac{4fL^2}{\ell_p(2k-1)^2\pi^2} \right)^{-1} \quad (\text{C.2})$$

has poles at  $f_k = -\lambda_k^2 \ell_p / L^2$  with  $k = 1, 2, 3, \dots$  only along the negative real axis, standard residuum calculus gives

$$\mathcal{P}_{\parallel}(f) = \sum_{k=1}^{\infty} e^{-(L-z)\lambda_k^2 \ell_p / L^2} \prod_{l \neq k} \left( 1 - \frac{(2k-1)^2}{(2l-1)^2} \right)^{-1} \left( \frac{\ell_p \lambda_k^2}{L^2} \right) \quad (\text{C.3})$$

Using  $\prod_{k=1}^{\infty} \left(1 - \frac{x^2}{(2k-1)^2}\right) = \cos\left(\frac{\pi}{2}x\right)$  (Abramowitz and Stegun, 1970), the product term can be written as

$$\begin{aligned} & \prod_{l \neq k} \left(1 - \frac{(2k-1)^2}{(2l-1)^2}\right)^{-1} \\ & \lim_{k' \rightarrow k} \left(1 - \frac{(2k'-1)^2}{(2k-1)^2}\right) \prod_l \left(1 - \frac{(2k'-1)^2}{(2l-1)^2}\right)^{-1} = \\ & \lim_{k' \rightarrow k} \left(1 - \frac{(2k'-1)^2}{(2k-1)^2}\right) \cos^{-1}\left(\frac{\pi}{2}(2k'-1)\right) = \\ & 2 \frac{(-1)^{k+1}}{\pi} \frac{2}{2k-1} = 2(-1)^{k+1} \frac{1}{\lambda_k}. \end{aligned} \quad (\text{C.4})$$

Hence we find

$$\mathcal{P}_{\parallel}(z) = 2L_{\parallel}^{-1} \sum_{k=1}^{\infty} (-1)^{k+1} \lambda_k \exp[-\lambda_k^2(L-z)/L_{\parallel}] \quad (\text{C.5})$$

with the characteristic longitudinal length scale  $L_{\parallel} = L^2/\ell_p$ .

### C.1.2 Series representation for the tip distribution function close to full stretching: general d

We begin the analysis with the two-dimensional case, where

$$\mathcal{P}_{\parallel}(f) = \prod_{k=1}^{\infty} \left(1 + \frac{fL_{\parallel}}{\lambda_k^2}\right)^{-1/2} = \sqrt{\frac{1}{\cosh \sqrt{fL_{\parallel}}}}. \quad (\text{C.6})$$

For the derivation of our first series representation, we start from the product formula for the moment generating function. In this representation, one has branch cuts on the negative real axis at  $\tilde{f} = fL_{\parallel} = -\lambda_k^2$  for  $k \in \mathbb{N}$ . We now deform the contour in the complex plane such that we enclose the negative real axis. Then

$$\begin{aligned} \tilde{\mathcal{P}}_{\parallel}(\tilde{\rho}) &= \int_{-i\infty}^{+i\infty} \frac{d\tilde{f}}{2\pi i} e^{\tilde{f}\tilde{\rho}} \tilde{\mathcal{P}}_{\parallel}(\tilde{f}) \\ &= \int_{-\infty}^0 \frac{d\tilde{f}}{2\pi i} e^{\tilde{f}\tilde{\rho}} \tilde{\mathcal{P}}_{\parallel}(\tilde{f} - i\epsilon) + \int_0^{-\infty} \frac{d\tilde{f}}{2\pi i} e^{\tilde{f}\tilde{\rho}} \tilde{\mathcal{P}}_{\parallel}(\tilde{f} + i\epsilon) \\ &= \int_0^{\infty} \frac{d\tilde{f}}{2\pi i} e^{-\tilde{f}\tilde{\rho}} \left[ \tilde{\mathcal{P}}_{\parallel}(-\tilde{f} - i\epsilon) - \tilde{\mathcal{P}}_{\parallel}(-\tilde{f} + i\epsilon) \right] \end{aligned} \quad (\text{C.7})$$

where  $\epsilon \rightarrow 0$ . To proceed, we need to evaluate the product formula on the negative real axis. We find for  $x \in [2k+1, 2k+3]\frac{\pi}{2}$

$$\lim_{\epsilon \rightarrow 0} \prod_{l=1}^{\infty} \sqrt{1 - \frac{x^2 \mp i\epsilon}{\lambda_l^2}} = (\mp i)^k \frac{1}{\sqrt{|\cos x|}} \quad (\text{C.8})$$

Upon substituting  $y^2 = \tilde{f}$ , this finally results in the series expansion

$$\tilde{P}_{\parallel}(\tilde{\rho}) = \frac{2}{\pi} \sum_{n=0}^{\infty} (-1)^n \int_{\lambda_{2n+1}}^{\lambda_{2n+2}} dy \frac{y e^{-y^2 \tilde{\rho}}}{\sqrt{|\cos y|}}. \quad (\text{C.9})$$

For large values of  $\tilde{\rho}$ , corresponding to a significant compression of the polymer, the integral is dominated by the contribution from the interval  $[\pi/2, 3\pi/2]$ , such that the leading factor will be proportional to  $\exp(-\pi^2 \tilde{\rho}/4)$ . In order to evaluate  $\tilde{P}_{\parallel}(\tilde{\rho})$  further, we may average  $ye^{-y^2 \tilde{\rho}}$  over the interval and approximate the integral as

$$\int_{\lambda_{2n+1}}^{\lambda_{2n+2}} \frac{y e^{-y^2 \tilde{\rho}} dy}{\sqrt{|\cos y|}} \approx \frac{1}{5} \sum_{m=4}^8 \lambda_{2n+\frac{m}{4}} e^{-\lambda_{2n+\frac{m}{4}}^2 \tilde{\rho}} \int_{\frac{\pi}{2}}^{\frac{3\pi}{2}} \frac{dy}{\sqrt{|\cos y|}} \quad (\text{C.10})$$

such that we finally get

$$\tilde{P}_{\parallel}(\tilde{\rho}) \approx \frac{1}{\mathcal{N}} \sum_{n=0}^{\infty} (-1)^n \sum_{m=4}^8 \lambda_{2n+\frac{m}{4}} \exp\left[-\lambda_{2n+\frac{m}{4}}^2 \tilde{\rho}\right], \quad (\text{C.11})$$

where

$$\mathcal{N}^{-1} = \frac{2}{5\pi} \int_{\frac{\pi}{2}}^{\frac{3\pi}{2}} \frac{dy}{\sqrt{|\cos y|}} \approx 0.67. \quad (\text{C.12})$$

Next we drive a series representation suitable for small values of  $\tilde{\rho}$ . We use that for  $f \in \mathbb{R}_+$  one has (Hansen, 1975)

$$\mathcal{P}_{\parallel}(f) = \frac{1}{\sqrt{\cosh \sqrt{fL_{\parallel}}}}. \quad (\text{C.13})$$

With  $\cosh(x) = \frac{1}{2}(e^x + e^{-x})$  and the generalized binomial theorem, this can be expanded to give

$$\mathcal{P}_{\parallel}(f) = \sqrt{2} \sum_{l=0}^{\infty} \binom{-\frac{1}{2}}{l} e^{-(2l+1/2)\sqrt{fL_{\parallel}}}, \quad (\text{C.14})$$

which is a holomorphic function on  $\mathbb{C} \setminus \mathbb{R}_-$ . Hence by the theorem of identity from complex calculus this formula remains valid  $\forall f \in \mathbb{C} \setminus \mathbb{R}_-$ . Substituting  $y = \sqrt{fL_{\parallel}}$  transforms Eq. (C.1) to

$$\tilde{P}_{\parallel}(\tilde{\rho}) = \int_{-i\infty+\varepsilon}^{i\infty+\varepsilon} \frac{dy}{\pi i} e^{y^2 \tilde{\rho}} y \tilde{\mathcal{P}}_{\parallel}(y^2). \quad (\text{C.15})$$

Inserting the series representation Eq. (C.14) and using the integral representation

$$D_1(z) = \sqrt{2\pi} e^{\frac{z^2}{4}} \int_{-i\infty+\varepsilon}^{i\infty+\varepsilon} \frac{ds}{2\pi i} s \exp\left[-zs + \frac{s^2}{2}\right] \quad (\text{C.16})$$

for the parabolic cylinder function (Abramowitz and Stegun, 1970) as well as

$$\binom{-\frac{1}{2}}{l} = (-1)^l \frac{(2l-1)!!}{2^l l!}, \quad (\text{C.17})$$

where  $n!! = n(n-2)(n-4) \dots$  yields

$$\begin{aligned} \tilde{P}_{\parallel}(\tilde{\rho}) &= \frac{1}{\sqrt{\pi\tilde{\rho}}} \sum_{l=0}^{\infty} (-1)^l \frac{(2l-1)!!}{2^l l!} \\ &\times \exp\left[-\frac{(l+\frac{1}{4})^2}{2\tilde{\rho}}\right] D_1\left[\frac{2l+\frac{1}{2}}{\sqrt{2\tilde{\rho}}}\right]. \end{aligned} \quad (\text{C.18})$$

With  $D_1(x) = xe^{-x^2/4}$  Eq. (C.18) becomes Eq. (2.50).

Finally, all the calculations are easily generalized to general spatial dimensions  $d$ . One finds the series representation

$$\begin{aligned} \tilde{P}_{\parallel}(\tilde{\rho}) &= 2^{d/2} \frac{1}{\sqrt{2\pi}} \sum_{l=0}^{\infty} \binom{-\frac{1}{2}(d-1)}{l} \\ &\times \frac{l + \frac{1}{4}(d-1)}{\tilde{\rho}^{3/2}} \exp\left[-\frac{(l + \frac{d-1}{4})^2}{\tilde{\rho}}\right] \end{aligned} \quad (\text{C.19})$$

which is the fast converging for small  $\tilde{\rho}$ .

## C.2 Saddle point approximation

Starting from Eq. (C.1) and introducing  $\tilde{f} = fL_{\parallel}$  gives

$$\begin{aligned} P_{\parallel}(z) &= \int_{-i\infty}^{+i\infty} \frac{df}{2\pi i} e^{fL_{\parallel}\tilde{\rho}} \cosh^{-1} \sqrt{fL_{\parallel}} \\ &= L_{\parallel}^{-1} \int_{-i\infty}^{+i\infty} \frac{d\tilde{f}}{2\pi i} \frac{2e^{\tilde{f}\tilde{\rho}}}{e^{\sqrt{\tilde{f}}} + e^{-\sqrt{\tilde{f}}}}. \end{aligned} \quad (\text{C.20})$$

We are interested to the asymptotic result of the integral close to full stretching  $\tilde{\rho} \rightarrow 0$ . Upon substituting  $\tilde{f} = \xi/\tilde{\rho}^2$  one finds

$$P_{\parallel}(z) = \frac{2}{\tilde{\rho}^2 L_{\parallel}} \int_{-i\infty}^{+i\infty} d\xi \frac{\exp[f(\xi)/\tilde{\rho}]}{1 + \exp[-2\sqrt{\xi}/\tilde{\rho}]} \quad (\text{C.21})$$

where  $f(\xi) = \xi - \sqrt{\xi}$ . Since the function  $f(\xi)$  has a global maximum at  $\xi_0 = 0.25$ , the main contribution to the integral in the limit  $1/\tilde{\rho} \rightarrow \infty$  comes from the integration along the curve of steepest descent which passes through  $\xi_0$ . We need to find this curve such that  $\Im[f(\xi)] = \text{constant} = \Im[f(\xi_0)] = 0$ . We write  $\sqrt{\xi} = \sqrt{a}(1 + is)$  in terms of the curve parameter  $s$ . Then the condition  $\Im[f(\xi_0)] = 0$  gives  $a = 1/4$ , and the curve of steepest descent is given in terms of  $\Re[\xi] = \frac{1}{4}(1 - s^2)$  and  $\Im[\xi] = 2as$ , which is a parabola parametrized by  $s$ . The saddle point approximation amounts to a contour integral along this parabola, where  $f(\xi) = -(1 + s^2)/4$ , such that

$$P_{\parallel}(z) = \frac{1}{L_{\parallel}\tilde{\rho}^2} \int_{-\infty}^{\infty} \frac{ds}{2\pi} (1 + is) \frac{e^{-(1+s^2)/4\tilde{\rho}}}{1 + e^{-(1+is)/\tilde{\rho}}}. \quad (\text{C.22})$$

To the leading order in  $\tilde{\rho}$  we get

$$\begin{aligned} P_{\parallel}(z) &= \frac{\exp[-1/4\tilde{\rho}]}{\tilde{\rho}^2 L_{\parallel}} \int_{-\infty}^{+\infty} \frac{ds}{2\pi} \exp\left[\frac{-s^2}{4\tilde{\rho}}\right] \\ &= \frac{1}{\sqrt{\pi\tilde{\rho}^3} L_{\parallel}} \exp\left[-\frac{1}{4\tilde{\rho}}\right] \end{aligned} \quad (\text{C.23})$$

In the two dimensional case (2d), using the same strategy and substituting  $\tilde{f} = \xi/\tilde{\rho}^{4/3}$  gives

$$P_{\parallel}(z) = \frac{1}{\sqrt{8\pi\tilde{\rho}^3} L_{\parallel}} \exp\left[-\frac{1}{16\tilde{\rho}}\right]. \quad (\text{C.24})$$

### C.3 Jacobi transformation of the restricted partition sum

To unclutter the formulas in this section, we use the generic argument  $x$  with  $x \equiv \eta_{\parallel}$ .  $\mathcal{Z}_{\parallel}(x)$  can be written as

$$\begin{aligned}\tilde{\mathcal{Z}}_{\parallel}(x) &= 2 \int_0^{\infty} dy \sum_{k=-\infty}^{\infty} (-1)^{k+1} \delta(y - \lambda_k) \frac{1}{y} e^{-\ell_{\text{p}} y^2 x} \\ &= 2 \int_0^{\infty} dy \tilde{\delta}(y) \frac{1}{y} e^{-\ell_{\text{p}} y^2 x}\end{aligned}\quad (\text{C.25})$$

where we defined

$$\tilde{\delta}(y) := \sum_{k=-\infty}^{\infty} (-1)^{k+1} \delta(\lambda_k - y). \quad (\text{C.26})$$

Since  $\tilde{\delta}(y)$  is odd in  $y$  and has periodicity  $2\pi$ , we can expand it into a Fourier-sine-series:

$$\tilde{\delta}(y) = \sum_{l=1}^{\infty} d_l \sin(l y) \quad (\text{C.27})$$

where

$$\begin{aligned}d_l &= \frac{2}{\pi} \int_0^{\pi} dy \tilde{\delta}(y) \sin(l y) \\ &= \frac{2}{\pi} \sin(l \pi / 2) \\ &= \frac{2}{\pi} \begin{cases} 0 & \text{if } l \text{ is even} \\ (-1)^{\frac{l-1}{2}} & \text{if } l \text{ is odd} \end{cases}.\end{aligned}\quad (\text{C.28})$$

This results in

$$\tilde{\delta}(y) = \frac{2}{\pi} \sum_{l=1}^{\infty} (-1)^{l+1} \sin[(2l-1)y]. \quad (\text{C.29})$$

Inserting this into Eq. (C.25) we find for  $\tilde{\mathcal{Z}}_{\parallel}(x)$

$$\tilde{\mathcal{Z}}_{\parallel}(x) = \frac{4}{\pi} \sum_{l=1}^{\infty} (-1)^{l+1} \int_0^{\infty} dy y^{-1} e^{-y^2 x} \sin[(2l-1)y] \quad (\text{C.30})$$

The integral evaluates to (Abramowitz and Stegun, 1970) (with  $\mu = 0$ ,  $\beta = x$ ,  $\gamma = 2l - 1$ )

$$\begin{aligned} & \int_0^\infty dy y^{-1} e^{-y^2 x} \sin[(2l-1)y] \\ &= \frac{(2l-1)e^{-(2l-1)^2/4x}}{2\sqrt{x}} \sqrt{\pi} {}_1F_1\left(1; \frac{3}{2}; \frac{(2l-1)^2}{4x}\right) \end{aligned} \quad (\text{C.31})$$

As the confluent hypergeometric function  ${}_1F_1(\alpha; \gamma; z) \equiv \Phi(\alpha, \gamma; z)$  has the property  $\Phi(\alpha; \gamma; z) = e^z \Phi(\gamma - \alpha, \gamma; -z)$  (Abramowitz and Stegun, 1970) we find with (Abramowitz and Stegun, 1970)

$$\begin{aligned} \Phi\left(1, \frac{3}{2}; z\right) &= e^z \Phi\left(\frac{1}{2}, \frac{3}{2}; -z\right) \\ &= \frac{\sqrt{\pi} e^z}{2\sqrt{z}} \operatorname{erf}\sqrt{z}. \end{aligned} \quad (\text{C.32})$$

Our result for  $\tilde{Z}_{\parallel}(x)$  is thus

$$\tilde{Z}_{\parallel}(x) = 2 \sum_{l=1}^{\infty} (-1)^{l+1} \operatorname{erf} \frac{2l-1}{2\sqrt{x}} \quad (\text{C.33})$$

This still has problems for  $x \rightarrow 0$  where  $\operatorname{erf}[(2l-1)/2\sqrt{x}] \rightarrow 1$ . We can, however rewrite it to

$$\tilde{Z}_{\parallel}(x) = 2 \sum_{l=1}^{\infty} (-1)^{l+1} + 2 \sum_{l=1}^{\infty} (-1)^l \operatorname{erfc} \frac{2l-1}{2\sqrt{x}}. \quad (\text{C.34})$$

All convergence problems are now isolated in the first sum. As we know that  $\tilde{Z}_{\parallel}(0) = 1$  (compare Eq. (2.36)) we assign  $2 \sum_{l=1}^{\infty} (-1)^{l+1} = 1$  to finally find

$$\tilde{Z}_{\parallel}(x) = 1 + 2 \sum_{l=1}^{\infty} (-1)^l \operatorname{erfc} \frac{2l-1}{2\sqrt{x}}. \quad (\text{C.35})$$

## C.4 Graft-angle-dependent force

We evaluate the general expression Eq. (2.60) using the representation

$$\Theta(x) = \lim_{\varepsilon \rightarrow 0^+} \int \frac{dq}{2\pi i} \frac{e^{iqx}}{q - i\varepsilon} \quad (\text{C.36})$$

of the step function  $\Theta(x)$ . With Eq. (2.73) we find

$$\begin{aligned}
 \mathcal{Z}(\zeta, \vartheta) &= \int \frac{dq}{2\pi i} \frac{\exp\left[iq \frac{\zeta / \cos \vartheta - L}{L_{\parallel}}\right]}{q - i\varepsilon} \times \\
 &\quad \int d\tilde{x} d\tilde{\eta} e^{iq\tilde{\eta}} e^{-iq(L_{\perp}/L_{\parallel}) \tan \vartheta \tilde{x}} \tilde{P}(\tilde{x}, \tilde{\eta}) \\
 &= \int \frac{dq}{2\pi i} \frac{\exp\left[iq \frac{\zeta / \cos \vartheta - L}{L_{\parallel}}\right]}{q - i\varepsilon} a_d(-iq) \\
 &\quad \exp\left[-(qL_{\perp}L_{\parallel}^{-1} \tan \vartheta)^2 3b(-iq)/2\right] \\
 &= \tilde{\mathcal{Z}}\left(\frac{L - \zeta / \cos \vartheta}{L_{\parallel}}, \frac{L_{\perp}}{L_{\parallel}} \tan \vartheta\right) \tag{C.37}
 \end{aligned}$$

where

$$\tilde{\mathcal{Z}}(\eta_{\parallel}, \mu) = - \int \frac{dq}{2\pi i} \frac{e^{iq}}{q + i\varepsilon} a_d(iq) e^{-\frac{3\mu^2 q^2 b(iq)}{2}}. \tag{C.38}$$

Using the Dirac formula

$$\frac{1}{q + i\varepsilon} = \mathcal{P} \frac{1}{q} - i\pi \delta(q), \tag{C.39}$$

$a_3(0) = 1$ ,  $3b(0) = 1$  and the symmetry properties of  $a_3(iq)$  and  $b(iq)$ , we find

$$\tilde{\mathcal{Z}}(\eta_{\parallel}, \mu) = \frac{1}{2} - 2 \int_0^{\infty} \frac{dq}{2\pi} \frac{1}{q} \Im \left( e^{iq\eta_{\parallel}} a_3(iq) e^{-\frac{1}{2}\mu^2 q^2 3b(iq)} \right). \tag{C.40}$$

The notation  $\mathcal{P}$  denoting the principal value has been dropped as the integrand is regular at  $q = 0$ . For large  $\mu$  and/or  $\zeta$ ,  $\tilde{\mathcal{Z}}(\eta_{\parallel}, \mu)$  vanishes. This means that the integral in Eq. (2.85) must approach  $1/2$ . Subtracting the result of the numerically evaluating the non-vanishing integral from  $1/2$  strongly amplifies the unavoidable round-off error. We therefore rewrite Eq. (C.40) to

$$\begin{aligned}
 \tilde{\mathcal{Z}}(\eta_{\parallel}, \mu) &= \frac{1}{2} \operatorname{erfc} \frac{\eta_{\parallel}}{\sqrt{2}\mu} \\
 &\quad - 2 \int_0^{\infty} \frac{dq}{2\pi} \frac{1}{q} \Im \left[ e^{iq\eta_{\parallel}} \left( a_3(iq) e^{-\frac{1}{2}\mu^2 q^2 3b(iq)} - e^{-\frac{\mu^2 q^2}{2}} \right) \right] \tag{C.41}
 \end{aligned}$$

where we used the identity

$$\frac{1}{2} - \mathcal{P} \int_{-\infty}^{\infty} \frac{dq}{2\pi i} \frac{e^{iq\eta_{\parallel}}}{q} e^{-\frac{q^2\mu^2}{2}} = \frac{1}{2} \operatorname{erfc} \frac{\eta_{\parallel}}{\sqrt{2}\mu}. \quad (\text{C.42})$$

As  $\Im q^2 b(iq) \sim -q$  for large  $|q|$ , it is again advantageous to split the integrals at some  $q_0$  and, for  $q > q_0$ , to rewrite the imaginary part appearing in the integrand of Eq. (C.41) to

$$\Im \left[ e^{iq(\eta_{\parallel} + 3\mu^2/2)} \left( a_3(iq) e^{-\frac{3}{2}\mu^2(q^2 b(iq) + iq)} - e^{-\frac{\mu^2 q^2 + 3iq\mu^2}{2}} \right) \right] \quad (\text{C.43})$$

and the real part appearing in Eq. (2.89) to

$$\Re \left( e^{iq(\eta_{\parallel} + 3\mu^2/2)} a_3(iq) e^{-\frac{3}{2}\mu^2(q^2 b(iq) + iq)} \right). \quad (\text{C.44})$$

In both cases, the integrand is holomorphic for  $\Im q < 0$ . Hence the integrals vanish if  $\delta\eta_{\parallel} := \eta_{\parallel} + 3\mu^2/2 < 0$  which we already understood in the simple geometric picture of the problem.

Both integrals now vanish in the limit of large  $\eta_{\parallel}$  and have well-behaved integrands on  $[0, \infty]$ . The precision with which  $\tilde{f}(\eta_{\parallel}, \mu)$  can be calculated is, however, still limited by the relative error in evaluating the integrals. This relative error grows quickly with increasing  $\eta_{\parallel}$  limiting the range of  $\eta_{\parallel}$  over which  $\tilde{f}(\eta_{\parallel}, \mu)$  can be calculated reliably (note that the first term of Eq. (C.41) vanishes with increasing  $\eta_{\parallel}$  as well).



## D Force-extension relation of attached filaments

In this appendix, we discuss the force-extension relation of a filament which is attached to a rigid wall via a linker.

First, consider a semiflexible polymer with contour length  $L$  and persistence length  $l_p$  which is grafted in one end in the  $\hat{z}$  direction. The other free fluctuating end is pulled by an external force  $\mathbf{f} = f\hat{z}$  (Fig. 1.11). The force-extension curve of such a filament is presented in Fig. 1.12. In order to have a closed form of the force-extension relation (especially for compressive forces), we approximate the integral in Eq. (2.20). For compressive forces,  $z \rightarrow 0$  or  $\tilde{\rho} \rightarrow L/L_{\parallel}$  holds. As a result, the part of the probability distribution with large  $\tilde{\rho}$  is dominant. This means that we can approximate  $P_{\parallel}(\tilde{\rho})$  by  $\pi \exp(-\pi^2 \tilde{\rho}/4)$ . Now, the integral in Eq. (2.20) can be easily done to obtain

$$\langle r_z(L, f) \rangle = L + \frac{L(\pi^2 + 4f'\epsilon)}{4\pi(1-y)} \left[ -\frac{16\pi\epsilon(1-y)}{(\pi^2 + 4f'\epsilon)^2} + \frac{4\pi y}{\pi^2 + 4f'\epsilon} \right] \quad (\text{D.1})$$

in which  $f' = fL/k_B T$  and  $y = \exp(-f' - f'_c)$  with  $f'_c$  being the dimensionless Euler buckling force ( $f'_c k_B T/L = \pi^2 \kappa/4L^2$ ).

A comparison of this approximation with the exact form is presented in Fig. D.1 for different values of  $\epsilon$ . Since  $\epsilon \ll 1$  in our case, the approximation is rather good for both pulling and pushing forces. We will use it for the whole range of  $f$ .

Now, we consider the case that the filament is attached to a rigid wall by a linker with spring constant  $k_l$  (Fig. D.2). The aim is to calculate the pulling force  $f$  as a function of  $z$ . It is obvious that when  $z > R_{\parallel}$ ,  $z = r_z(L, f) + r_l$  holds ( $r_l$  length of linker molecule). But for  $z \leq R_{\parallel}$ , the linker does not play any role and  $z = r_z(L, f)$  is valid. All of this leads to the following non-linear equations for  $f$  as a function of  $z$

$$z = \begin{cases} f/k_l + r_z(L, f) & z \geq R_{\parallel} \\ r_z(L, f) & z < R_{\parallel} \end{cases} \quad (\text{D.2})$$

In the small force regime, the linker is a spring acting in series with the attached filament with an effective spring constant  $k_{\text{eff}} = k_l k_{\parallel}/(k_l + k_{\parallel})$ . In

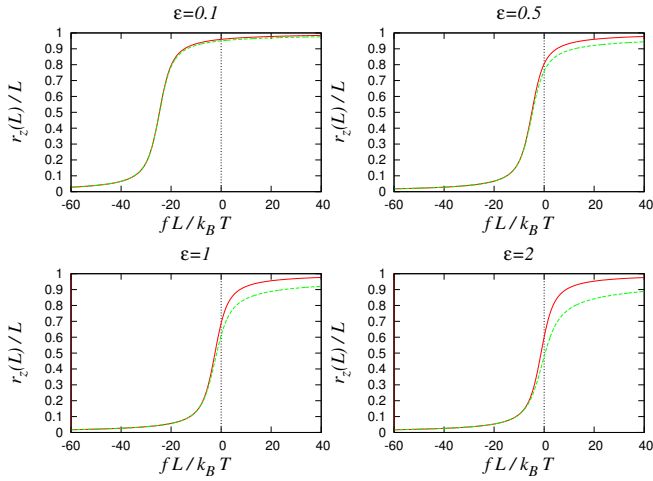


**Figure D.1** Comparison of the exact result (green line) with approximation (red line). The approximation works rather good for small values of  $\epsilon$  and especially for compressing forces.

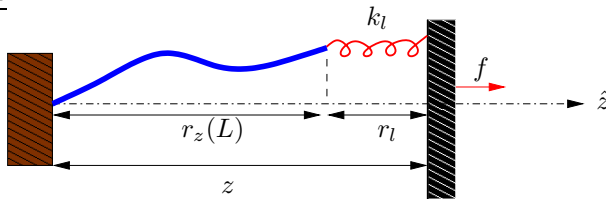


**Figure D.2** A grafted semiflexible polymer is attached to a wall via a linker with spring constant  $k_l$ .

the strong force regime, the effective spring constant of the system switches to  $k_l$ . The force-extension relation of the filament is highly nonlinear for strong forces and the force diverges like  $1/(L - r_z(L))^2$  at full stretching (see Eq. (1.10)). Since a finite external force can not stretch the filament to its full contour length and beyond, mostly the linker will be extended.

We assume that the transition between the regimes happens at  $L^* = L - f^*/k_l$ , in which  $f^*$  is the solution of Eq. (D.2) at  $z = L$ . With the dimensionless variables  $\phi = k_l L^2/k_B T$  and  $\epsilon = L/\ell_p$ ,  $f^*$  can be approximated as

$$f^* L/k_B T \approx \frac{2}{3} \epsilon^{-3} \left( 27\phi^2 \epsilon^{-2} - 8\epsilon^{-6} + 3\sqrt{3} \sqrt{27\phi^4 \epsilon^{-4} - 16\phi^2 \epsilon^{-8}} \right)^{-1/3} + \frac{1}{6} \left( 27\phi^2 \epsilon - 8\epsilon^{-1} + 3\sqrt{3} \sqrt{27\phi^4 \epsilon^2 - 16\phi^2 \epsilon^{-2}} \right)^{1/3} - \frac{1}{3\epsilon} \quad (\text{D.3})$$

$L^*$  is very close to  $L$ , so as an approximation we assume that the transition of  $k_{\text{eff}}$  to  $k_l$  happens at  $L$ . In the end, our linear approximation is

$$f(L, z) = \begin{cases} -k_{\parallel}(z - R_{\parallel}) & z \leq R_{\parallel} \\ -k_{\text{eff}}(z - R_{\parallel}) & R_{\parallel} < z < L \\ -k_l(z - L) - k_{\text{eff}}(L - R_{\parallel}) & z \geq L \end{cases} \quad (\text{D.4})$$

The numerical solutions to Eqs. (D.2), as well as the linear approximations in Eq. (D.4) are presented in Fig. D.3 for different values of  $L$ .

Examples for the time course of forces during typical oscillations are shown in Fig. D.4. Forces of attached filaments pull the obstacle back most of the time, i.e.  $z > R_{\parallel}$  holds almost always.

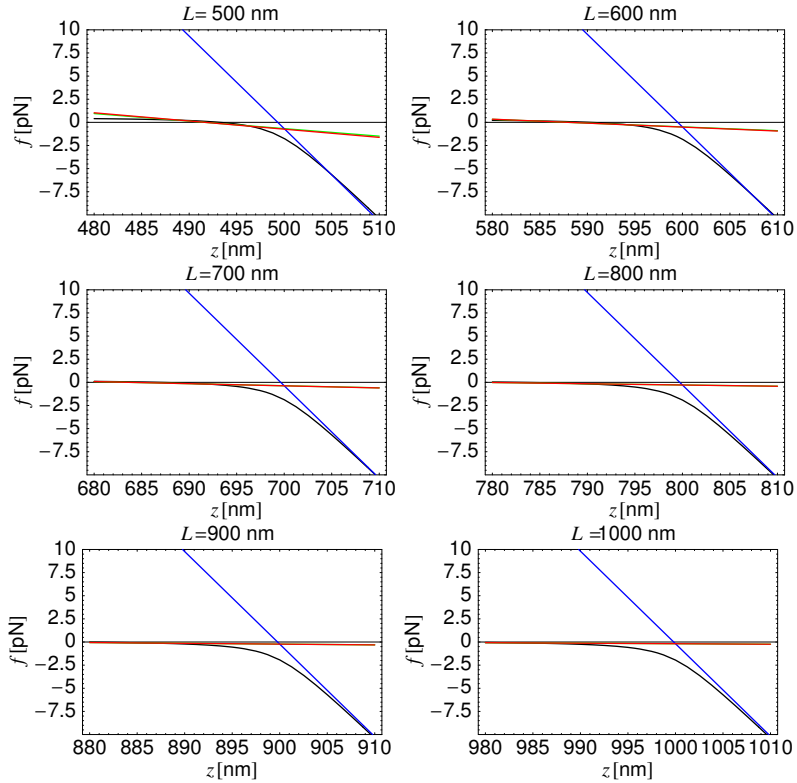


**Figure D.3** Force exerted on the obstacle by a single polymer as a function of  $x$  for different values of  $L$ . Parameters are  $\ell_p = 15 \mu\text{m}$ ,  $k_l = 1 \text{ pN/nm}$ ,  $k_B T = 4.1 \text{ pN nm}$ ,  $d = 3$ . The black curve is the force-extension curve calculated from Eq. (D.2). The red, green and blue curves are the linear approximations from Eq. (D.4) with slope  $k_{\parallel}$ ,  $k_{\text{eff}}$  and  $k_l$  respectively.

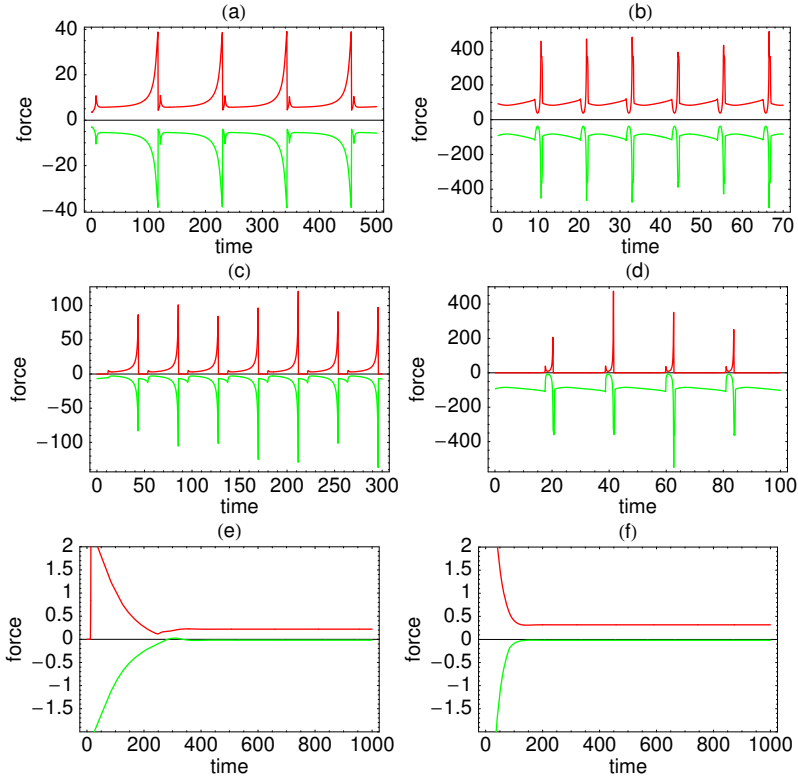


**Figure D.4** Total pushing force (red) as well as total pulling force (green) with  $N = 200$  polymers as a function of time for  $v_g^{\max} = 300$  nm/s,  $v_p^{\max} = 500$  nm/s,  $k_d^0 = 0.5$  s $^{-1}$  and (a)  $d=3$ ,  $k_a = 0.144$  s $^{-1}$ , (b)  $d=3$ ,  $k_a = 3.46$  s $^{-1}$ , (c)  $d=2$ ,  $k_a = 0.3$  s $^{-1}$ , (d)  $d=2$ ,  $k_a = 3.47$  s $^{-1}$ , (e)  $d=2$ ,  $k_a = 0.186$  s $^{-1}$  (stationary) and (f)  $d=3$ ,  $k_a = 0.1$  s $^{-1}$  (stationary). Forces are in pN and time is in seconds.



# Bibliography

The references are listed alphabetically; a dash indicates a repeated author list.

- Abramowitz, A. and I. Stegun: *Handbook of Mathematical Functions with Formulas, Graphs, and Mathematical Tables* (Dover, New York, 1970).
- Anderson, K. and R. Cross: *Contact dynamics during keratocyte motility*, *Curr. Biol.* **10**, 253 (2000).
- Benetatos, P. and E. Frey: *Depinning of semiflexible polymers*, *Phys. Rev. E* **67**, 051108 (2003).
- *Linear response of a grafted semiflexible polymer to a uniform force field*, *Phys. Rev. E* **70**, 051806 (2004).
- Benetatos, P., T. Munk, and E. Frey: *Bimodality in the transverse fluctuations of a grafted semiflexible polymer and the diffusion-convection analogue: An effective-medium approach*, *Phys. Rev. E* **72**, 030801 (2005).
- Bernheim-Groswasser, A., J. Prost, and C. Sykes: *Mechanism of actin-based motility: A dynamic state diagram*, *Biophys. J* **89**, 1411 (2005).
- Bernheim-Groswasser, A., S. Wiesner, R. Golsteyn, M. Carlier, and C. Sykes: *The dynamics of actin-based motility depend on surface parameters*, *Nature* **417**, 308 (2002).
- Borisy, G. and T. Svitkina: *Actin machinery: pushing the envelope*, *Curr. Opin. Cell Biol.* **12**, 104 (2000).
- Bray, D.: *Cell Movements* (Gerland, 2001).
- Brierer, W. M., M. Coughlin, and T. Mitchison: *Fascin-mediated propulsion of listeria monocytogenes independent of frequent nucleation by the Arp2/3 complex*, *J. Cell Biol.* **165**, 233 (2004).
- Cameron, L., P. Giardini, F. Soo, and J. Theriot: *Secrets of actin-based motility revealed by a bacterial pathogen*, *Mol. Cell Biol.* **1**, 110 (2000).

- Cameron, L., T. Svitkina, D. Vignjevic, J. Theriot, and G. Borisy: *Dendritic organization of actin comet tails*, *Curr. Biol.* **11**, 130 (2001).
- Cameron, L. A., M. J. Footer, A. V. Oudenaarden, and J. A. Theriot: *Motility of ActA protein-coated microspheres driven by actin polymerization*, *Proc. Natl. Acad. Sci. USA.* **96**, 4908 (1999).
- Carlier, M. and D. Pantaloni: *Control of actin dynamics in cell motility*, *J. Mol. Biol.* **269**, 459 (1997).
- Carlsson, A. E.: *Growth velocities of branched actin networks*, *Biophys. J.* **84**, 2907 (2003).
- Clerc, P. and P. Sansonetti: *Entry of Shigella flexneri into HeLa cells: evidence for directed phagocytosis involving actin polymerization and myosin accumulation*, *Infect. Immun.* **55**, 2681 (1987).
- Cudmore, S., P. Cossart, G. Griffiths, and M. Way: *Actin-based motility of vaccinia virus*, *Nature* **378**, 636 (1995).
- Daniels, D. R. and M. S. Turner: *The force generated by biological membranes on a polymer rod and its response: Statics and dynamics*, *J. Chem. Phys.* **121**, 7401 (2004).
- Disanza, A., A. Steffen, M. Hertzog, E. Frittoli, K. Rottner, and G. Scita: *Actin polymerization machinery: the finish line of signalling networks, the starting point of cellular movement*, *Cell. Mol. Life Sci.* **62**, 955 (2005).
- Edelstein-Keshet, L. and G. Ermentrout: *Models for spatial polymerization dynamics of rod-like polymers*, *J. Math. Biol.* **40**, 64 (2000).
- Evans, E. and K. Ritchie: *Strength of a weak bond connecting flexible polymer chains*, *Biophys. J.* **76**, 2439 (1999).
- Fixman, M. and J. Kovac: *Polymer conformational statistics III: Modified Gaussian models of the stiff chains*, *J. Chem. Phys.* **58**, 1564 (1973).
- Frey, E., K. Kroy, J. Wilhelm, and E. Sackmann: *Dynamical Networks in Physics and Biology* (Springer, Berlin, 1998).
- Gerbal, F., P. Chaikin, Y. Rabin, and J. Prost: *An elastic analysis of Listeria monocytogenes propulsion*, *Biophys. J.* **79**, 2259 (2000a).
- Gerbal, F., V. Laurent, A. Ott, P. Chaikin, and J. Prost: *Measurement of the elasticity of the actin tail of Listeria monocytogenes*, *Biophys. J.* **29**, 134 (2000b).
- Gholami, A., J. Wilhelm, and E. Frey: *Entropic forces generated by grafted semi-flexible polymers*, *Phys. Rev. E* **74**, 41803 (2006).

- Goldberd, M. and J. Theriot: *Shigella flexneri* surface protein *IcsA* is sufficient to direct actin-based motility, Proc. Natl. Acad. Sci. USA. **92**, 6572 (1995).
- Gouin, E., M. Welch, and P. Cossart: *Actin-based motility of intracellular pathogens*, Curr. Opin. Microbiol **8**, 35 (2005).
- Gracheva, M. and H. Othmer: *A continuum model of motility in ameboid cells*, Bull. Math. Biol. **66**, 167 (2004).
- Hansen, E. R.: *A Table of Series and Products* (Prentice-Hall, Englewood Cliffs, N. J., 1975).
- Helfrich, W.: *Steric interaction of fluid membranes in multilayer systems*, Z. Naturforsch. **33a**, 305 (1978).
- Hermans, J. J. and R. Ullman: *The statistics of stiff chains, with applications to light scattering*, Physica **18**, 951 (1952).
- Hill, T.: *Microfilament or microtubule assembly or disassembly against a force*, Proc. Natl. Acad. Sci. USA. **78**, 5613 (1981a).
- Hill, T. H.: *Microfilament or microtubule assembly or disassembly against a force*, Proc. Natl. Acad. Sci. USA. **78**, 5613 (1981b).
- Kocks, C., R. Hellio, P. Gounon, H. Ohayon, and P. Cossart: *Polarized distribution of Listeria monocytogenes* surface protein *ActA* at the site of directional actin assembly, J. Cell Sci. **105**, 699 (1993).
- Kovac, J. and C. Crabb: *Modified Gaussian model for rubber elasticity. 2. The wormlike chain*, Macromolecules **15**, 537 (1982).
- Kratky, O. and G. Porod: *Rontgen untersuchung geloster fadenmolekule*, Rec. Trav. Chim. **68**, 1106 (1949).
- Kroy, K.: *Viskoelastizitaet von Lösungen halbsteifer Polymere*, Ph.D. thesis, München (1998).
- Kroy, K. and E. Frey: *Force-extension relation and plateau modulus for wormlike chains*, Phys. Rev. Lett. **77**, 306 (1996).
- Kuo, S. C. and J. McGrath: *Steps and fluctuations of Listeria monocytogenes during actin-based motility*, Nature **407**, 1026 (2000).
- Landau, L. D. and E. Lifshitz: *Theory of Elasticity* (Pergamon Press, London, 1959).
- Lasa, I., E. Gouin, M. Goethals, K. Vancompernelle, V. David, J. Vandekerckhove, and P. Cossart: *Identification of two regions in the N-terminal domain of acta involved in the actin comet tail formation by Listeria monocytogenes*, EMBO J. **16**, 1531 (1997).

- Lattanzi, G., T. Munk, and E. Frey: *Transverse fluctuations of grafted polymers*, Phys. Rev. E **69**, 021801 (2004).
- Lee, J., A. Ishiara, and K. Jacobson: *The fish epidermal keratocyte as a model system for the study of cell locomotion*, in *Cell behavior: adhesion and motility*, edited by G. Jones, C. Wigley, and R. Warn (Cambridge, 1993a).
- Lee, J., A. Ishiara, J. Theriot, and K. Jacobson: *Principles of locomotion for simple-shaped cells*, Nature **362**, 467 (1993b).
- LeGoff, L., O. Hallatschek, E. Frey, and F. Amblard: *Tracer studies on F-actin fluctuations*, Phys. Rev. Lett. **89**, 258101 (2002).
- Lipowsky, R.: *Lines of renormalization group fixed points for fluid and crystalline membranes*, Europhys. Lett. **7**, 255 (1988).
- *The conformation of membranes*, Nature **349**, 475 (1991).
- *Stacks and bunches of fluid membranes*, J. Phys: Condens. Matter **6**, A409 (1994).
- Lipowsky, R. and S. Leibler: *Unbinding transitions of interacting membranes*, Phys. Rev. Lett. **56**, 2541 (1986).
- Lipowsky, R. and B. Zielinska: *Binding and unbinding of lipid membranes: A Monte Carlo study*, Phys. Rev. Lett. **62**, 1572 (1989).
- Loisel, T. P., R. Boujemaa, D. Pantaloni, and M. Carlier: *Reconstitution of actin-based motility of Listeria and Shigella using pure proteins*, Nature **401**, 613 (1999).
- Lubensky, T. C.: *Soft condensed matter physics*, Solid State Comm. **102**, 187 (1997).
- Marcy, Y., J. Prost, M. Carlier, and C. Sykes: *Forces generated during actin-based propulsion: A direct measurement by micromanipulation*, Proc. Natl. Acad. Sci. USA. **101**, 5992 (2004).
- Marko, J. F. and E. Siggia: *Stretching DNA*, Macromolecules **28**, 8759 (1995).
- Meunier, J., D. Langevin, and N. Boccara (eds.): *Physics of Amphiphilic Layers* (Springer, Berlin, 1987).
- Mitchison, T. J. and L. P. Cramer: *Actin-based cell motility and cell locomotion*, Cell **84**, 371 (1996).
- Mogilner, A. and L. Edelstein-Keshet: *Regulation of actin dynamics in rapidly moving cells: a quantitative analysis*, Biophys. J. **83**, 1237 (2002).

- Mogilner, A. and G. Oster: *Cell motility driven by actin polymerization*, Eur. Biophys. J. **25**, 47 (1996a).
- *The physics of lamellipodial protrusion*, Biophys. J. **71**, 3030 (1996b).
- *Force generation by actin polymerization II: the elastic ratchet model and tethered filaments*, Biophys. J. **84**, 1591 (2003).
- Oosawa, F. and S. Asakura: *A theory of linear and helical aggregations of macromolecules*, J. Mol. Biol. **4**, 10 (1962).
- Ott, A., M. Magnasco, A. Simon, and A. Libchaber: *Measurement of the persistence length of polymerized actin using fluorescence microscopy*, Phys. Rev. E **48**, R1642 (1993).
- Pampaloni, F., G. Lattanzi, A. Jonas, T. Surrey, E. Frey, and E. L. Florin: *Thermal fluctuations of grafted microtubules provide evidence of a length-dependent persistence length*, Proc. Natl. Acad. Sci. USA. **103**, 10248 (2006).
- Pantaloni, D., C. Clainche, and M. Carlier: *Mechanism of actin based motility*, Science **292**, 1502 (2001).
- Parekh, S. H., O. Chaudhuri, J. Theriot, and D. Fletcher: *Loading history determines the velocity of actin-network growth*, Nat. Cell Biol. **7**, 1219 (2005).
- Peskin, C., G. Odell, and G. Oster: *Cellular motions and thermal fluctuations: The Brownian ratchet*, Biophys. J. **65**, 316 (1993).
- Plastino, J. and C. Sykes: *The actin slingshot*, Curr. Opin. Cell Biol. **17**, 62 (2005).
- Pollard, T.: *Rate constants for the reactions of ATP- and ADP- actin with the ends of actin filaments*, J. Cell Biol. **103**, 2747 (1986).
- Pollard, T., L. Blanchoin, and R. Mullins: *Molecular mechanism controlling actin filament dynamics in nonmuscle cells*, Annu. Rev. Biophys. Biomol. Struct. **29**, 545 (2000).
- Pollard, T. and G. Borisy: *Cellular motility driven by assembly and disassembly of actin filaments*, Cell **112**, 453 (2003).
- Roth, R., R. van Roij, A. Andrienko, K. Mecke, and S. Dietrich: *Entropic torque*, Phys. Rev. Lett. **89**, 088301 (2002).
- Safran, S.: *Statistical Thermodynamics of Surfaces, Interfaces, and Membranes* (Westview Press Inc, 2003).
- Saito, N., K. Takahashi, and Y. Yunoki: *The statistical mechanical theory of stiff chains*, J. Phys. Soc. Jap. **22**, 219 (1967).

- Schwartz, I. M., M. Ehrenberg, M. Bindschalter, and J. L. McGrath: *The role of substrate curvature in actin pushing forces*, *Curr. Biol* **14**, 1094 (2004).
- Semeriyarov, F. and S. Stepanow: *Bimodal distribution function of a 3d wormlike chain with a fixed orientation of one end*, *Phys. Rev. E* **75**, 061801 (2007).
- Small, J.: *Lamellipodia architecture: actin filament turnover and the lateral flow of actin filaments during motility*, *Semin. Cell Biol.* **5**, 157 (1994).
- Small, J., M. Herzog, and K. Anderson: *Actin filament organization in the fish keratocyte lamellipodium*, *J. Cell Biol.* **129**, 1275 (1995).
- Southwick, F. and D. Purich: *Listeria and Shigella actin-based motility in host cells*, *Trans. Am. Clin. Climatol. Assoc.* **109**, 160 (1998).
- Svitkina, T. and G. Borisy: *Arp2/3 complex and actin depolymerizing factor/cofilin in dendritic organization and treadmilling of actin filament array in lamellipodia*, *J. Cell Biol.* **145**, 1009 (1999).
- Svitkina, T., A. Verkhovsky, K. McQuade, and G. Borisy: *Analysis of the actin-myosin II system in fish epidermal keratocytes: mechanism of cell body translocation*, *J. Cell Biol.* **139**, 397 (1997).
- Theriot, J. and T. Mitchison: *Actin microfilament dynamics in locomoting cells*, *Nature* **352**, 126 (1991).
- Theriot, J. A., T. J. Mitchison, L. G. Tilney, and D. A. Portney: *The rate of actin-based motility of intracellular Listeria monocytogenes equals the rate of actin polymerization*, *Nature* **357**, 257 (1992).
- Upadhyaya, A., J. R. Chabot, A. Andreeva, A. Samadani, and A. V. Oudenaarden: *Probing polymerization forces by using actin-propelled lipid vesicles*, *Proc. Natl. Acad. Sci. USA.* **100**, 4521 (2003).
- Upadhyaya, A. and A. V. Oudenaarden: *Actin polymerization: Forcing flat faces forward*, *Curr. Biol.* **14**, R467 (2004).
- Van Oudenaarden, A. and J. A. Theriot: *Cooperative symmetry-breaking by actin polymerization in a model for cell motility*, *Nature Cell Biol.* **1**, 493 (1999).
- Wegner, A.: *Head to tail polymerization of actin*, *J. Mol. Biol.* **108**, 139 (1976).
- Welch, M., A. Mallavarapu, J. Rosenblatt, and T. Mithison: *Actin dynamics in vivo*, *Curr. Opin. Cell Biol.* **9**, 54 (1997).
- Wilhelm, J. and E. Frey: *Radial distribution function of semiflexible polymers*, *Phys. Rev. Lett.* **77**, 2581 (1996).

# Acknowledgement

I would like to thank Prof. Dr. Erwin Frey for giving me the opportunity to do my PhD in his group and for posing the interesting and challenging subject of this thesis. I always enjoyed discussing physics with him, usually coming up with new and creative ideas.

My collaboration with Dr. Martin Falcke in last year of my PhD was very fruitful. He has always giving me a high motivation to continue my work. Without his guidance, I might have been lost at the middle of the way. I'm really very grateful to him.

During one year stay in India, I benefited from discussions with Dr. Madan Rao. I am very much indebted to him for introducing me to the interesting field of biophysics and recommending me to Prof. Dr. Erwin Frey.

My husband Iraj has been a big support for me in last 6 years. He has made my life more colorful and beautiful with love. Without his help, I never could finish my PhD on time. I thank him for every thing.

My little daughter Hasti, with her beautiful smiles, always has been a source of energy and happiness for us in last 3 years. I thank God for such a beautiful gift.

I am very grateful to my parents for all encouragements and supports. They did all they could to prepare the best for me. I'm really proud of them and I hope, I deserve all this mercy and kindness.

Working in HMI would not have been possible without having a friendly atmosphere. My special thanks to Alexander Skupin, Felix Höfling, Erin Higgins, Mihaela Enculescu, Klaus Kroy, Panayotis Benetatos and Katarzyna Skorupska.

I appreciate financial supports from the Deutsche Forschungsgemeinschaft (Graduate Kolleges 265 on "Dynamics and evolution of cellular and macromolecules") and Hahn-Meitner Institute.



# Lebenslauf

## Persönliche Daten

Azam Gholami  
Chausseestr 12A  
14109 Berlin

Tel: (0049) 0176 2161 9831  
E-mail: azam@hmi.de

Geb. am 25.06.1977 in Tehran  
Verheirated, Iranerin

## Schulbildung

10/91-06/95           Gymnasium in Tehran (Leistungskurse  
Mathematik und Physik)

## Studium

10/95-06/99           Batchelor in Physik an der Sharif  
Universität (Tehran, Iran)  
10/99-10/2001        Master in Physik an der Institute for Advanced  
Studies in Basic Sciences (Zanjan, Iran)

## Promotion

01/2002-12/2002     Theoretische Doktorarbeit bei Prof. Madan Rao am  
Raman Research Institut, Bangalore, Indien (resigniert)  
01/2003-06/2007     Theoretische Doktorarbeit bei Prof. Erwin Frey am  
Hahn-Meitner Institut in Berlin, Deutschland